DECONSTRUCTION OF SEPTIN ASSEMBLY

Agata Szuba

This thesis was reviewed by:

prof.dr. A.S. Akhmanova	Universiteit Utrecht
dr. T. Idema	Technische Universiteit Delft
prof.dr. S. Mostowy	London School of Hygiene & Tropical Medicine
prof.dr. W.H. Roos	Rijksuniversiteit Groningen
prof.dr.ir. G.J.L. Wuite	Vrije Universiteit Amsterdam

The work described in this thesis was performed at AMOLF, Science Park 104, 1098 XG Amsterdam, The Netherlands. This work is part of the Dutch Research Council (NWO).

Cover design: Aline Faro
Printed by: GVO drukkers & vormgevers B.V.

ISBN: 978-94-92323-29-3

A digital version of this thesis can be obtained from www.amolf.nl and from www.ub.vu.nl. Printed copies can be obtained by request via library@amolf.nl.

VRIJE UNIVERSITEIT

DECONSTRUCTION OF SEPTIN ASSEMBLY

ACADEMISCH PROEFSCHRIFT

ter verkrijging van de graad Doctor of Philosophy
aan de Vrije Universiteit Amsterdam,
op gezag van de Rector Magnificus
prof.dr. V. Subramaniam,
in het openbaar te verdedigen
ten overstaan van de promotiecomissie
van de Faculteit der Bètawetenschappen
op maandag 11 november 2019 om 13.45 uur
in de aula van de universiteit,
De Boelelaan 1105

door

Agata Szuba

geboren te Warschau, Polen

promotor: prof.dr. G.H. Koenderink

Simple is beautiful

Contents

1

Introduction

1.1 Cell shape control

Cells in our bodies can take different shapes, depending on the type of tissue. For example neurons build long protrusions in order to build synapses, while muscle cells optimize their shape to generate contractile forces. Cells are also are very dynamic. They change their shape dramatically during cell division, migration, and wound healing. Cell shape changes are made possible by the combination of a thin and deformable plasma membrane made of lipids, and a dynamic scaffold that spans the cell made of protein filaments, which is known as the cytoskeleton. Control of cell dynamics requires careful regulation by accessory proteins, including septins, which are the focus of this thesis. Below, we introduce the two main determinants of cell shape, the membrane and the cytoskeleton, and then zoom in on the properties of septins.

1.1.1 Plasma membrane

The eukaryotic plasma membrane is a thin sheet with a thickness of around 4 nm that separates the cell interior from the environment. It is composed of over a hundred different types of lipids [1]. Due to their amphiphilic nature, lipids naturally form a bilayer, in which hydrophobic fatty acid tails are buried inside the bilayer and the hydrophilic heads are exposed to the aqueous cytoplasm and extracellular environment. The most abundant lipids in the plasma membrane are *phospholipids* (>50%), which have one polar head group and two fatty acid chains attached to it. The main phospholipids are phosphatidylcholine (PC), phosphatidylethanolamine (PE), phosphatidylserine (PS), and phosphatidic acid (PA). One of the two tails is usually unsaturated, which means it has one or more double bonds in the carbon

chain resulting in a kink in the tail. A second important class of lipids are the *sphingolipids* (e.g. sphingomyelin), which have only one hydrophobic tail. The third, and most non-polar, class of lipids are *sterols* such as cholesterol, with its four ring bulky steroid structure that interacts with fatty acids in the hydrophobic part of the plasma membrane, while its single cholesterol group interacts with polar lipid heads. Sphingolipids and sterols together make up the other 50% of lipids in the plasma membrane.

The exact lipid composition depends on cell type and developmental stage. Moreover, the lipid composition is different in the inner and outer leaflet of the bilayer. For instance, PS localizes specifically to the inner leaflet. The asymmetric distribution of lipids with different preferred shapes between the two bilayer leaflets generates membrane curvature, which contributes to the formation of constrictions and protrusions of the plasma membrane .

Apart from providing a boundary for the cell, the plasma membrane has many other important functions, including transmembrane transport, cell signaling and facilitating cell shape changes. Typically the membrane is presented as a 2-dimensional fluid layer with freely diffusing proteins embedded in it. However, it has been shown that the lipids do not mix entirely uniformly. Instead they form transient domains with different chemical and physical properties. These nanoscale domains are coupled across leaflets and are believed to play a crucial role in signal transduction between the cell and its environment. The formation and maintenance of these domains is driven by lipid-lipid as well as lipid-protein interactions [2–4]. Some cells even feature large-scale microdomains, especially in regions that require segregation of functional components in the plasma membrane. Examples are the apical and basolateral membranes of epithelial cells, the neck region of budding yeast cells, sperm tails, and dendritic arbors [5]. These microdomains often correlate with the presence of diffusion barriers. Not much is known about the molecular origin of diffusion barriers and the way in which they maintain membrane compartmentalization. It is thought that the underlying actin cortex, together with its interactors, plays an important role in this process [5]. There seems to be an especially central role for septins [4], the protein family that is the focus of this thesis.

1.1.2 Cytoskeleton

The cytoskeleton is a dynamic network of protein filaments that spans the entire cell, connecting the plasma membrane to the nucleus. It is traditionally considered to be made up of three distinct filamentous components: actin filaments, intermediate filaments and microtubules. Alone and in interaction with each other, these filamentous systems govern cell shape and mechanics [6]. As we will discuss below, septins were recently identified as a fourth cytoskeletal system, which also contributes to the regulation of cell shape and mechanics [7].

Actin is a globular protein of a size of 42 kDa that polymerizes in the presence of the chemical fuel molecule adenosine triphosphate (ATP) to form double-stranded

filaments with a diameter of ~7 nm. Actin filaments are structurally polar with two distinct ends denoted as the plus (or barbed) end, where monomers preferentially bind, and the minus (or pointed) end, from which actin monomers preferentially detach. In the presence of ATP, one end therefore grows faster than the other. The persistence length of actin filaments is ~ 10 μm [8], which is of the same order as their contour length. Accordingly, actin filaments are classified as semiflexible polymers. Actin is predominantly found at the cell cortex and is the main contributor to cortical stiffness and tension [9]. Actin filaments interact with other proteins to organize into dynamic higher order structures, such as lamellipodia, filopodia and the contractile ring that drives cell division [10]. These structures can dynamically rearrange and drive cell motion, thanks to pushing forces generated by actin filament growth and pulling forces generated by myosin motors that use ATP to slide actin filaments past one another.

Intermediate filaments form a large family of proteins (with ca. 70 genes in humans) forming nonpolar filaments that are responsible for cytoplasmic stiffness and for cellular resilience against large mechanical deformations [11]. Intermediate filaments are formed from fibrous subunits that form rope-like bundles with a diameter of about 11 nm. They are the softest filaments, with a persistence length in range of 0.5 to 2μm [12]. Their complex hierarchical structure makes intermediate filaments very extensible, providing the cell with remarkable mechanical resilience [6].

Microtubules are composed of tubulin dimers, which assemble into hollow tubes composed of 13 protofilaments and with a diameter of ~ 25nm [13]. They are the stiffest cytoskeletal filaments, with a persistence length in the order of millimeters [14]. Similar to actin filaments, microtubules possess a structural polarity because the subunits hydrolyze the nucleotide guanosine triphosphate (GTP). In the presence of GTP, microtubules exhibit a phenomenon known as dynamic instability, meaning that their fast-growing plus end undergoes stochastic switches from polymerization to depolymerization (catastrophes) and back (rescues). This dynamics allows microtubules to quickly remodel and form dynamic structures such as the mitotic spindle, which drives chromosome segregation in dividing cells. Furthermore, microtubules serve as molecular railway tracks for molecular motors from the dynein and kinesin families, which transport different types of cargoes such as organelles. Finally, microtubules also make up motile substructures of the cell like ciliae and flagellae.

Another protein family known as the *septins* was only recently recognized as a fourth element of the cytoskeleton [7]. They form structurally nonpolar filaments and they interact with the plasma membrane as well as with two of the other cytoskeletal components, namely actin filaments and microtubules [15] (Fig. 1.1). They have been reported to play a role in cell rigidity and deformability during diverse cellular processes, including cell migration and tissue morphogenesis in developing embryos. Septin filaments exhibit much slower turnover in the cell than both actin filaments and microtubules, and are therefore thought to act as organizing centers that help create

and maintain functional domains and structures such as the cell cortex, contractile ring, and actin stress fibers [15, 16]. However, the exact nature of the interactions of septins with themselves, with the plasma membrane, and with the other cytoskeletal components remains elusive. The following parts of the introduction will describe in more details what we currently know about septins.

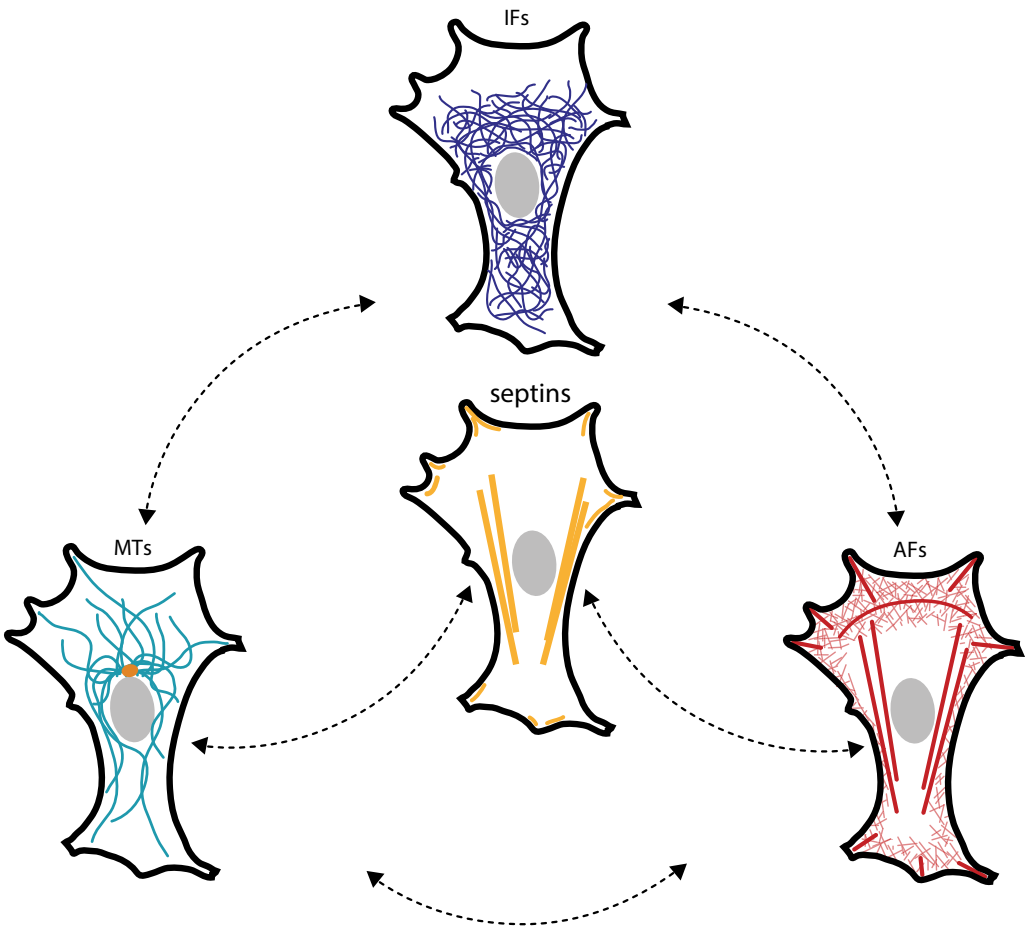

Figure 1.1: Septins are a part of the cytoskeleton of yeast and animal cells, together with intermediate filaments (IFs), actin filaments (AFs), and microtubules (MTs). The images show a schematic top view of mammalian cells that are adhered to a flat substrate, with a protrusive front (upper side) and contractile rear (lower side). The nucleus is represented by the grey ellipses and the plasma membrane is drawn as black outlines. Septins (depicted in orange) form filamentous structures that interact with the plasma membrane, actin filaments, and microtubules (dashed arrows). The other cytoskeletal components also interact with each other and influence each other's organization. Septins are enriched in curved regions of the cell and are associated with actin stress fibers. IFs form extended networks that pervade the cytoplasm, MTs usually form radial arrays that are tethered by their minus ends to the centrosome, and AFs form branched arrays, thin cortical meshworks underneath the membrane, and bundles known as stress fibers. Figure adapted from [6].

1.2 Septins

1.2.1 The septin family of proteins

Septins are GTP-binding proteins that were discovered in the 1970s in the budding yeast (*S. cerevisiae*) as components of the cytokinetic ring during septum formation, hence the name [17]. It was later found that they are expressed in all eukaryotes, except for plants [15]. Although septins are conserved among species, the number of genes greatly varies among different organisms. For example, nematodes (*C. elegans*) have only 2 septin genes, *S. cerevisiae* has 7, the fruit fly (*D. melanogaster*) has 5, and humans have 13 genes. In mammals, additional diversity arises from the variety of transcripts generated from alternative promoters or from splicing. Septins are expressed in a tissue-specific and developmentally regulated manner, which likely contributes to the specific phenotypes exhibited by different cell types.

Septins all share a common domain organization. They have a highly conserved GTP-binding domain that is flanked by a polybasic region thought to mediate membrane binding on the amino-terminal side, and by the septin unique element (SUE) of unknown function on the carboxy-terminal side. The amino-terminal region furthermore contains a proline-rich stretch, while the C-terminus of most septins is predicted to form a coiled-coil domain. The C- and N-terminal regions greatly vary in length and amino-acid sequence, and are a base for the classification of septin genes into 4 groups [18] (see Fig. 1.2).

A

Septin group	Human	Fruit fly *D. melanogaster*	Yeast *S. cerevisiae*
SEPT2	SEPT1, SEPT2, SEPT4, SEPT5	Sep1, Sep4	Cdc10, Cdc3, Cdc11, Cdc12, Shs1, Spr3, Spr28
SEPT6	SEPT6, SEPT8, SEPT10, SEPT11, SEPT14	Sep2, Sep5	
SEPT7	SEPT7	Pnut	
SEPT3	SEPT3, SEPT9, SEPT12	———	

B

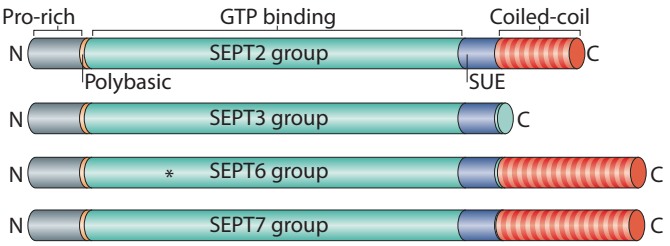

Figure 1.2: Classification and domain structure of septins. A) Table showing the classification of mammalian and fruit fly septins into 4 groups. B) Schematic showing the domain structure of septins. The overall domain structure is conserved, featuring a Proline-rich (Pro-rich) N-terminal domain, a polybasic domain, a globular GTP-binding (G-) domain, a Septin Unique Element (SUE), and a C-terminal region predicted to adopt a coiled-coil structure. Septins from different groups mainly differ in the length and composition of the N- and C-terminal regions (image taken from [7]).

1.2.2 Hierarchical assembly of septins into higher-order structures

Septins form heteromeric complexes that vary in size, depending on species. For example, yeast septins form octamers [19], nematode septins form tetramers [20], fly septins form hexamers [21], and human septins are present in the cell both as hexamers and octamers [22]. Septins form oligomers by associating end-to-end via two types of interfaces: the G-interface, which is made up by the interactions between two globular domains, and the N-C interface, which is made up by interactions between N- and C-terminal regions of septin subunits. Intriguingly, septins assemble in a palindromic manner, resulting in non-polar complexes. Each heterocomplex

contains a pair of identical septin units that belong to one of the four previously mentioned groups (Fig. 1.3). It is thought that a single septin protein from one group can be replaced by another from the same group, often referred to as the Kinoshota rule [18]. It is likely, however, that the total number of physiological septin complexes is far lower than the simple combinatorial prediction of the Kinoshita rule [23].

When purified septins are stored in high salt (>150 mM KCl) buffers, they are present as oligomers. However, when the salt concentration is lowered to physiologically relevant levels (< 150 mM), septin complexes polymerize into filamentous structures. These filaments are best-characterized in the case of yeast septins, where electron microscopy imaging has shown that septins form paired filaments [19]. Each filament is composed of octamers stacked end-to-end, while the paired filament is held together by interactions of the long C-terminal coiled coil regions that emanate from the surface of each filament. In the presence of a lipid bilayer containing anionic lipids, filaments can even form at high salt, suggesting that membrane binding catalyzes septin polymerization [16].

The filaments can in turn form various higher-order structures, such as bundles, networks, coils, and rings (Fig. 1.4). It is poorly understood what interactions drive this self-assembly. The coiled coils may be involved, but there are also indications that the G-domains may contribute to the lateral association of septin filaments.

Like actin and microtubules which bind to nucleotides (ATP and GTP respectively), all septins can bind GTP. Most septins can hydrolyze GTP to GDP, though at a slow rate. Septins from the SEPT6 group do not hydrolyze GTP due to the lack of a threonine residue (see Fig. 1.2B). The functional role of nucleotide binding and hydrolysis has remained enigmatic. Native and recombinant septin complexes are always purified with tightly bound nucleotides. In human hexamers, Sept2 and Sept7 are GDP-bound and Sept6 is GTP-bound [24]. The Sept2/6 interface is a GDP-GTP interface and the Sept7/7 homotypic interface contains GDP. Many lines of evidence suggest that nucleotide binding by septins plays a structural role in stabilizing septin-septin interactions in complexes and filaments [25]. GTP hydrolysis may regulate septin-septin interactions by inducing conformational changes, in particular at the NC interface. Whether GTP hydrolysis plays a role in mediating dynamic turnover of septins in the cell remains unclear.

Posttranslational modifications further regulate the assembly state of septins in the cell [26, 27]. Phosphorylation has been shown to determine in the yeast bud neck whether septins form a ring or a gauze [28, 29]. Sumoylation has been shown to induce ring disassembly at the bud neck [30, 31], and in mammalian cells it seems to prevent septins from forming bundles that can hamper cell division [32].

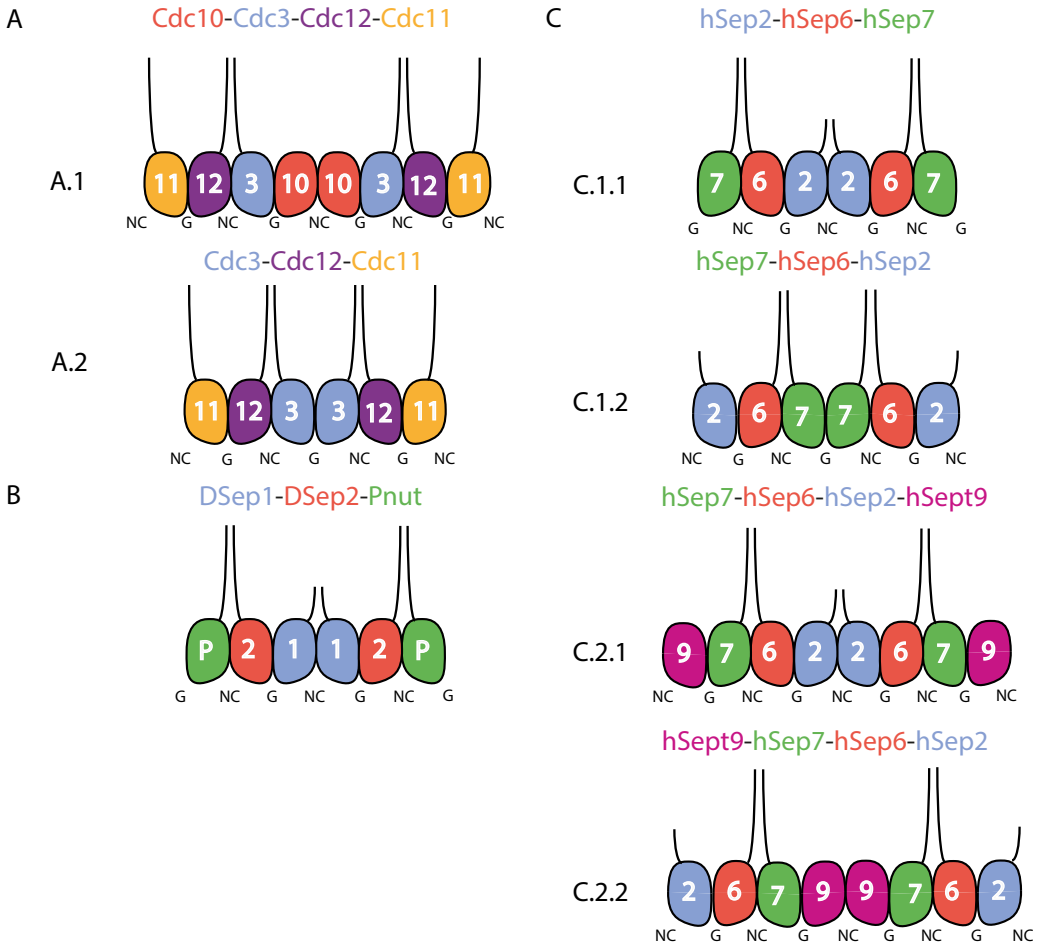

Figure 1.3: Arrangements of yeast (A), fly (B) and human (C) septin complexes. The annotations NC and G refer to the alternating interfaces between N- and C-terminal domains of adjacent subunits and between adjacent G-domains, respectively. A.1: Yeast (*S. cerevisiae*) septin octamer [19]. A.2 Yeast septin hexamer, which lacks the Cdc10 subunits [33]. B: Fly (*D. melanogaster*) septin hexamer, which was used for the majority of the experiments in this thesis. C.1.1 Canonical and best-studied human septin hexamer, for which a crystal structure is available [34]. C.1.2 Recently proposed alternative arrangement of the same complex, which has the NC interfaces exposed, similar to yeast septin complexes [35, 36]. C.2.1 and C.2.2: Proposed arrangements of human septin octamers, containing subunits of the Sept9 group. The Sept9 units were originally proposed [22, 37] to flank the ends (C.2.1), but two recent studies [35, 36] provided evidence that they are actually in the center (C.2.2).

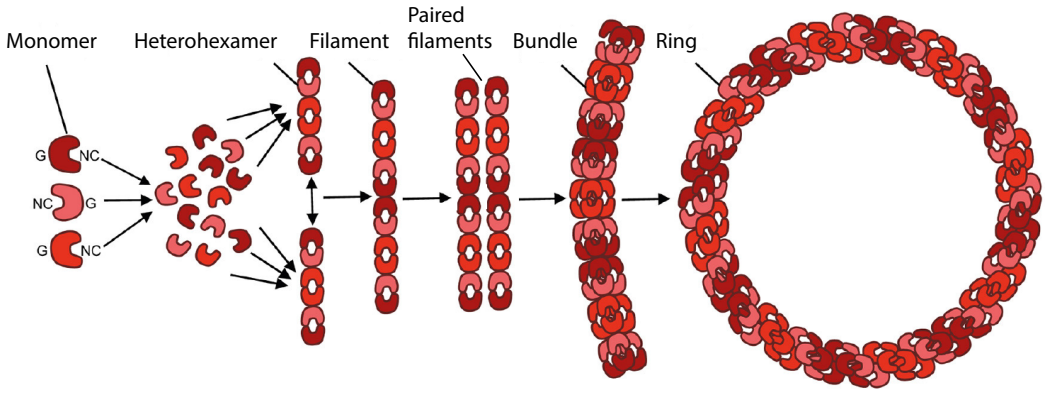

Figure 1.4: Higher order septin assembly. Schematic representation of the hierarchical assembly of septin monomers into complexes (here shown as hexamers), linear filaments, bundles of paired filaments, and rings. In addition to rings, also other higher order structures such as networks (referred to as 'gauzes' in the yeast literature) are formed. Figure edited from [38].

1.2.3 Septin functions

Septins play an important function in cell division, cell polarity and various processes involving membrane remodeling. In animal cells, septins are found in several different locations in the cell, depending on organism, cell type, and the stage of development [15, 16]. Septins interact with actin filaments and with microtubules [15] and are more stable than both of these cytoskeletal components, suggesting that they function as a scaffold that controls the composition of lipids and cytoskeletal proteins at the interface of the actin cortex and the plasma membrane. They also act as a scaffold for specialized molecular machineries of the cell, such as the cytokinetic ring. Septins are also reported to form a cage around pathogenic bacteria in infected human cells to entrap them and promote their elimination by autophagy [39].

From yeast to mammals, septins have a conserved ability to sense the curvature of the plasma membrane on a micron-scale [40, 41]. They are often localized in highly curved regions of the membrane, where they often form a diffusion barrier. Examples are the localization of septins at the cytokinetic ring, at the base of the cilium and at the annulus of sperm cells, dendritic spines, and the phagocytic cup [7, 42].

Abnormal expression levels and mutations in septins have been linked to many neurological diseases like Alzheimer and Parkinson disease [43], as well as male infertility, bleeding disorders and a wide range of cancers [44, 45].

1.3 Septins at the cell cortex

1.3.1 Septins and cell rigidity

The rigidity of the cell cortex plays an important role in cellular functions that require changes in cell shape or cell motility. The actin cortex, a thin (100 nm) layer of actin filaments anchored to the plasma membrane, is generally considered to be the main regulator of cortical rigidity [9]. However, there is evidence suggesting that septins also contribute to cortical rigidity [46]. Cortical elasticity measurements by nanoindentation on HeLa cells showed that septin knockout decreases cortical rigidity to a similar extent as actin perturbation [47]. In the context of immune cell migration, septins were shown to spatially regulate cortical rigidity and thereby influence directional migration [48]. In developing tissues, septins influence cortical tension and tissue shape transformations [49]. In addition to these global regulatory effects on cortical rigidity, septins rigidify specialized membrane regions forming junctions between cell compartments in some cells. Examples are the middle piece just behind the neck in spermatozoa called the annulus [50, 51] and the base of dendritic spines [52].

Since septins interact directly with actin [53, 54] and may potentially crosslink actin filaments or link them to the plasma membrane in cells, it is difficult to determine whether the loss of cortical rigidity in septin-deficient cells is due to the lack of septins themselves, or rather due to membrane-detachment or weakening of the actin cortex. An alternative scenario is that septins may change the composition of the plasma membrane, which might also change membrane rigidity [16].

1.3.2 Septin interactions with the plasma membrane

The importance of septins in cell shape changes and in membrane scaffolding and compartmentalization suggests that septins provide a tight connection between the cytoskeleton and the plasma membrane. Reconstitution experiments have shown that septins are in principle able to directly influence membrane shape on their own, since they bind membranes and form filamentous arrays that induce tubulation of cell-sized lipid vesicles [55]. There is also circumstantial evidence of a direct effect of septins on the membrane in T-cells, where septins are required to retract the plasma membrane after blebs are induced [56]. It has been proposed that septins may regulate membrane tension by sequestering excess membrane [57]. Furthermore, work on epithelial tissues in developing embryos suggests a direct link between cell polarity proteins and septin-mediated compartmentalization of cortical actomyosin [49, 58].

However, how septins interact with lipid bilayers, and if this interaction is direct or mediated by other protein adapters in the cell remains unknown. Septins are reported to interact with acidic phospholipids, with the majority of research until now reporting a specificity for particular phosphoinositides (PIs). PIs make up less than

1% of cellular lipids, but they are essential for signaling. Specific PIs are constantly generated on the plasma membrane and membranous organelles, giving each membrane a distinct biochemical identity [59]. This specificity is likely important for the role of septins in regulating membrane trafficking, phagocytosis, clathrin-mediated endocytosis, micropinocytosis, macropinosome fusion, and degradative sorting [60]. For most of these mechanisms it is not known, however, what exactly the role of septins is, and whether their recruitment is driven by specific lipid recognition, as there are many more proteins involved in each of these processes. If lipid recognition does indeed drive septin recruitment, then it is a puzzle to understand how different septins interact specifically with the large variety of PI subsets.

Purified septins have been shown to interact with various PIs, including their mono-, di-, and tri- phosphorylated forms, but the exact set of PI species interacting with septins seems to vary between organisms and possibly between different septin subunits [40, 55, 61–66]. Septins do not have any of the canonical domains known to bind specifically to PI lipids. They are instead thought to interact with negatively charged phospholipids via a polybasic region close to the N-terminus, which is composed of between 2 and 6 positively charged amino acids [63, 65]. This stretch is very similar to polybasic sequences found in gelsolin, profilin, G-protein-coupled receptor kinases and some ion channels [65], which are all reported to interact with $PI(4,5)P_2$.

1.3.3 Septin-actin interaction

Biochemical reconstitution studies have shown that purified fly and human septins directly interact with filamentous actin [53, 54]. Septin hexamers form curved actin bundles, which may potentially explain the role of septins in stabilizing the contractile ring that drives cell division and the process of cellularization in early stages of development of fruit fly embryos [53]. It was shown that septin knockdown in fruit fly embryos leads to slower membrane ingression during cellularization, indicating that septins are a central component of the contractile ring at the base of the ingressing membrane. In the contractile rings that drive cellularization and cell division, septins additionally interact with actin, myosin and the plasma membrane through a scaffolding protein called anillin [67–70]. During interphase, septins in cultured cells mostly co-localize with actin stress fibers, but they have been also been observed in branched actin structures such as lamellipodia and pseudopodia [15]. This association may be direct, through direct actin-septin binding, but may also involve indirect association through interactions of septins with the plasma membrane or with non-muscle myosin II [71]. Given that septins can interact both directly and indirectly with actin, it is difficult to disentangle the roles of septins and actin in the regulation of the rigidity and dynamics of the actin cortex.

1.4 Goal and approach of this thesis

As explained above, the cell cortex is a key player in controlling the cell shape changes that are necessary for cell motility and division and tissue morphogenesis. The cell cortex is composed of a thin polymeric meshwork containing actin filaments and septins, which is attached to the inner leaflet of the plasma membrane. Non-muscle myosin II motors exert pulling forces on actin filaments, leading to actin network contraction and establishing cell surface tension. The shape, rigidity and tension of the cell cortex are controlled by a plethora of proteins that influence actin-membrane interactions. In this thesis we focus on septins, which are an understudied element of the cytoskeleton. Septins have the ability to interact with lipid membranes, microtubules and actin filaments. The molecular origin of these interactions, the possible involvement of other protein partners, and the role of septin polymerization all remain unknown.

Clearly the living cell is a very complex environment in terms of molecular composition and architecture, which complicates attempts to disentangle the role of septins in cellular functions. We therefore use a cell-free (*in vitro*) reconstitution system to study the biophysical properties of septins alone and in the presence of model biomembranes in a highly controlled manner. We use fly septin hexamers that are expressed and purified from bacteria, and we use a range of microscopy techniques and surface analytical methods to study the higher order assembly of septins and their interactions with biomimetic lipid membranes. The ability to precisely control the molecular composition of the system allows us to obtain quantitative insights in the biophysical properties of septins, which may aid future studies of processes involving septins in cells.

1.5 Thesis outline

The central goal of this thesis is to understand septin higher order assembly and gain more insight into how the resulting septin structures perform their functions at the cell cortex.

In **Chapter 2** of this thesis we first investigate septin self-assembly in solution. We show that fly septin hexamers form bundles, whose shape and thickness differs depending on septin concentration. We apply a quantitative electron microscopy method known as Scanning Transmission Electron Microscopy (STEM) to determine the mass per length of these bundles and correlate this with bundle width. We conclude that fly septins form tightly packed thick bundles comprised of tens to hundreds of subunits per cross-section. By contrast, yeast septin octamers form much thinner, paired filaments.

In **Chapter 3** we next investigate how membrane binding modulates fly septin self-assembly. We show that fly septins interact with glass-supported lipid bilayers, forming dense septin meshworks. We no longer observe bundle formation, indicating

that the membrane interaction competes with the septin-septin interactions that drive bundle formation in solution. We furthermore show that the affinity of fly septins for lipid membranes is dependent on the net negative charge of the membrane, which is different from yeast septins, which specifically bind phosphoinositide lipids. We use an array of high resolution imaging methods to show that fly septins form single and paired filaments on lipid membranes, which are organized into flat arrays that are stable and resistant to mechanical forces.

In **Chapter 4** we investigate the kinetics of septin binding to lipid membranes and the mechanical properties of the ensuing membrane-bound septin films using an acoustic surface analytical technique known as quartz-crystal microbalance with dissipation monitoring (QCM-D) and an optical method known as spectroscopic ellipsometry (SE). We show that septin binding to membranes is dominated by electrostatic interactions and the kinetics are mass transport limited. We furthermore quantify the septin film thickness and rigidity and the amount of hydrodynamically trapped solvent. These insights, combined with the high resolution imaging data reported in Chapter 3, allow us to propose a model explaining how septins assemble on lipid membranes and how the resulting septin films may influence cell cortex mechanics.

Finally, in **Chapter 5** we summarize our findings and we discuss a proof-of-principle experiment where we link a contractile actomyosin cortex to a biomimetic lipid membrane via septins. We show that myosin drives concurrent and colocalized remodeling of septins and actin. This exciting observation suggests that septins may be important for transducing actomyosin-generated forces onto the plasma membrane to generate cell shape changes.

2

Quantifying septin self-assembly by electron microscopy-based mass mapping

Septins are a conserved family of proteins that form an essential component of the cytoskeleton in yeast and animal cells. Purified septins from diverse organisms are able to form filamentous structures including paired filaments, bundles, and rings. The molecular mechanisms that drive filament assembly and that determine what structure forms remain poorly understood. In this chapter we combine fluorescence and electron microscopy to compare the ability of septins obtained from two different model organisms (budding yeast and fruit fly) to form filaments. We show that fly septins form thick and rigid bundles above an onset concentration of 200 nM, whereas yeast septins form thin and semiflexible paired filaments. We use Scanning Transmission Electron Microscopy (STEM) to measure the mass-length ratio of these filaments and bundles. We find that yeast septins form paired filaments, consistent with prior findings, whereas fly septins form bundles with tapered ends. At a concentration of 500 nM, these bundles reach widths of 250 nm and contain hundreds of subunits per cross-section. Close to the onset concentration for bundling, fly septins instead form two distinct bundle types, namely tapered bundles with tens of subunits per cross-section and even thinner bundles of 6-8 subunits per cross-section with a constant width of ~60 nm and a characteristic groove along the long axis. By correlating width and mass-length ratio measurements, we find that septin bundles flatten on the electron microscopy grid. Topographic imaging of septins by atomic force microscopy confirms that septins have a tendency to flatten upon surface adsorption and drying. Our findings show that a combination of STEM with mass mapping analysis is a powerful tool for future studies of the self-assembly mechanism of septins in the absence and presence of regulatory factors.

2.1 Introduction

Septins are a highly conserved family of GTP-binding proteins in yeast and animal cells, with essential functions in many cellular processes ranging from cell division and migration to tissue morphogenesis [7]. Accordingly, septin dysfunctions are linked to a wide spectrum of diseases, including cancer, neurodegenerative disorders and infertility [72–74]. Septins are present in cells as rod-shaped oligomeric complexes that join endwise to form single filaments, which laterally associate into so-called paired filaments [23]. These filaments in turn form a variety of higher-order structures such as bundles, rings or cages, often in association with the plasma membrane and the actin or microtubule cytoskeleton [15, 16, 75]. Due to their filamentous nature and their association with the cytoskeleton, septins are often referred to as the fourth component of the cytoskeleton, complementing actin filaments, microtubules and intermediate filaments [7].

The cellular functions of septins are best-understood in budding yeast (*Saccharomyces cerevisiae*), where they were first discovered [17]. Mitotic yeast cells express four essential septins, referred to as Cdc3, Cdc10, Cdc11, and Cdc12, and one nonessential septin, known as Shs1. The four essential septins form a symmetric octamer with the palindromic order Cdc11-Cdc12-Cdc3-Cdc10-Cdc10-Cdc3-Cdc12-Cdc11 [19, 76–78]. The terminal Cdc11 subunits can be replaced by Shs1 [77, 79]. Electron microscopy of yeast cells revealed that septins form filaments on the plasma membrane at the mother-bud neck [78, 80–82]. These filaments form higher-order networks that are remodeled during the cell cycle [83]. Septin mutations that block filament formation lead to impaired cytokinesis and cell death, suggesting that the ability of septins to form filaments is essential for their functions in yeast [33]. High resolution microscopy studies of native and recombinant purified septins have provided key insights into the molecular mechanism of filament assembly. Under low-salt conditions (<150 mM KCl), Cdc11-capped septin octamers assemble endwise into long filaments, which zipper up into paired filaments [19, 78, 84]. Pairing is mediated by coiled coil formation by the carboxy-terminal extensions of Cdc3 and Cdc12 subunits on neighboring filaments [19, 85, 86]. By contrast, Shs1-capped septin octamers form small (400 nm) rings, arcs, and spirals [79, 87]. Membrane-binding has a catalytic effect on filament assembly [61, 62]. The assembly state and dynamics of yeast septins in the cell are regulated by posttranslational modifications and by interactions with various septin-binding proteins via mechanisms that are only partially understood [69, 79, 88].

The molecular basis of the functions and assembly mechanism of septins in animal cells is much less well understood than in yeast. Fluorescence imaging of septins in cultured cells typically shows septin structures that look filamentous, but the precise organization of these filaments has been difficult to resolve because they are always found in close proximity to the plasma membrane and/or to actin filaments or microtubules. Ring-shaped septin structures in the proximity of the plasma membrane are present at the base of cilia, sperm flagella, and the dendritic

spines of neurons [50, 89, 90]. Septins are also found in flat regions of the cell cortex in cultured cells and in epithelial tissues, but it is unclear whether cortical septins form filaments [48, 49, 91–93]. It is furthermore unclear whether cortical septins are associated with the plasma membrane or with the cortical actin. During cytokinesis, septins form a ring-shaped structure that co-localizes with the actin-myosin contractile ring [53]. In interphase cells, a subset of septins form linear structures that co-localize with actin stress fibers [37, 43, 53, 94–96]. A recent single-molecule imaging study of human osteosarcoma U2OS cells showed that this septin subset forms thick bundles comprised of 25 to 150 filaments [97]. In many cells, another subset of septins is co-localized with the microtubule cytoskeleton. There are observations of ring-shaped septin structures associated with microtubules at the cell cortex of nonadherent cells [98] and of linear septin structures co-aligned with microtubules in adherent cells [99–102]. It has been suggested that septins require actin filaments and microtubules as a template to form these filamentous structures, based on observations of septin depolymerization upon pharmacological disruption of actin or microtubules [37, 94, 103, 104]. Biochemical reconstitution studies have shown that septins do indeed directly associate with actin and microtubules [43, 53, 54, 105, 106]. In addition, septins interact with both cytoskeletal filaments through adaptor proteins such as anillin, Borg, nonmuscle myosin-2 and microtubule end-binding proteins [71, 94, 95, 107].

In addition to technical difficulties of resolving the precise organisation of septins in the dense cortical and cytoskeletal networks of animal cells, two other factors have made it difficult to dissect the molecular mechanisms of assembly. First, there are multiple septin genes and protein isoforms (in mammals, for instance, 13 genes encode more than 30 protein isoforms), which are expressed in a cell-type specific and developmentally regulated fashion [108]. Based on sequence similarity, the septins can be divided into four subgroups, named SEPT2, SEPT3, SEPT6, and SEPT7 [23]. Septins from different subgroups assemble in a combinatorial manner into hexameric and octameric complexes that can possess different compositions [22, 35–37]. Second, septin assembly is regulated by multiple posttranslational modifications and by septin-binding proteins [26, 27, 45, 109].

Given this complexity, there is a clear need for cell-free reconstitution studies to dissect the molecular mechanisms of septin assembly. Until now, there have only been a handful of studies of native and recombinant septin complexes from various invertebrate and vertebrate species. Recombinant frog (*Xenopus laevis*) septins were shown to form paired filaments, similar to yeast septins [110]. Recombinant nematode (*Caenorhabditis elegans*) septins were shown to form single (unpaired) filaments when purified from bacteria and bundles when purified from insect cells [20]. Native and recombinant fly (*Drosophila melanogaster*) septins composed of Pnut, Sep2 and Sep1 were shown to form thin filaments at low concentrations [21, 111–113] and bundles at higher concentrations [21, 53]. Recombinant human septin hexamers composed of SEPT6, SEPT6, and SEPT7 purified from bacteria were also shown to form bundles [53]. Intriguingly, recombinant human septin

hexamers purified from insect cells were reported to form bundles that transformed into rings and spirals after prolonged (24 hours) incubation [94]. Native human septin hexamers and octamers were recently shown to form a variety of filamentous structures, including thin filaments, thick bundled filaments, rings and half rings [35].

In this chapter, we perform a comparative analysis of the self-assembly behavior of recombinant animal and yeast septins using fluorescence and electron microscopy. We focus on septin hexamers from the invertebrate animal model system *Drosophila melanogaster*. This model system has the advantage of being genetically tractable, which facilitates the connection of *in vitro* studies to the phenotype *in vivo* during different tissue morphogenetic events. The fly has five septins divided in three homology subgroups, which form hexameric complexes. Here we focus on hexamers composed of Pnut, DSep1, and DSep2, which have previously been studied both *in vivo* [53, 114–116] and *in vitro* [21, 53, 111]. We first use fluorescence microscopy to screen the self-assembly behavior of septins as a function of their concentration and to test the filament stability. We then turn to scanning transmission electron microscopy (STEM) to investigate the molecular packing structure of the bundles.

STEM is uniquely capable of measuring the mass of supramolecular protein assemblies at high spatial resolution [117, 118] and was previously used to measure the molecular packing density of several filamentous proteins including actin, intermediate filaments and collagen [119–122]. The basic idea is to raster-scan a tightly focused beam of electrons across an EM grid with adsorbed proteins and to collect the elastically scattered electrons with an annular detector that captures the dark-field (high-angle) signal [123]. The dark-field STEM signal in each image pixel is proportional to the projected specimen mass [124, 125]. STEM combines a large dynamic range for mass measurements (from a few tens of kDa to hundreds of MDa) with a high spatial resolution of 2-4 nm [126].

2.2 Materials and methods

2.2.1 Septin complex purification

Recombinant yeast septins purified from bacteria according to a published procedure [19] were a kind gift from Dr. Aurélie Bertin (Institut Curie, Paris, France). We used septin octamers without a fluorescent label (comprised of Cdc3, Cdc10, Cdc11 and His_6-Cdc12) and octamers labeled with GFP on the N-terminus of Cdc3. The septins were provided in 50 mM Tris-HCl buffer (pH 8) supplemented with 300 mM KCl to prevent filament assembly. Prior studies have shown that yeast septin octamers form filaments at KCl concentrations below 150 mM [19, 87].

Recombinant fly septin hexamers were expressed and purified from bacteria in-house, following a published protocol [53] with small modifications. In order to obtain stoichiometric hexameric septin complexes, we co-expressed the three fly

septins (His_6-DSep1, DSep2 and Pnut-Strep) on two separate plasmids. Moreover, we made sure to isolate full-length complexes and remove substoichiometric septin complexes by using a two-tag affinity purification scheme. The central subunit of the hexamer (DSep1) with a TEV-cleavable 6xHis-tag fused to its N-terminus was expressed on a pnEA-vH vector under the control of the T7 promoter. The other two septin genes (DSep2 and Pnut) were expressed on a pnCS vector under the control of a single T7 promoter. The C-terminus of Pnut was fused to a noncleavable eight-amino-acid Strep-tag II (WSHPQFEK, 1058 Da). GFP-labeled septin complexes for fluorescence microscopy were constructed in the same manner, replacing DSep2 by DSep2 with mGFP fused to its N-terminus.

Escherichia coli BL21(DE3) competent cells (200131, Agilent Technologies) were co-transformed with the two plasmids encoding all three septin genes and grown overnight at 37°C on LB agar (Sigma) plates containing the antibiotics ampicillin and spectinomycin (Sigma) at 100 µg/mL. Precultures of single colonies were obtained by growing the cells at 37°C for 12-16 hr in a shaking incubator in LB medium (Sigma) supplemented with 100 µg/mL ampicillin and spectinomycin. Co-transformed bacteria were stored in a 50% v/v glycerol stock at -80°C. Large scale cell cultures for dark septins were grown in Terrific Broth (Sigma) with 50 µg/mL antibiotics at 37°C until the optical density at 600 nm (OD600) reached a value of 2-3, before induction with 0.5 mM isopropyl β-D-1-thiogalactopyranoside (IPTG). Cell cultures for GFP-labeled septins were grown at 37°C to a lower density (OD600 in the range of 0.6-0.8) before expression was induced at 17°C overnight (16 hr), conditions chosen to minimize protein degradation and allow GFP to fold. Cells were collected by centrifuging at 2,800 g and 4°C for 10 min. The bacterial pellets were lysed on ice with a tip sonicator in *lysis buffer* (50 mM Tris-HCl pH 8, 500 mM KCl, 10 mM imidazole , 5 mM $MgCl_2$, 20 mM $MgSO_4$, 0.1 mM guanosine diphosphate (GDP), 5% glycerol) containing 0.25 mg/mL lysozyme (5934-D, Euromedex) for lysis, 1 mM phenylmethylsulfonyl fluoride (Sigma) and Complete™protease inhibitor cocktail (11697498001, Roche) to prevent protein degradation, and 10 mg/L DNAse (DNAse I, Sigma) to remove DNA. We used 100 mL of lysis buffer for a bacterial pellet from a 6 L culture. The lysate was clarified by centrifugation at 20,000 g for 30 min at 4°C.

Contrary to the original protocol, we first ran the supernatant on a streptavidin affinity column (Streptrap™HP 5ml, GE Healthcare) and then on a nickel affinity column (HisTrap FF crude column, 17-5286-01, GE Healthcare). Furthermore, we used a 5 mL Streptrap column instead of the 2 × 1 mL tandem columns used in the original protocol to avoid overpressure. The Streptrap column was equilibrated with *septin 1* buffer (50 mM Tris-HCl pH 8, 300 mM KCl, 5 mM $MgCl_2$, 5% glycerol buffer) and complexes containing Pnut-Strep were eluted with septin 1 buffer supplemented with 2.5 mM desthiobiotin. Fractions contained in the elution peak were pooled and loaded on the HisTrap column equilibrated with *septin 2 buffer* (50 mM Tris-HCl pH 8, 500 mM KCl, 10 mM imidazole pH 8, 5 mM $MgCl_2$, 5% glycerol). Nonspecifically bound protein was washed off with septin 2 buffer

containing 20 mM imidazole. Next, septin complexes containing His_6-DSep1 were eluted with septin 2 buffer containing 250 mM imidazole. Fractions contained in the elution peak were pooled and dialyzed against *storage buffer* (50 mM Tris-HCl pH 8, 300 mM KCl, 5 mM $MgCl_2$, 5% glycerol, and 5 mM of the redox reagent dithiothreitol (DTT)) at 4°C overnight and subsequently concentrated using Vivaspin 6 concentrators (Sartorius, 6 ml, 100MWCO). We did not perform additional size exclusion chromatography, contrary to the original protocol [127], to increase the yield and avoid excessive dilution.

Purified septin complexes in storage buffer were flash-frozen in liquid nitrogen and stored in small aliquots at -80°C. We typically obtained 0.5-1 mg of septin hexamers, which we concentrated to 10-15 µM (about 3-5 mg/mL).

2.2.2 Protein characterization

We determined the final concentration of septin complexes by measuring the optical absorbance over a range of wavelengths from 220 to 750 nm with a UV-VIS spectrophotometer (Thermo Scientific, Nanodrop 2000). We inferred the septin concentration from the absorbance at 280 nm, after subtraction of the scattering contribution [128]. To obtain the scattering contribution at 280 nm, we fitted the absorbance data in the wavelength range of 320-340 nm, where the protein absorbs negligibly, to a Beer-Lambert law with exponent -4 and used this fit to extrapolate to 280 nm. The scattering contribution was typically on the order of 2-3%. We used extinction coefficients of 0.545 $L.g^{-1}.cm^{-1}$ for dark Drosophila septins and 0.584 $L.g^{-1}.cm^{-1}$ for mGFP-tagged septins, both calculated from the amino acid sequences (including the His-, Strep, and GFP tags) using the SIB Bioinformatics Resource Portal ExPASy [129]. Molar concentrations can be converted into weight concentrations using the calculated molecular weights (including tags) of 306.9 kDa for dark septins and 361.1 kDa for mGFP-tagged septins.

The purity and integrity of the proteins was evaluated for each batch by sodium dodecyl sulfate polyacrylamide gel electrophoresis (SDS-PAGE) using 4-15% gels (Mini-PROTEAN® TGX™Precast Protein Gels, Bio-Rad). For a reference of protein sizes we used a protein standard (Precision Plus Protein™Kaleidoscope™, Bio-Rad). The example gel shown in Fig. 2.1 reveals three bands of similar intensity at positions that are consistent with the expected molecular weights of the three subunits, Pnut-Strep (61.2 kDa), DSep2 (48.5 kDa) and His_6-DSep1 (43.8 kDa). We also observe smaller bands in between the DSep2 and Pnut bands, which were previously identified by mass spectrometry as partially degraded Pnut-Strep units [53], and a faint band located around 70 kDa that was identified as the bacterial chaperone DnaK [127].

The quality of each septin preparation in terms of hexamer content was evaluated by transmission electron microscopy. Solutions of septins diluted to 65 nM (high salt) or 163 nM (low salt) were deposited on glow discharged carbon coated copper grids (CF300-Cu, Electron Microscopy Sciences) and incubated for at least 30 min. The

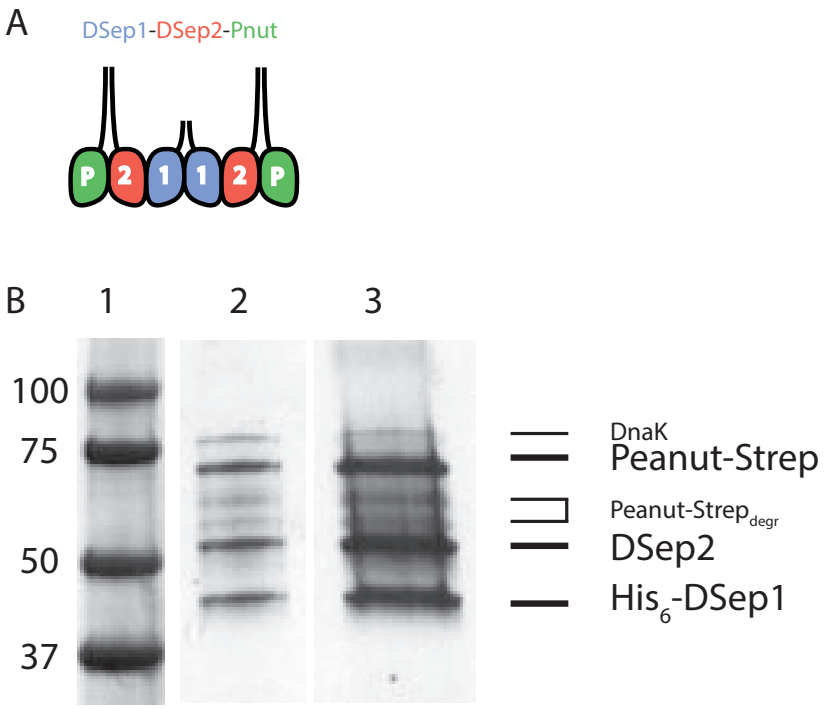

Figure 2.1: SDS PAGE of purified septin complexes. (A) Schematic depiction shows the palindromic arrangement of Pnut, DSep1 and DSep2 in fly septin hexamers. The Pnut subunits have traditionally been thought to form the terminal subunits on the basis of the homology between fly and human (hSep2, hSep6, hSep7) septin hexamers, for which a crystal structure is available [34]. However, two recent preprints challenge this view and show evidence for an alternative subunit arrangement for human septin hexamers, which would imply that the Pnut subunits are actually in the center [35, 36]. (B) SDS PAGE, with the numbered lanes showing (1) A reference marker (in kDa), (2) the Strep column eluate, and (3) the Nickel column eluate.

samples were negatively stained with 2% uranyl acetate (Nanoprobes) and air-dried. The samples were examined with a FEI Tecnai Spirit (120 kV) electron microscope at the Institut Curie by Dr. A. Bertin. Under high-salt conditions (300 mM KCl), we observed rod-shaped oligomers that were predominantly octameric given their characteristic length of ~24 nm. Under low-salt conditions (50 mM KCl), the fly septins formed bundles, consistent with prior studies [53]. A typical example of purified fly septins imaged by TEM is presented in Fig. 2.2. Similar bundles are also observed for human septin hexamers, both by negative stain EM [53] and by cryoEM (see Figure S1).

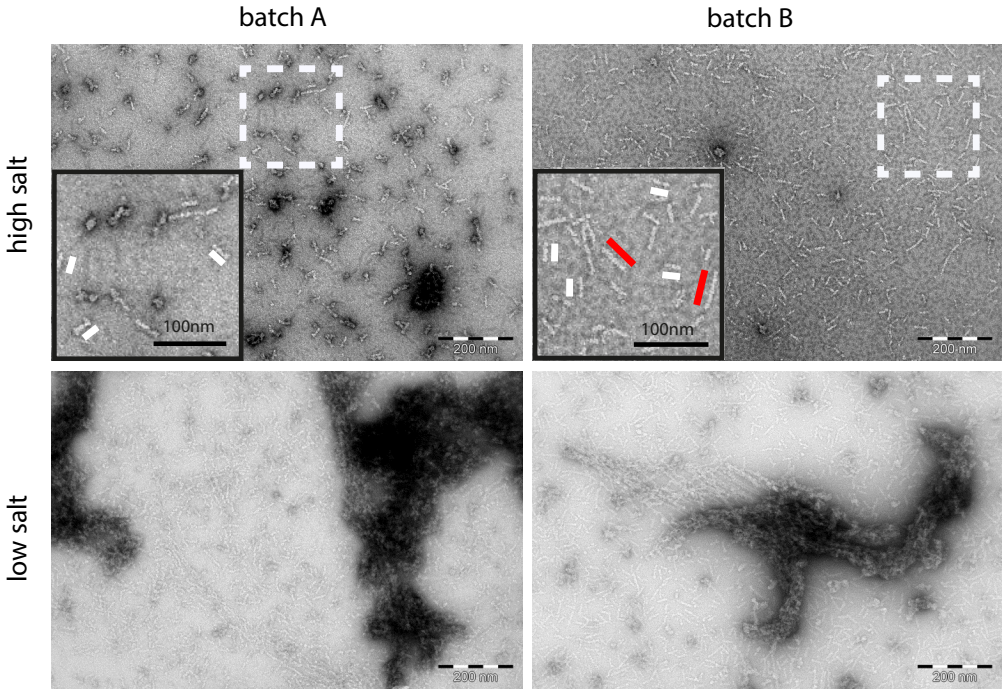

Figure 2.2: Evaluation of the quality of fly septin hexamer preparations by transmission electron microscopy (TEM). Examples of two septin batches evaluated by negative stain TEM imaging. Upper panel: Septins in high salt (300 mM KCl) form predominantly hexamers (white lines correspond to hexamer length). Oligomers of hexamers are also present (red lines correspond to double hexamer length). Lower panel: Septins in low salt (50 mM KCl) form bundles. Septin complexes are still present in the background. The dark patches are staining artifacts.

2.2.3 TIRF imaging of septins

2.2.3.1 Sample preparation

Cover slips and microscope slides were cleaned and rendered hydrophilic in base Piranha solution (5% hydrogen peroxide, 5% ammonium hydroxide) at 70°C and stored in miliQ water for up to 3 days. Just before use, a slide and a cover slip were blow dried with a stream of N_2 gas. Flow channels were prepared by cutting strips of parafilm with a width of ~2 mm and placing these pairwise between the slide and cover slip, spaced by a distance of about ~2 mm. The parafilm was fixed in place by placing the chambers on a hotplate at 120°C until the parafilm melted and then cooling down.

For most of the total internal reflectance fluorescence (TIRF) microscopy experiments, we used DOPC (18:1 1,2-dioleoyl-*sn*-glycero-3-phophocholine) lipid bilayers as the surface passivator (the preparation procedure is described in Chapter

3). We confirmed by TIRF imaging and QCM-D measurements (shown in Chapter 4) that fly septins do not bind to the DOPC lipid bilayer. For comparison, we also tested septins on glass passivated with dichlorodimethylsilane (DDS) [130]. Surface passivation was carried out by incubating slides and cover slips in a custom-designed Teflon box filled with 250 mL trichloroethylene (TCE) and 125 µL of DDS for 1 hr. Next, the slides and coverslips were transferred to a Teflon holder placed in a beaker with methanol and sonicated for 15 min. The glass was thoroughly rinsed by at least 3 washes in a beaker with milliQ water, dried with N_2 gas, and stored in a closed glass container for up to 1 month. Just before use, we incubated the DDS passivated channels for 5 min with 1 wt% Pluronic F127 (in septin assembly buffer, see below) [130], which strongly adsorbs onto the hydrophobic surfaces and renders them nonadhesive. We then washed the channels with approximately 3 channel volumes of septin assembly buffer.

Fly septins were assembled at concentrations between 50 and 500 nM in *assembly buffer* (20 mM imidazole pH 7.4, 1 mM DTT, 0.1 mM MgATP, 50 mM KCl and 2 mM $MgCl_2$), supplemented with 2 mM trolox to suppress blinking [131] and with an oxygen scavenging system of 2 mM protocatechuic acid and 0.1 µM protocatechuate 3,4-dioxygenase to minimize photobleaching [132, 133], for 30 minutes and at 20°C, unless stated otherwise. The septins were fluorescently labeled by co-polymerizing dark septins with 10 mole% of GFP-septins, which is a small enough mole fraction that assembly is not noticeably influenced. For mole fractions of GFP-septins of 50% and above we observed aberrant structures (see Fig. S2 in the Supporting Information). Yeast septins were assembled at a concentration of 20-40 nM in the same assembly buffer, but with pH 8, for 30 minutes and at 20°C, unless stated otherwise.

To observe the septin bundles in the evanescent field of the TIRF microscope, we confined them to a thin layer close to the surface by including the crowding agent methylcellulose in the buffer at a concentration of 0.1 wt%. We sealed the channels with Valap (a mixture of equal amounts of vaseline, lanolin, and paraffin wax) to prevent solvent evaporation.

2.2.3.2 Imaging and data analysis

Septin bundles were imaged with a Nikon Eclipse Ti-E inverted microscope equipped with a TI-TIRF-E motorized TIRF Illuminator (Roper Scientific), a Nikon Apo TIRF 100x/1.49 N.A. oil immersion objective, and a 491 nm/50 mW Calypso laser (Cobolt, Solna, Sweden). Images were acquired with a QuantEM 512SC EMCCD camera (Photometrics, Roper Scientific, Tucson, AZ, USA) using an exposure time of 50 ms. The microscope was controlled with MetaMorph 7.5 software (Molecular Devices, Sunnyvale, CA, USA). Image processing (specifically, contrast enhancement and look-up table inversion) was performed using Fiji software [134].

2.2.4 Mass mapping by STEM

To convert the intensity in each image pixel to the mass-per-length (MPL) of the septin filaments, we imaged septins together with tobacco mosaic virus (TMV) rods as an internal mass standard [135]. The TMV virus has a well-defined length (300 nm), width (18 nm) and MPL (131 kDa/nm) [136]. Samples for mass mapping were prepared on carbon or formvar+carbon coated copper grids (Ted Pella, Redding, CA, USA). First, 3 µL of a 0.01-0.02 mg/ml dispersion of TMV rods in phosphate-buffered saline (a kind gift from Dr. Jean-Luc Pellequer from the Institut de Biologie Structurale, Grenoble, France) was incubated on the grid for 30 s. Next, the grid was washed with 3 × 5 µL of milliQ water and blotted with filter paper to remove excess water. Then, 5 µL of a solution of septins preassembled for 1 hr at 20°C (at a concentration between 50 and 500 nM in case of fly septins, or 50 nM in case of yeast septins) was deposited on the grid. After a 1 min incubation, the grids were washed twice with 5 µL of MilliQ water to remove excess salts and left to dry in air at 37°C.

The grids were imaged with a FEI Verios 460 STEM microscope. Images of 3072 × 2207 pixels (16 bits) were acquired at different magnifications in the range of 15000-50000× and at an acceleration voltage of 10 to 20 kV, a current of 100 pA, and a pixel dwell time of 3 to 5 µs. We first performed a search for a region of interest at low magnification to avoid sample damage and next increased the magnification and optimized the contrast so as to cover the full dynamic range of the detector. All images used for quantitative mass analysis were acquired during the first scan of the sample.

The images were analyzed manually using Fiji [134] following a previously published procedure [136]. Briefly, images containing both TMV rods and septin bundles were selected. For intensity calibration, boxes with a width of 25 to 45 nm (depending on the image resolution) and a length of 100 nm were drawn along the TMV rods, to obtain the protein signal, and on both sides of each rod, to obtain the background signal (see Fig. 2.3). The integrated intensities of at least three TMV rods per image were averaged and the calibration factor K was determined according to:

$$K = \frac{131}{\frac{I_{\mathrm{TMV}}}{L}} \left[\frac{kDa}{counts}\right] \tag{2.1}$$

Here I_{TMV} is the total intensity in the box containing a segment of the TMV rod after background subtraction, L is the box length (100 nm), and 131 kDa/nm is the known MPL value of TMV [136]. After obtaining the calibration factor, a similar procedure was used to obtain the MPL of septin bundles: boxes were drawn over the bundles that encompassed their width (20 to 50 nm), together with equal-sized boxes on both sides of each bundle for background subtraction. The MPL of the septin bundle was next determined according to:

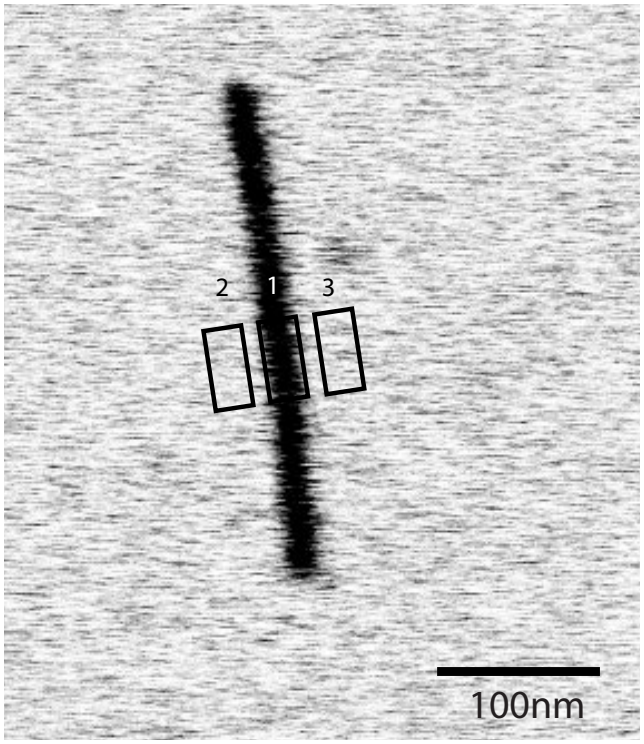

Figure 2.3: Procedure for quantitative mass mapping by STEM of septins by intensity calibration with TMV rods. Contrast-inverted STEM image of a TMV rod together with numbered boxes representing: (1) a box encompassing a TMV rod, and (2,3) two boxes of the same size on both sides of the rod for background subtraction.

$$MPL = K \times \frac{I_{\text{fibril}}}{L} \left[\frac{kDa}{nm} \right] \tag{2.2}$$

Here, I_{fibril} is the total intensity in the box containing a segment of a septin fibril or bundle after background subtraction and L is again the box length (100 nm). The width of the septin bundles was measured by drawing a line (using the line tool in Fiji) across the bundles in each region where the MPL was calculated and measuring its length, where the edges were defined by eye.

2.2.5 Atomic force microscopy (AFM)

Fly septin bundles were polymerized in *assembly buffer* at a concentration of 500 nM for 30 min at room temperature. For imaging in air, 10 µL of sample was deposited on freshly cleaved mica (Ted Pella) and directly washed with *assembly buffer* by replacing the liquid with a pipette. The sample was dried with an air gun. Images were acquired in contact mode with a Veeco Dimension 3100 Scanning Probe Microscope (Bruker), using a DNP-C cantilever with a nominal spring constant of 0.24 N/m and a triangular tip with a nominal radius of 20 nm (Bruker). Images with

a scan resolution of 512 × 512 pixels over an area of 50 × 50 µm were recorded at a scan rate of 1 kHz. For imaging in liquid, 50 µl of sample was deposited on freshly cleaved mica (Agar Scientific Ltd) and directly washed with *assembly buffer* by replacing the liquid with a pipette and kept wet till use. Images were acquired in *assembly buffer* and in peak force tapping mode with Nanoscope Multimode 8 Scanning Probe Microscope (Bruker), using a DNP-B cantilever with a nominal spring constant of 0.12 N/m and a triangular tip with a nominal radius of 20 nm (Bruker). Images with a scan resolution of 512 × 512 pixels over an area of 20×20 µm and 7x7 µm were recorded at a scan rate of 0.9 Hz with a tapping amplitude of 50 nm and driving frequency of 2 kHz. Images were third-order flattened using the open source software Gwyddion [137].

2.3 Results

2.3.1 TIRF microscopy investigation of septin polymerization

To investigate the ability of fly septin hexamers to form filamentous structures, we performed TIRF imaging of septins after rapid dilution from a high salt *storage buffer* (containing 300 mM KCl) to a low salt *assembly buffer* (containing 50 mM KCl), which has previously been shown to promote fly septin polymerization [53]. To enable septin visualization, we co-polymerized dark septin hexamers with 10 mole% GFP-labeled hexamers. This labeling percentage is high enough to provide a homogeneous fluorescent signal along the bundles, yet low enough so as not to influence septin polymerization. We noted that labeling percentages of 50% and higher severely impaired bundle formation (Fig. S2), perhaps due to steric hindrance between adjacent GFP-tagged subunits. To enable observation of septins in the thin evanescent TIRF field, we polymerized septins in the presence of the crowding agent methylcellulose that pushes septins towards the surface. To prevent surface adhesion, we tested two different types of passivation: a DDS coating and a neutral DOPC lipid bilayer.

As shown in Figure 2.4A, the fly septin hexamers formed rigid bundles on DDS-coated glass (left image) as well as on DOPC-coated glass (middle image). The bundles freely moved through translational and rotational diffusion, confirming that they do not interact with the surface. The bundles were rather straight and did not exhibit measurable thermal bending undulations, indicating that they are stiff. To prove further that the surface did not affect bundle formation, we compared septin bundles polymerized directly in the channel for 30 min with prepolymerized bundles, flushed into the channel after 30 min of polymerization in an Eppendorf tube (right-hand image in Figure 2.4A). In both cases, we observed bundles with similar shapes and sizes, confirming that the surfaces do not affect assembly. The fly septins polymerized very rapidly at a concentration of 500 nM: they were already formed within the 2 min time window needed to mount the sample on the microscope and

did not further increase in length or number over time (Fig. S3A). This observation suggests that the septin-septin interactions that drive bundle assembly are very strong. Consistent with this idea, fluorescence recovery after photobleaching measurements, where we locally photobleached septins with high intensity light and monitored the recovery of the fluorescence intensity with low intensity light, showed that the septin bundles displayed negligble subunit exchange (Fig. S4). When we lowered the septin concentration to 200 nM, bundles still formed rapidly, but they were shorter than the bundles formed at 500 nM (Fig. 2.5, middle). We did not observe any filamentous structures at concentrations below 200 nM (Fig. 2.5, left), consistent with prior evidence based on electron microscopy that only hexamers are present at 100 nM [53].

For comparison, we also imaged yeast septin octamers after rapid dilution from a high salt storage buffer to a low salt assembly buffer. We used the same assembly buffer as for fly septins except for the pH, which was 8 instead of 7.4. The yeast septins formed filaments that were thinner (of lower intensity) and more flexible compared to the rigid bundles formed by fly septins (Fig. 2.4B). This observation is consistent with prior reports showing that yeast septins form thin semiflexible filaments with a persistence length of 8 to 10 μm [19, 41, 61, 77]. At a concentration of 20 nM, filaments appeared a few minutes after the initiation of polymerization by rapid dilution. In time, the filaments grew in length and number, leading to dense and entangled networks (Fig. S3B). Again, septin filaments looked identical irrespective of whether they were polymerized inside the channel or in an Eppendorf tube (see Fig. 2.4B, right), indicating that the passivated surface of the flow cell does not affect the polymerization process.

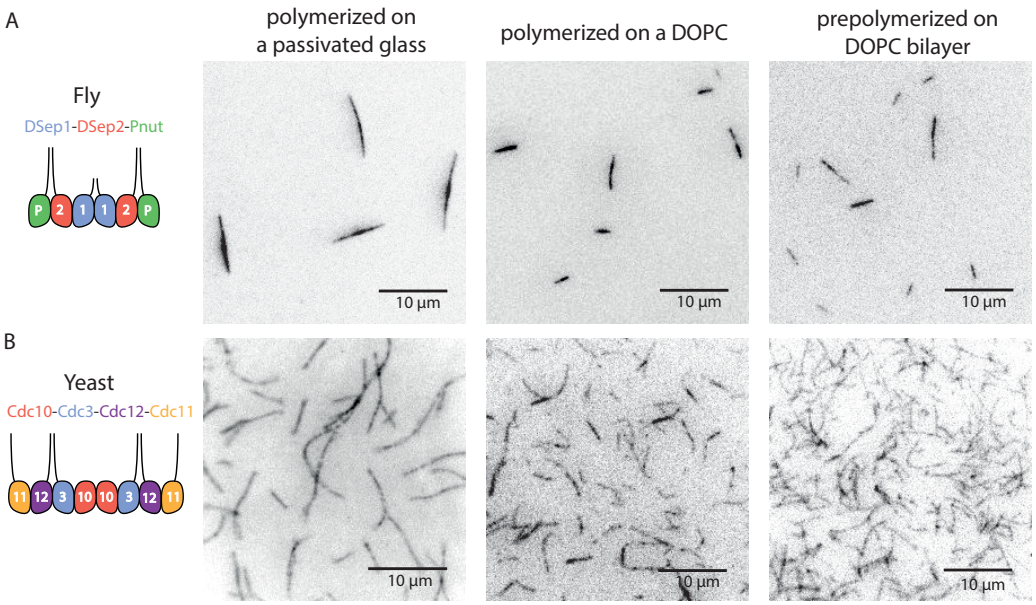

Figure 2.4: TIRF imaging shows that fly septin hexamers form rigid bundles, whereas yeast septin octamers form thin semiflexible filaments. Schematic depictions of the subunit compositions are shown on the left, and contrast-inverted TIRF images of the GFP-tagged septins after 30 min polymerization are shown on the right. (A) Fly septins (500 nM) polymerized on a glass surface passivated with DDS (left) or with a DOPC bilayer (middle), and prepolymerized before flushing onto a DOPC bilayer (right). (B) Yeast septins polymerized on a glass surface passivated with DDS (left, (10 nM) or with a DOPC bilayer (middle, 20 nM), and prepolymerized (20 nM) before flushing onto a DOPC bilayer (right).

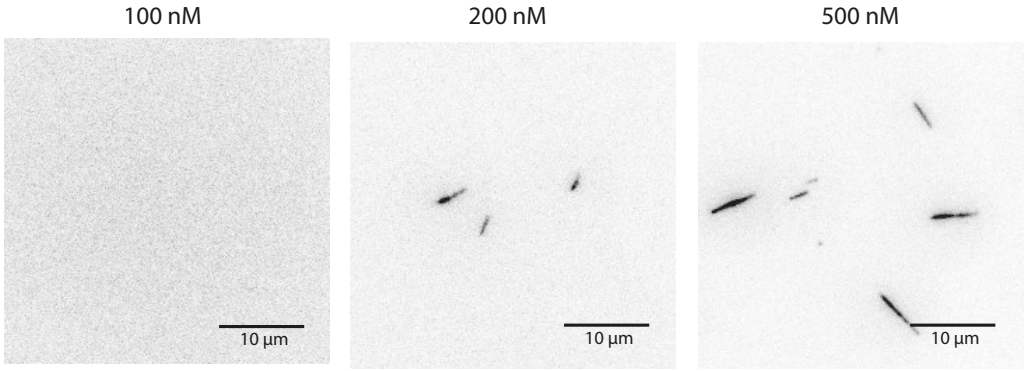

Figure 2.5: Concentration dependence of fly septin bundle formation. TIRF images (inverted contrast) show septins polymerized for 15 min on a DOPC bilayer. No filamentous structures were observed at 100 nM (left), sparsely distributed short bundles were observed at 200 nM (middle), and thick septin bundles were present at 500 nM (right).

2.3.2 Mass mapping of septin filaments and bundles

With TIRF microscopy we could not measure how thick the septin filaments and bundles are, due to limitations posed by the optical diffraction limit. We therefore decided to use STEM microscopy, which provides high spatial resolution and furthermore has the advantage of providing quantitative measurements of the mass per length unit of protein filaments (Fig. 2.6A). We used tobacco mosaic virus (TMV) rods as an internal calibration, as its mass per length is well defined (Fig. 3, for details see Methods). To test the reliability of the mass mapping method, we first investigated yeast septins, since these are already known to form paired filaments based on transmission electron microscopy imaging [19]. Given a length of 33 nm and molecular weight of 383 kDa for a yeast septin octamer [19], the expected mass per length is 23.2 kDa/nm for these paired filaments.

We polymerized yeast septins at a concentration of 20 nM, where TIRF imaging showed the formation of long semiflexible filaments. We aimed to have both TMV rods and septin filaments in the same image, in order to have a reliable calibration of the intensities. As shown in Fig. 2.6B (upper panel), the TMV rods were clearly much brighter in signal than the yeast septin filaments, consistent with their higher MPL (131 kDa/nm) compared to that of septin filaments (23.2 kDa/nm). The histogram in Fig. 2.6 shows that the majority of septin filaments had a MPL close to 20 kDa/nm, consistent with a paired filament arrangement. In rare cases we could directly observe the double-stranded structure in the image (see Fig. 2.6B, lower panel). The railroad track appearance is consistent with prior negative stain electron microscopy studies, which showed two linear strands spaced by 15-25 nm [19]. The spacing has been ascribed to the carboxy-terminal extensions of the Cdc3 and Cdc11 subunits, which mediate filament pairing by coiled-coil formation. The histogram also reveals a population of septin filaments with a MPL of around 10 kDa/nm consistent with single filaments, which have indeed also been observed by transmission electron microscopy [19]. Finally, we observed one filament with a clear axial periodicity in the intensity with a repeat distance of 33 nm that corresponds to the length of a single yeast septin octamer (Fig. 2.6C). This filament had a larger MPL of 38 kDa/nm compared to the other filaments, likely due to lateral association of two paired filaments. The axial periodicity suggests that lateral association occurred in register. The same 33 nm axial periodicity has previously also been observed in negatively stained samples by TEM (Fig. 2.6D, taken from [19]). This periodicity was ascribed to the pairing of the coiled coil regions of Cdc3 and Cdc12 subunits on adjacent filaments, forming a four-helix bundle.

Having confirmed that mass mapping can reliably measure the MPL of yeast septin filaments, we turned to fly septin bundles. STEM imaging of septins polymerized at 500 nM revealed the presence of thick bundles with thin tapered ends, reaching widths of over 250 nm in the middle (Fig. 2.7A and B). Contrary to the yeast septin filaments, the fly septin bundles were brighter than the TMV rods, indicating that they have a larger MPL. Mass mapping revealed that the MPL for

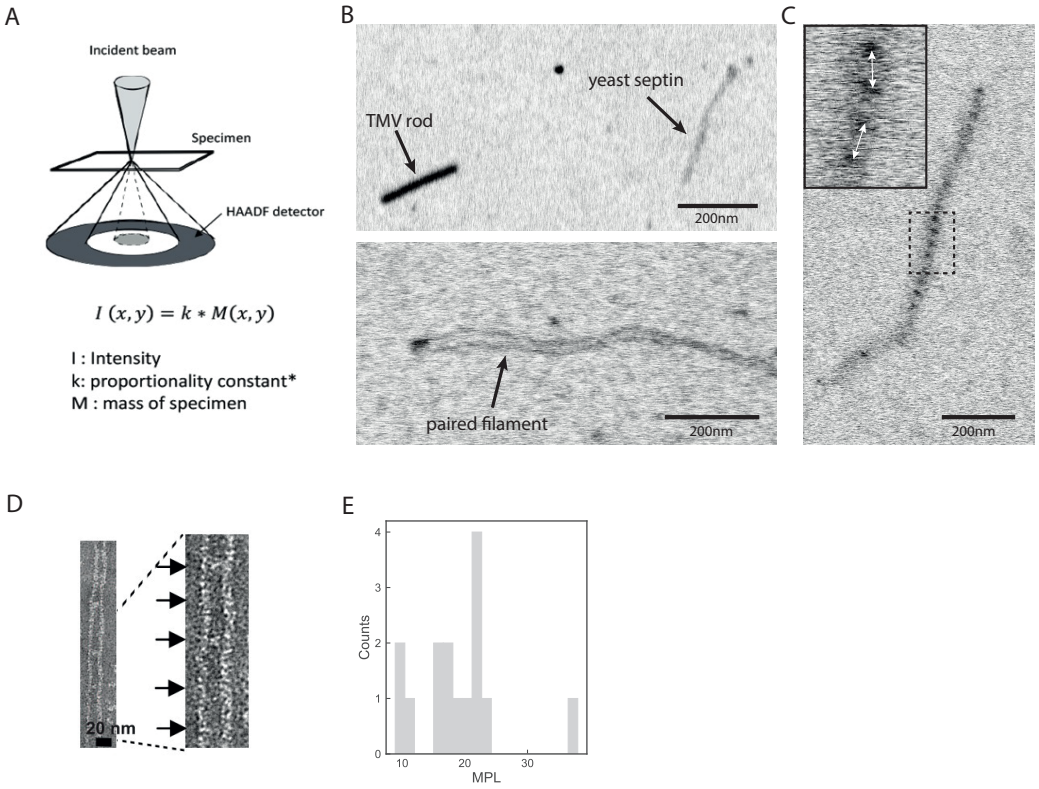

Figure 2.6: Quantitative mass mapping of yeast septin filaments. (A) Schematic diagram of the principle of mass mapping by STEM microscopy. The intensity reaching the annular detector (HAADF) is proportional to the mass of the specimen in the volume illuminated by the focused electron beam. Drawing kindly provided by C. Martinez Torres (B) Upper panel: STEM image showing both a TMV rod and a septin filament (see arrows). Lower panel: Septin filament that is clearly paired. (C) Septin filament displaying a periodic variation in mass-per-length (MPL) along its length. Inset: zoomed-in image, where the white arrows indicate the 33 nm length of a single septin octamer. (D) Previously published TEM images of negatively stained yeast septin filaments (reprinted from [19]), showing a periodic increase in intensity every 33 nm as well as cross-bridges (indicated by black arrows) thought to represent the coiled coils. The paired filament has a spacing between the two filaments of 15 to 25 nm. (E) MPL histogram based on 15 data points pooled together from 3 images and 10 septin filaments. Note that the one data point on the histogram at 38 kDa/nm corresponds to the filament in panel (C). The box length for the MPL analysis was 50 nm and the width was 40 nm, except for the 38 kDa/nm filament for which the box width was 200 nm. Note that the contrast of the STEM images in panels (B) and (C) is inverted.

bundles with a width of 100 nm was on average close to 1000 kDa/nm. Given a MPL of 12.8 kDa/nm for fly septin hexamers (as calculated from their length of 24 nm and molecular weight of 307 kDa/nm [53]), this translates to nearly 80 hexamers per cross-section.

To investigate the molecular packing structure of the bundles, we plotted the MPL as a function of the bundle width (Fig. 2.7C). If the bundles would be hollow single wall tubes or flat arrays, the MPL should increase linearly with increasing width (black dashed line). By contrast, if the bundles would be solid, cylindrical tubes, the MPL should increase quadratically with the width (red dashed line). The data points lie in between these two limiting cases. The bundles are therefore unlikely to be hollow single-wall tubes. They are likely solid bundles that flatten to varying degrees due to surface adhesion. Flattening is a well-known phenomenon for soft protein filaments adhered to a solid substrate [138, 139].

Motivated by the concentration dependence of septin polymerization observed by TIRF imaging, we imaged septins by STEM at concentrations between 50 and 200 nM. Consistent with TIRF imaging, we did not observe any filamentous structures at septin concentrations of 50 or 100 nM by STEM. Also consistent with TIRF imaging, we did observe bundles at a septin concentration of 200 nM, and these looked different from the bundles observed at 500 nM. Strikingly, we observed two different bundle structures at 200 nM. One category of bundles had tapered ends, similar to the bundles observed at 500 nM, but they were substantially thinner. For instance, the bundle shown in Fig. 2.8A in the region indicated by the rectangular box has a width of 31 nm and MPL of 251 kDa/nm, corresponding to around 20 hexamers per cross-section. The second category of bundles did not have tapered ends but had a uniform width of 63 ±1 nm and MPL of 84 ±7 kDa, corresponding to 6-8 hexamers per cross-section (Fig. 2.8B). In some cases these bundles showed a lower mass in the center than at the edges, suggestive of a hollow tube-like structure (Fig. 2.8C). Given the width and MPL of the structure, we suggest that it may be composed of 2 layers of 2 paired filaments, where the second layer is perfectly aligned on top of the first layer (Fig. 2.8D). We note that the number of hexamers (6-8) in the cross-section may indicate that the second septin layer within the bundle is not always fully saturated with hexamers.

As an independent test of the septin bundle width, we also imaged the bundles in air and in buffer by AFM at 500 nM (Fig. 2.9). In both cases, we observed septin bundles with lengths up to 10 μm, consistent with the TIRF results. For samples imaged in air, the widths of bundles were up to 150 nm, consistent with the STEM results. The bundle height was on average around 20 nm (Fig. 2.9C). For samples imaged in liquid, septin bundles were taller and thinner (average height of 27 nm and width of 97 nm). This observation suggest that bundles imaged in liquid do not flatten as much due to surface interactions as bundles imaged in air. Nevertheless, the discrepancy between the bundle height and width even for samples imaged in liquid suggests flattening upon surface adsorption, but the width may also be artificially broadened by tip convolution.

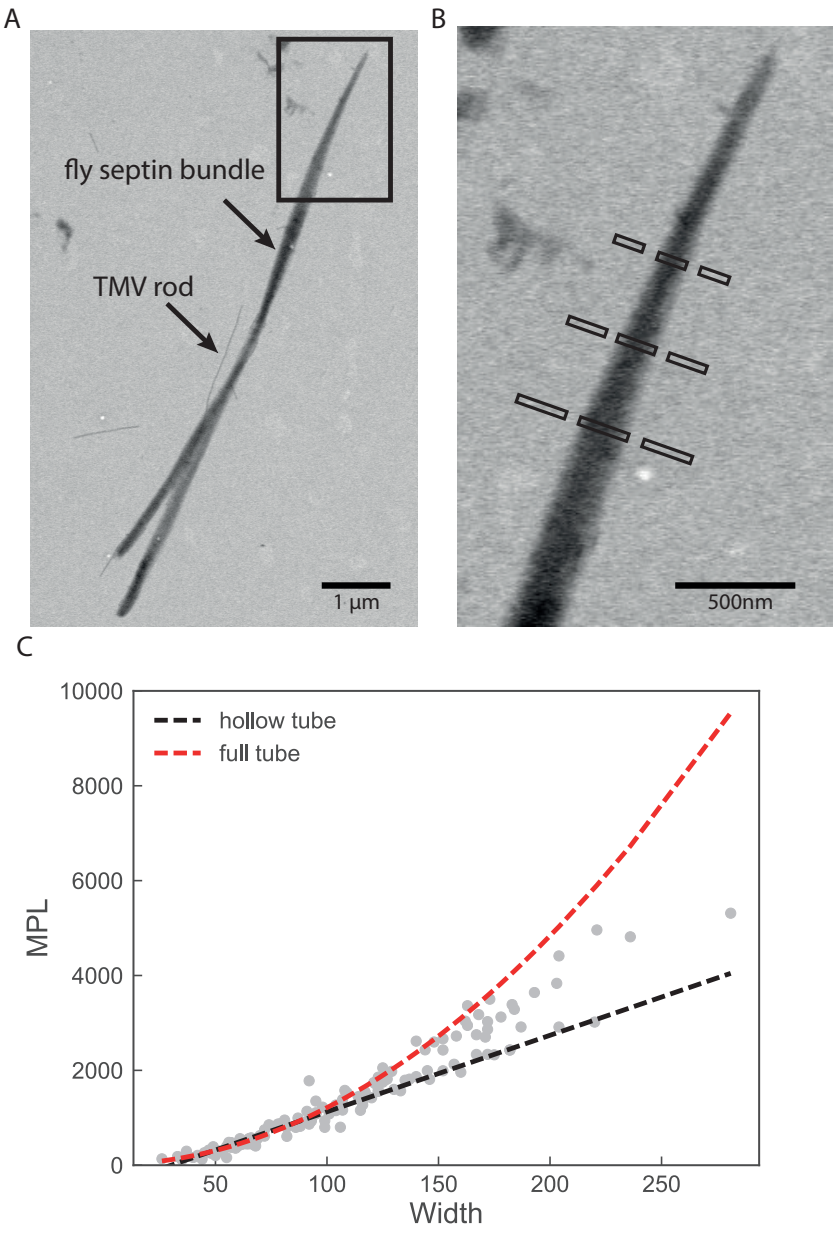
A
fly septin bundle
TMV rod
1 µm
B
500nm
C
10000
8000
6000
4000
2000
0
MPL
hollow tube
full tube
50
100
150
200
250
Width

Figure 2.7 *(preceding page)*: STEM imaging shows that fly septins at a concentration of 500 nM form thick bundles. (A) Example image showing a septin bundle together with three TMV rods (one is indicated by an arrow). (B) Zoomed-in image of the rectangular box in (A), also showing the boxes used for quantifying the intensity of the septin bundle and the surrounding background. (C) Scatter plot of the MPL (in units of kDa/nm) versus the bundle width (in nm). The data were collected from 2 independent imaging sessions, 5 images, 16 bundles, and in total 130 data points. The dotted lines show a linear dependence expected in case of hollow cylinders or flat filament arrays and a quadratic dependence expected for solid cylinders (see legend). The lines are based on fits to small-width (<100 nm) bundles, as in this regime there was the highest number of data points. Note that the contrast of the STEM images is inverted.

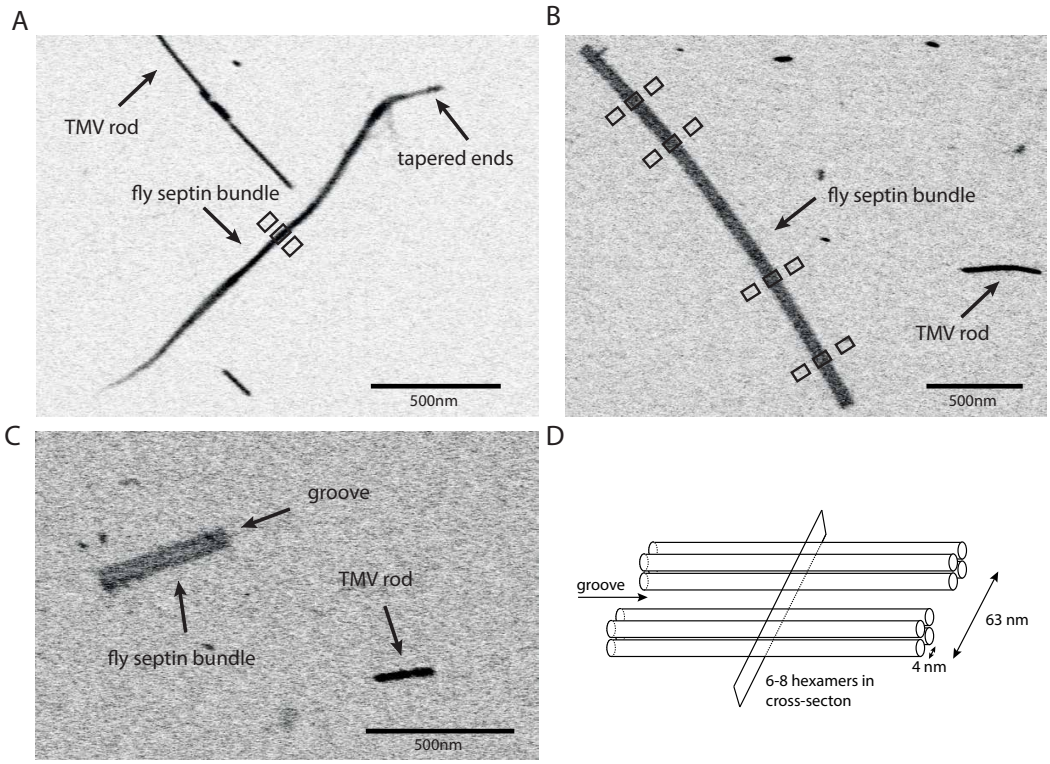

Figure 2.8: STEM imaging shows that fly septins at a concentration of 200 nM form two different types of bundles. (A) An example of a septin bundle with tapered ends. The MPL and bundle width in the region indicated by the rectangle are 251 kDa/nm and 31 nm, respectively. (B) An example of a septin bundle of uniform width and blunt ends. The MPL and bundle width averaged over the regions indicated by the black rectangles are 84 ±7 kDa and 63 ±1nm, respectively. (C) Another septin bundle of uniform width and blunt ends, showing a lower MPL along its centerline compared to the edges. The contrast of the images is inverted. TMV rods in the images are indicated by arrows. (D) Schematic showing a possible septin arrangement that can explain the image shown in panel (C).

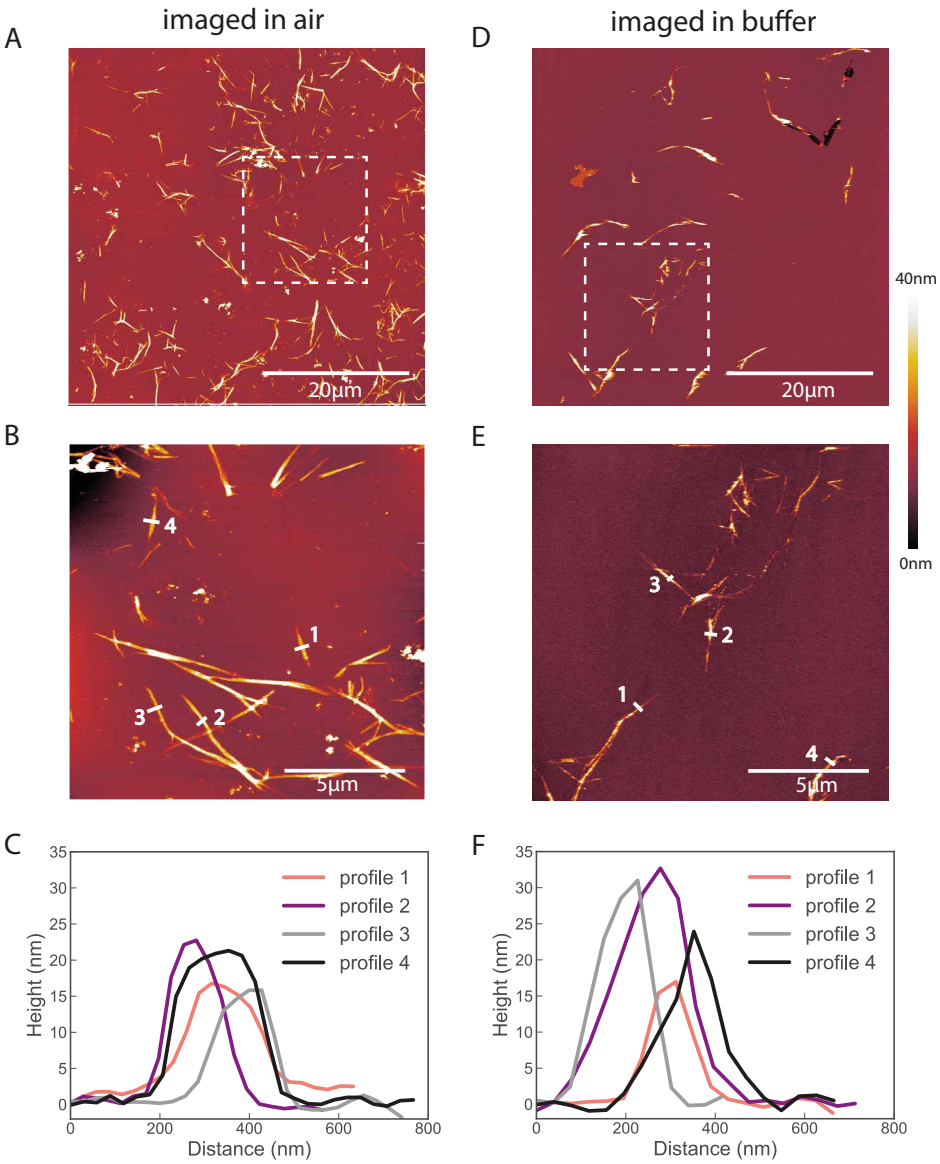

Figure 2.9: AFM height images of fly septin bundles on mica imaged in air and liquid (the color bar on the right displays the pixel heights). (A) Septin bundles prepolymerized at 500 nM for 30 min, imaged in air. (B) Zoomed-in region corresponding to the boxed region in (A). (C) Heights along the numbered line profiles shown in (B). Mean bundle height and width (FWHM) are 20 ±3 nm and 144 ±31 nm, respectively. (D) Septin bundles prepolymerized at 500 nM for 30 min, imaged in buffer. (E) Zoomed-in region corresponding to the boxed region in (D). (E) Heights along the numbered line profiles shown in (E). Mean bundle height and width are 27 ±6 nm and 97 ±19 nm, respectively.

2.4 Discussion

In this chapter, we reported a comparative analysis of the self-assembly behavior of recombinant fly septin hexamers and yeast septin octamers using fluorescence and electron microscopy. Fluorescence microscopy showed that yeast septins form thin, semiflexible filaments, whereas fly septins form thick bundles with tapered ends. FRAP analysis showed that the septin bundles were very stable, with negligible subunit exchange. This observation is consistent with surface plasmon resonance measurements of the stability of yeast septin filaments, which also showed negligible subunit exchange [140]. Using scanning transmission electron microscopy (STEM), we were able to quantify the molecular packing density of the septin filaments and bundles. Our STEM measurements for the first time provide quantitative evidence based on mass measurements that yeast septins form paired filaments, confirming previous conclusions based on transmission EM images [19, 78], fluorescence polarization microscopy [100] and fluorescence localization microscopy [84]. By contrast, we find that fly septins form bundles that are comprised of 6-20 hexamers per cross-section at 200 nM and up to hundreds of hexamers per cross-section at 500 nM.

A few studies have reported bundling also for yeast septin filaments [87]. However, our work suggests that fly septin hexamers have a much stronger tendency for lateral association compared to yeast septin octamers. A similar bundling tendency was reported in previous studies of recombinant fly septin hexamers [21, 53] as well as human septin hexamers [53], although the extent of lateral association was not quantified in those studies. It remains to be determined whether septin bundling has any physiological roles. A recent single-molecule imaging study of human osteosarcoma U2OS cells revealed a subset of septins associated with actin stress fibers that formed thick bundles comprised of 25 to 150 septin filaments [97]. Possibly the extended and rigid structure of these septin bundles contributes to their proposed role in templating actin stress fibers [15]. Another study showed that human septins in mitotic cells are normally not bundled, but that expression of non-SUMOylatable septin variants causes aberrant septin bundle formation and defects in cytokinesis [32].

It is unclear which domain of septins is responsible for the lateral association into bundles. Structurally, septins are comprised of three principal domains: an N-terminal domain containing a stretch of basic residues, a central GTP-binding domain, and C-terminal domains (see Chapter 1). The Pnut and Sep2 subunits of fly septin hexamers have long C-terminal extensions, whereas the Sep1 subunits have short C-terminal extensions. In the crystal structure of the human SEPT2/SEPT6/SEPT7 heterocomplex, no electron density was observed for the C-terminal domains, suggesting they are flexible [34]. Based on the sequence, it has been predicted that the C-terminal extensions adopt a coiled-coil conformation [86]. Circular dichroism spectroscopy of purified C-terminal domains (of human SEPT2, SEPT6, SEPT7 and SEPT4) confirmed this prediction and furthermore showed that SEPT6-

C and SEPT7-C are able to form both homo- and heterodimers [86, 141, 142]. EM images of septin oligomers from rat brain have indeed revealed thin strands projecting outward from the rod-shaped core [143], which are likely heterodimeric parallel coiled coils arising from the C-terminal domains of SEPT7 and SEPT6 [141]. Coiled-coil interactions contribute to the stability of septin complexes [86]. Moreover, EM images of yeast septin filaments strongly suggest that heterodimeric coiled-coils from adjacent filaments form four-helix bundles that mediate pairing of septin filaments [19].

It is possible that some fraction of the C-terminal extensions is not engaged in pairing and is available for lateral association. An alternative (or additional) driver of lateral association could be the GTP-binding globular domain. It has been speculated in the context of EM observations of yeast octamers forming extended filament sheets on lipid monolayers that the globular domains might be involved in lateral association of single filaments [62]. We are not aware of any direct evidence for this, but an interesting observation in this context is that magnesium ions and guanine nucleotides (GDP or GTP) were recently shown to promote bundling of yeast septin filaments [77]. To identify the molecular basis of septin bundling, it will be necessary to perform experiments on mutants, such as truncation mutants that lack the C-terminal extensions or point mutants where end-to-end assembly is impaired. Such structural studies of septin mutants have already proven very informative in the context of budding yeast septins [62]. Furthermore, it would be informative to perform molecular modelling of septins using the crystal structure of the hexamer core [34] and structural information on the coiled coils [86] as input.

Our work establishes STEM as a powerful technique to study in a quantitative manner how septin assembly is modulated by the molecular properties of the oligomers, especially when combined with a high throughput automated analysis of the images. Quantitative information on the MPL is important since it is a key determinant of the mechanical properties of septin filaments and bundles, which may influence functional properties such as membrane reshaping and curvature recognition [41, 144] and interactions with the actin and microtubule cytoskeleton [15]. It will for instance be interesting to compare septin complexes with different subunit compositions. The fruit fly has five septins divided in three homology subgroups, which form hexameric complexes. Here we focused on hexamers composed of Pnut, DSep1 and DSep2 [21, 53, 111, 114–116], but alternative hexamers have also been identified [115, 116, 145]. In humans there is a much larger number of septin genes (13) and protein isoforms (30), which form hexamers and octamers in different combinations [108]. It will be interesting to compare filaments polymerized from hexamers, octamers, or combinations, to test how the oligomer composition modulates filament formation [35, 36]. Likewise, STEM should be a useful tool to study the effects of GTP binding and hydrolysis [25], posttranslational modifications, and septin-binding proteins on septin self-assembly [26, 27, 45, 109].

Acknowledgements

I thank Aditya Iyer for introducing me to STEM imaging and mass mapping. I thank Cristina Martinez Torres for the joint STEM sessions and sharing experience in STEM imaging and data analysis. I thank Fouzia Bano (Leeds University) and Anders Aufderhorst-Roberts for help in imaging septin bundles by AFM. I thank Marjolein Kuit-Vinkenoog for protein purification. Furthermore, I acknowledge Henk Jan Boluijt for designing the teflon boxes for DDS glass treatment. For a critical reading of the manuscript, I thank Manos Mavrakis (Institut Fresnel, Marseille), Aurélie Bertin (Institut Curie, Paris), Ralf Richter (Leeds University), and Gerard Castro Linares.

2.5 Supplemental material

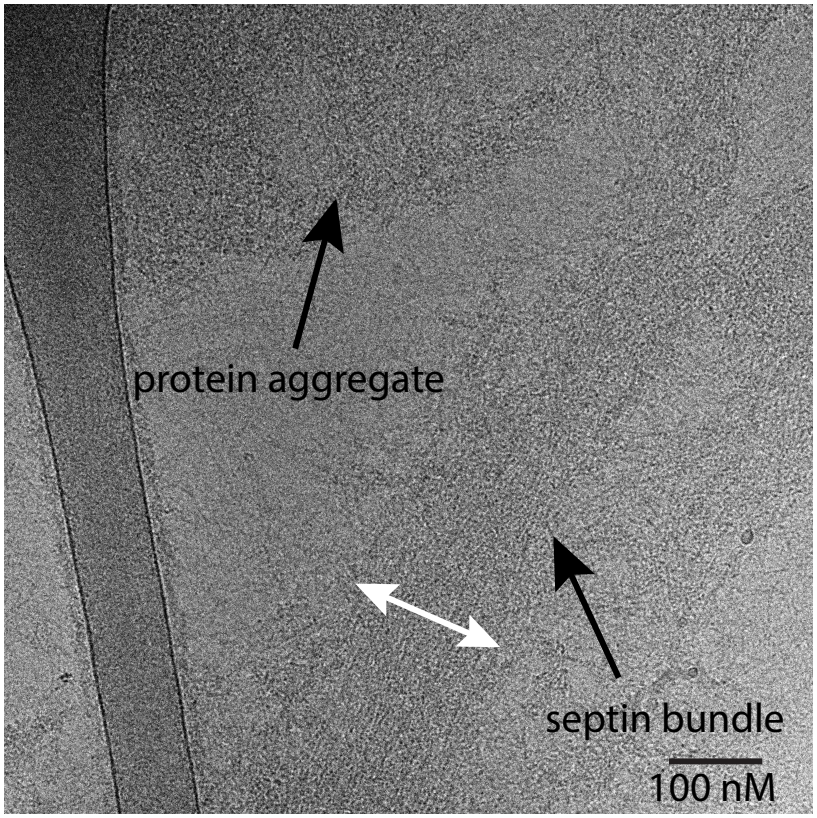

Figure S1: Bundle of human septin hexamers imaged by cryoEM. Human septin hexamers assembled at a concentration of 0.65 µM and deposited on a carbon grid. The image shows a septin bundle composed of aligned septin filaments and some protein aggregates (black arrows). The width of the bundle at the position indicated by the white arrow is 170 nm.

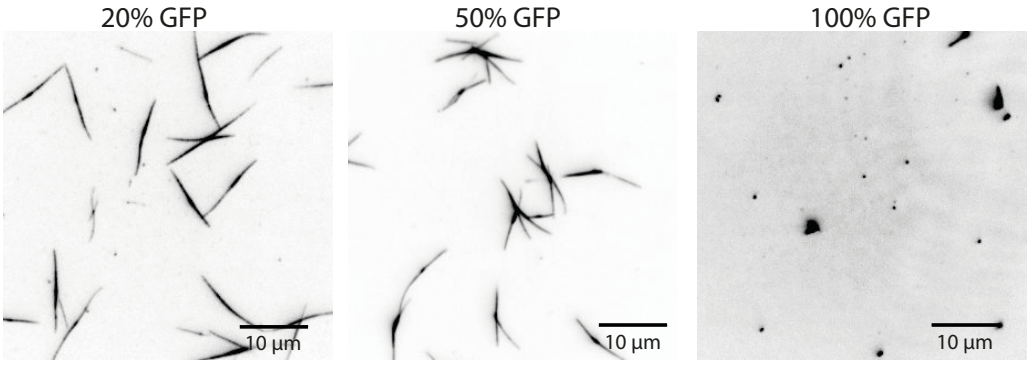

Figure S2: Incorporation of GFP-labeled septin hexamers beyond 20% influences fly septin bundle formation. Contrast-inverted TIRF images showing bundles composed of dark septin hexamers co-polymerized with GFP-labeled hexamers at different ratios. The septin bundles are long and rather straight for GFP-septin contents up to 20%, whereas they are short, bent, and aggregated in aster-like structures at 50%. At a GFP-septin content of 100%, septins form only clusters.

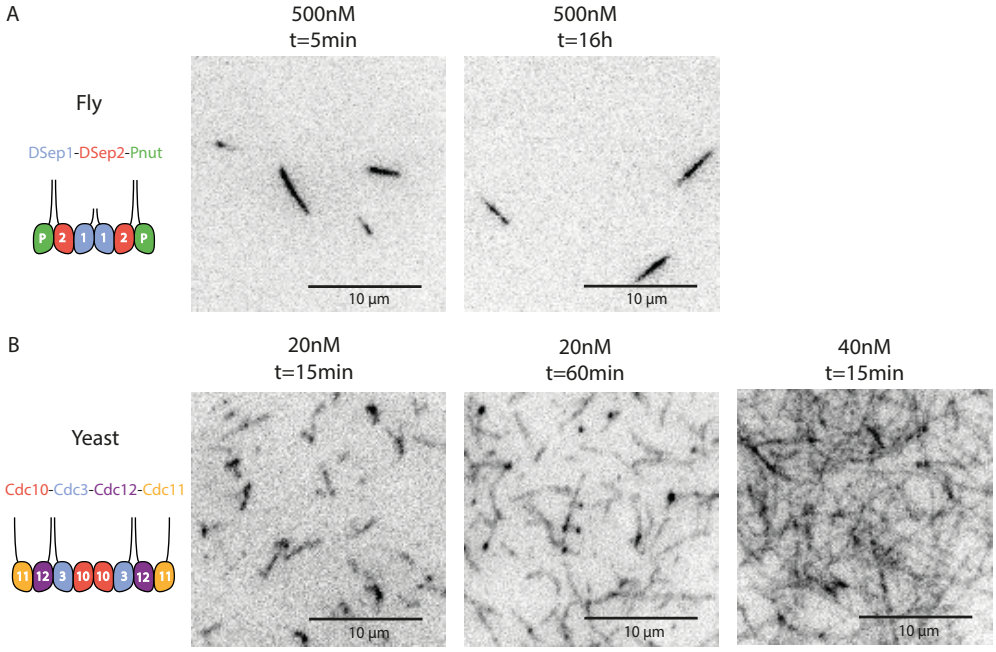

Figure S3: Comparison of the growth kinetics of fly septin hexamers and yeast septin octamers. (A) Fly septins at 500 nM polymerize instantaneously after rapid dilution (left) from high salt storage buffer (300 mM KCl) to low salt polymerization buffer (50 mM KCl) and they do not appreciably change in number density or length afterwards, even on a time scale of 16 hr (right). (B) Yeast septins (20 nM) initially form short filaments (left), which grow in length and density over a period of 60 min (middle). At 40 nM, yeast septins form denser coverages while still not bundling (right).

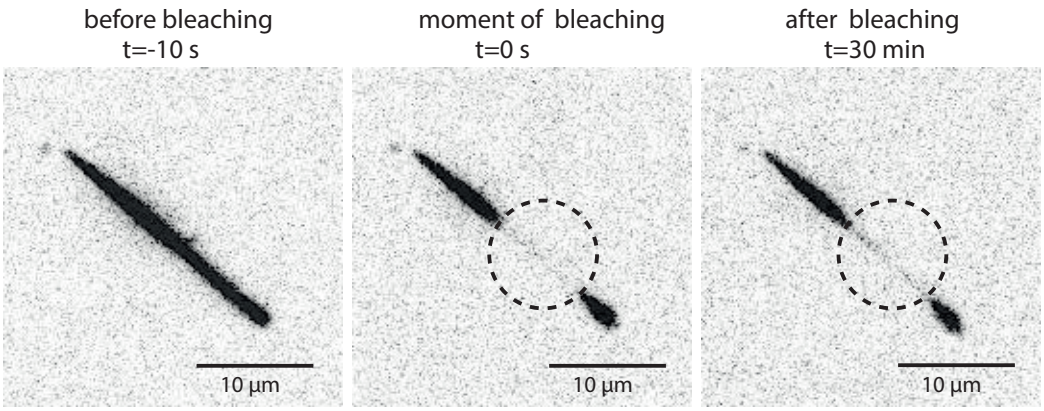

Figure S4: FRAP measurements reveal that fly septin bundles display negligible subunit exchange. Contrast-inverted TIRF images show a septin bundle before, during, and after bleaching. The circular region (dashed circle) that is photobleached by illumination with high-intensity laser light does not show any appreciable recovery of fluorescence intensity.

3

Membrane-templated assembly of septins

Septins are conserved proteins that have recently been recognized as an important component of the cytoskeleton for their ability to polymerize and interact with the plasma membrane and other cytoskeletal components. However, the architecture of septins in the proximity of the cell membrane and the role of septin-lipid interactions in septin polymerization remain poorly understood. Here we show by cell-free reconstitution and fluorescence microscopy that fly (Drosophila) septins form a dense protein layer on solid-supported model biomembranes, in contrast to the thick bundles formed in bulk solution (Chapter 2). Transmission electron microscopy imaging reveals that the septins form single and paired filaments on the membrane, which associate into tightly packed flat bundles. Similar structures are formed on bilayers containing phosphatidylserine (PS) or phoshatidylinositol(4,5)-bisphosphate (PIP_2) lipids, indicating that membrane binding is electrostatic in origin. Imaging of the membrane-bound septins in liquid using Atomic Force Microscopy reveals that septins already form filaments at a concentration of only 10 nM, which is an order of magnitude lower than the onset concentration for septin bundle formation in solution. The height of the septin layers is concentration-dependent, ranging from a single septin layer (~4 nm) at 10 nM to corrugated multilayers with heights varying between 4 and 17 nm at 60 nM. Our findings show that fly septins bind to anionic lipid membranes and that membrane binding catalyzes filament formation and prevents bundling, presumably because septin-membrane interactions compete with septin-septin interactions. These insights can help improve our understanding of the central role of septins in a wide range of cellular processes that involve the cell cortex, from cell migration to tissue morphogenesis.

3.1 Introduction

Septins are a family of cytoskeletal proteins that are conserved from fungi to humans [146]. They assemble into filamentous scaffolds that participate in diverse cellular processes taking place at the cell cortex, such as cytokinesis, cell-cell adhesion, exocytosis, macropinocytosis, and phagocytosis [64, 147–149]. Most of what we currently know about the molecular mechanisms by which septins participate in these processes comes from studies of the yeast cell *S. cerevisae*, where septins were first discovered [17]. Mitotic yeast cells express five septins that form hetero-octamers with a core of 3 subunits arranged as Cdc12-Cdc3-Cdc10-Cdc10-Cdc3-Cdc12 and terminal subunits provided either by Cdc11 or Shs1 [19, 76–78, 85]. The octamers form paired filaments that associate into bundles and networks [78, 80, 81, 150]. During budding, septins form a collar encircling the bud neck that acts as a scaffold to recruit proteins necessary for cell division and cell cycle progression[151–154] and that restricts lateral diffusion of integral membrane proteins [155–157].

Fluorescence correlation spectroscopy measurements showed that mitotic yeast septins are present as octamers in the cytosol and form filaments exclusively on the plasma membrane [61]. *In vitro* reconstitution studies showed that membrane-binding indeed strongly promotes septin polymerization because the membrane concentrates septins and facilitates diffusion-driven annealing [61, 62]. Also for meiotic septins, membrane binding strongly promotes filament formation [158]. Yeast septins are targeted to lipid membranes by the N-terminal polybasic domain of the Cdc10 subunit, which binds to the anionic phosphoinositide lipids PI, PI(4,5)P_2 and PIP_3 [61–63] but not to PI(4)P nor to the anionic lipid phosphatidylserine [62, 159]. Septins are curvature-sensitive and preferentially localize to regions with micron-scale curvature [40, 41, 77], which may be due to a putative amphipathic helix on the carboxy-terminus of Cdc12 [144].

Compared to yeast septins, animal septins have a much more variable cellular localization that changes with tissue type, developmental stage, and passage through the cell cycle [15, 16]. Similar to yeast septins, animal septins are frequently found at curved regions of the plasma membrane such as the base of dendritic spines and cilia, where they provide a diffusion barrier [160–162]. However, septins also associate with flat regions of the cell cortex, where they influence the rigidity and contractility of the actin-myosin cortex, both in single cells [47, 48, 56] and in tissues [49, 58, 93]. Cortical septins also play a key role in cytokinesis, where they are needed to stabilize the actomyosin ring [53], control membrane diffusion [163], and recruit proteins required for chromosome segregation and abscission [37, 69, 164]. However, it is still unclear whether the cortical septin pool associates directly with the plasma membrane or indirectly through association with cortical actin and microtubules [46, 92].

It is known from biochemical reconstitution studies that some mammalian septins are able to bind lipid membranes in the presence of various phosphoinositides (PIs) with no phosphorylation (PI), monophosphorylation (PI(3)P, PI(4)P, PI(5)P), di-

phosphorylatation ($PI(4,5P)_2$, $PI(3,4)P_2$), and tri-phosphorylation ($PI(3,4,5)P_3$) [40, 55, 64–66]. However, septins have also been shown to directly bind actin filaments [43, 53, 54] as well as actin-binding proteins present in the cell cortex such as anillin [94] and nonmuscle myosin-2 [71]. One study of membrane blebbing in amoeboid T-cells showed that septins are recruited to retracting blebs after actin polymerization, hence it was suggested that actin-binding may be necessary for cortical recruitment [56]. Furthermore, electron microscopy imaging of immunostained cells revealed localization of cortical septins with cortical actin in tissue culture cells [91, 92]. However, the high density of the actin cortex in animal cells has made it impossible to unambiguously distinguish actin and septin filaments in electron micrographs. It therefore remains an open question whether cortical septins interact with the plasma membrane and even whether they actually form filaments. Fluorescence microscopy has shown the presence of cortical septin puncta, fibrous strands, or rings, but has lacked the resolution to resolve the precise nature of these structures [48, 49, 56, 93]. Septin-deficient cells exhibit a markedly reduced cortical rigidity, but it is unclear whether these effects imply a loss of membrane-bound septin filaments or a loss of septin-mediated actin stabilization [47, 48, 56, 58]. A further complication is that microtubules have also been found to interact with cortical septins. In nonadhered cells, cortical microtubules were shown to be important for stabilizing septin rings at the cell cortex [98].

To resolve the functions of septins at the cell cortex of animal cells, it is necessary to understand the innate ability of septins to assemble alone and in association with the membrane. Several reconstitution studies have been reported for native and recombinant septins from various animal species, but nearly all of these studies considered septin assembly in solution. Frog (*Xenopus laevis*) septins were found to form paired filaments similar to yeast septins [110], while recombinant nematode (*C. Elegans*) septins [20] and native and recombinant fly (*Drosophila melanogaster*) septins [21, 53] were observed to form bundles that resemble the bundles formed by yeast septins at elevated concentrations [19, 76, 77, 87]. In Chapter 2 we confirmed that fly septins form rigid bundles in solution. Interestingly, one study of recombinant septin hexamers (composed of murine Sept2 and human Sept6 and Sept7) purified from insect cells [94] showed that septins can form rings and spirals that are reminiscent of structures formed by Shs1-capped yeast septin octamers [165]. To the best of our knowledge, there are only two reports until now of the structure of animal septins on lipid membranes [55, 66]. In this work, native porcine septins and recombinant human septin hexamers (composed of Sept2, Sept6 and Sept7) were incubated with giant liposomes, which resulted in the formation of thin (0.4 μm) membrane tubes. Electron microscopy showed that both the liposome body and the membrane tubes were covered by a dense array of septin paired filaments and bundles thereof.

In this chapter we investigate the role of membrane-binding in septin assembly by reconstituting recombinant septins on supported lipid bilayers containing controlled fractions of negatively charged phospholipids. We use septins from the fruit fly

(*Drosophila*), which is a genetically tractable model system that expresses only five septins that assemble in hexamers. We specifically focus on hexamers comprised of Pnut, Sep2, and Sep1, which have been previously characterized *in vivo* [53, 114–116] and *in vitro* [21, 53, 111]. We studied the septins on model biomembranes composed of phosphatidylcholine (PC) lipids mixed with various concentrations of two different biologically relevant anionic lipids. We selected phosphatidylserine (PS), because this is the most abundant anionic lipid in the inner leaflet of the plasma membrane [166], and the signaling lipid phosphatidylinositol 4,5-bisphosphate (hereafter referred to as PIP_2), as it was shown in biochemical reconstitution studies to interact specifically with yeast septins [62, 159] and some mammalian septins [65]. We show by fluorescence imaging that fly septin hexamers have a high affinity for negatively charged membranes and form dense membrane-associated meshworks. High-resolution imaging by electron microscopy and by atomic force microscopy reveals that these septin meshworks are comprised of single and paired filaments, which laterally associate into ribbon-shaped bundles that form tightly packed ordered domains. Our findings establish that fly septins have the innate ability to form stable filamentous meshworks on lipid membranes, which may contribute to the ability of septins to regulate the cortical rigidity and tension of cells.

3.2 Materials and Methods

3.2.1 Septin preparation

Recombinant *Drosophila* septin hexamers (composed of His6-tagged DSep1, DSep2 and Strep-tagged Peanut), GFP-labeled fly septin complexes for fluorescence microscopy (containing DSep2 subunits with mGFP fused to its N-terminus) were expressed and purified from bacteria in-house, as detailed in Chapter 2. Human hexamers composed of His_6-hSep2, hSep6 and hSep7-Strep subunits [53] were purified by Aurélie Bertin (Institut Curie, Paris) according to the same protocol. The molecular weight and purity of the septin complexes were checked on SDS-PAGE gels and the length of the complexes (as a readout of the stability of the hexameric arrangement) was checked by negative stain transmission electron microscopy.

3.2.2 Fluorescence microscopy of septins on supported lipid bilayers

Sample preparation

We used four lipid species, all purchased either in powder form or dissolved in chloroform from Avanti Polar Lipids (Birmingham, AL): DOPC (L-α-phosphatidylcholine), DOPS (1,2-dioleoyl-*sn*-glycero-3-phospho-L-serine), PIP_2 (1,2-dioleoyl- *sn*-glycero-3-phospho-(1'-myo-inositol-4',5'-bisphosphate) (ammonium salt) and fluorescently labeled rhodamine-DOPE (1,2-dioleoyl-sn-

glycer-3-phosphoethanolamine-N-(lissamine rhodamine B sulfonyl). DOPC, DOPC and rhodamine-DOPE lipids were stored at a concentration of 10-25 mg/ml in chloroform. PIP_2 was ordered in powder and dissolved at a concentration of 0.5 mg/ml in a mixture of chloroform:methanol:water 20:9:1 vol-%, as suggested by the manufacturer.

Small unilamellar vesicles (SUVs) were prepared by drying mixtures of DOPC/DOPS/rhodamine-DOPE (79.7:20.0:0.3 molar ratio), DOPC/PIP_2/rhodamine-DOPE (94.7:5.0:0.3), or DOPC/DOPS/PIP_2/rhodamine-DOPE (74.3:20.0:5.0:0.3) in glass vials. DOPC/DOPS lipid mixtures were resuspended in an imidazole buffer of pH 7.4 (20 mM Imidazole-HCl, 50 mM KCl, and 2mM $MgCl_2$) to reach a total lipid concentration of 0.5µM. PIP_2-containing lipid mixtures were resuspended to a total lipid concentration of 0.25-0.5µM in an acidic citrate buffer of pH 4.8 (50 mM citrate, composed of equal molarity trisodium citrate and citric acid mixed in a 2:3 volume ratio to obtain pH 4.8), containing 50 mM KCl, and 0.1 mM ethylenediaminetetraacetic acid. At this acidic pH, the net charge on the head group of PIP_2 is reduced (from −4 to −3), which promotes the formation of homogeneous and fluid bilayers [167]. SUVs were obtained by sonication with a tapered microtip (Branson, USA, 3 mm diameter) for 30 min in pulsed mode using settings of 30 s on/30 s off at 10% amplitude. Vesicles were stored at room temperature for a maximum of 30 days in case of DOPC/DOPS vesicles and 7 days in case of PIP_2-containing vesicles.

To prepare supported lipid bilayer (SLB), SUVs were flushed into cleaned glass channels (see Chapter 2), leading to their rupture and spreading within 10-15 min. The SLBs were washed with 5 channel volumes of septin polymerization buffer to remove remnant SUVs. Recombinant fly septin hexamers were diluted from high salt storage buffer to a final concentration between 10 nM and 1 µM in polymerization buffer (20 mM imidazole pH 7.4, 1 mM dithiothreitol (DTT), 0.1 mM MgATP, 50 mM KCl and 2 mM $MgCl_2$) complemented with 1 mM trolox to suppress blinking and an oxygen scavenging system of 2 mM protocatechuic acid and 0.1 µM protocatechuate 3,4-dioxygenase to minimize photobleaching [132]. The septin mix was directly flushed onto the lipid bilayers. The septins were fluorescently labeled by co-polymerizing 90 mole% unlabeled septin hexamers with 10 mole% of GFP-septin hexamers having mGFP fused to the N-terminus of the DSep2 subunits.

Fluorescence microscopy, FRAP, and data analysis

Total Internal Reflection Fluorescence (TIRF) imaging was performed as described in Chapter 2. For experiments where the intensity of labeled septin was compared among different preparation conditions, the TIRF angle and acquisition settings were kept the same. Images were processed and analyzed with Fiji software [134] (contrast enhancement, look-up table inversion, integrated intensity calculation).

Confocal imaging was performed on a NikonA1 microscope equipped with a

100x oil immersion objective and a Perfect Focus system. Septins and lipid bilayers were imaged with a 100-mW Argon laser (Coherent, CA, USA) using excitation wavelengths of 488 nm and 561 nm, respectively. The turnover dynamics of septin structures was measured by Fluorescence Recovery After Photobleaching (FRAP) experiments, where we bleached a circular region of 10 µm diametre in 1 second with the laser power set to 70% and afterwards monitored the time-dependent fluorescent signal in the bleached region and a reference region of the same size for a period of 7 minutes.

3.2.3 Transmission electron microscopy of septins on lipid monolayers

Samples for transmission electron microscopy (TEM) were prepared by incubating septin hexamers with lipid monolayers formed at an air-buffer interface. Teflon wells were filled with 50 µL of a solution of 65 nM (fly) or 70 nM (human) septin hexamers in a 50 mM Tris-HCl (pH 8) buffer with 50 mM KCl. To each well, a small magnetic stirrer bar was added. A drop of lipid mix at a total concentration of 0.5 g/L in chloroform was deposited on the surface of the solution in each well in order to form a lipid monolayer. The Teflon block was kept in a humid chamber overnight and at 4 °C while stirring. Lipid monolayers with adsorbed septins were collected by briefly placing hydrophobic grids (Electron Microscopy Sciences, Hatfield, PA, USA) on the surface of the solutions with the carbon-coated side facing the solution. Grids with the collected monolayers facing up were stained with 2% uranyl formate (Nanoprobes) in water by depositing 4 µL on the grid and simultaneously blotting the excess solution. Samples were imaged using a Philips CM12 (120 kV) electron microscope at Imagopole (Institut Pasteur, France).

3.2.4 Cryo-electron microscopy of septins on lipid vesicles

Samples for cryoEM were prepared by incubating septin hexamers with large unilamellar vesicles (LUVs). Lipid mixtures at a total lipid concentent of 50 µg/sample in glass vials at the desired lipid ratios were dried with argon and left in vacuum for 2 hours to fully evaporate the chloroform. LUVs were formed by hydrating the lipids in high salt buffer (20 mM imidazole pH 7.4, 1 mM DTT, 300 mM KCl and 2 mM $MgCl_2$). The vesicles were next incubated for 30 min with 5 µg of septins at a concentration of 1.6 µM (0.5 g/L) in high salt septin storage buffer, corresponding to a lipid-to-protein weight ratio of 10:1. In the meantime, lacey carbon-coated grids were plasma treated (Electron Microscopy Science) for 30 min to hydrophilize the surface and remove any impurities. Next, the vesicles were diluted fivefold in septin polymerization buffer (20 mM imidazole pH 7.4, 1 mM DTT, 50 mM KCl and 2 mM $MgCl_2$) to a final concentration of 0.3 µM (0.1 g/L) and applied to the grid straight after plasma treatment. Gold particles with a diameter of 10 nm (EMS) were added to each sample to align images for 3D tomography

reconstruction (images not shown). Excess liquid was blotted and the samples were vitrified in liquid ethane using an automatic plunge freezer (EM PG, Leica). Samples were imaged using a FEI Tecnai G2 microscope equipped with a LaB6 filament and a CMOS camera F416 (TVIPS) operated at an acceleration voltage of 200 kV and a magnification of 50000 ×.

3.2.5 Atomic force microscopy of septins on supported lipid bilayers

Sample preparation

Mixtures of DOPC and DOPS lipids in an 80:20 molar ratio were dried in glass vials using an air stream and resuspended in filtered and degassed vesicle buffer (20 mM imidazole pH 7.4, 50 mM KCl, and 2 mM $MgCl_2$) to reach a total lipid concentration of 2 mg/mL. Small unilamellar vesicles (SUVs) were obtained by exposing the suspended lipids to 5 freeze/thaw cycles followed by sonication with a microtip (FisherBrand, 2 mm diameter) for 30 min in pulsed mode (1 s on/1 s off) at 30% amplitude with ice cooling. Next, vesicles were centrifuged (15 min at 15000 g) to remove any titanium particles that might be present in the solution due to wear of the sonicator tip. Before use, vesicles were diluted to 50 µg/mL in buffer of increased salt concentration (20 mM imidazole pH 7.4, 150 mM KCl, and 2 mM $MgCl_2$) to facilitate SUV rupture and spreading [168]. We used this more rigorous vesicle preparation protocol compared to the protocol used for TIRF imaging to ensure optimal quality lipid bilayers for high resolution imaging.

Silicon wafers with a thickness of 500-550 µm (Prime Silicon, Les Ulis, France) were cut into squares of 9×9 mm^2, rinsed with absolute ethanol, blow-dried with N_2, and treated with UV/ozone (Bioforce Nanoscience, Ames, IA) for 30 min. This pretreatment removes organic contaminations and renders the surface hydrophilic. Each substrate was glued on a metal disc (15 mm diameter from Agar Scientific, Ltd) using two components glue (Picodent Twinsil, WipperfÃ¼rth, Germany). The metal disc was covered with hydrophobic Fluorinated Ethylene Propylene (FEP) film protector (Bytac surface protection laminate, Sigma) to avoid contamination of the sample by solvent wetting the metal disc and glue. When the glue was set (~ 10 min), we deposited 100 µL of 100 µg/mL of vesicle solution diluted in septin polymerization buffer with an increased KCl concentration (20 mM imidazole pH 7.4, pH 7.4, 1 mM DTT, 150 mM KCl and 2 mM $MgCl_2$) on the hydrophilic surface of the silicon wafer. After 30 min incubation, excess vesicles were washed off by replacing the liquid with 1 mL of septin polymerization buffer (20 mM imidazole pH 7.4, 1 mM DTT, 50 mM KCl and 2 mM $MgCl_2$) using a pipette. We left 100 µL buffer on the wafer surface after washing the lipid bilayers to keep them hydrated. We than added 50 µL of septin solution to obtain the desired final concentration (either 12, 24, or 60 nM). After 15 min incubation at lab temperature (19°C), unbound protein was washed off with 1 mL of septin polymerization buffer. Unless mentioned otherwise, bound septins were fixed with 1 wt-% glutaraldehyde (GTA)

in septin polymerization buffer. Samples were incubated in the GTA-containing buffer for 1 min and then washed with polymerization buffer. We found that GTA fixation prevented septin disruption by the AFM tip, while it did not noticeably influence the morphology of the samples (see Fig. S2).

AFM imaging and data analysis

AFM images were acquired with a Nanoscope Multimode 8 AFM (Bruker, CA, USA) on samples immersed in buffer (20 mM imidazole pH 7.4, 50 mM KCl, 2 mM $MgCl_2$) at the AFM lab temperature (23°C). Images of various lateral dimensions (1 to 20 µm) at a resolution of 512 x 512 pixels and a scan rate of 0.8 Hz were recorded with sharp silicon cantilevers (ScanAsyst-Fluid+; Bruker) with a nominal spring constant of 0.35 N/m and sharp pyramidally shaped tips (referred to as Triangular tips by the manufacturer) with a nominal radius of 2 nm. Images were recorded in Peak Force Tapping mode with a typical driving frequency of 2 kHz and tapping amplitude of 50 nm.

Images were second-order flattened using open source software Gwyddion [137] to account for sample tilt, and were further analyzed using a customized analysis code written in Python. Septin filament heights were determined in two ways. First, we obtained height profiles along lines drawn over selected septin bundles and obtained the height of the bundles after subtracting the background (membrane) height taken from the same region. Second, we constructed histograms of the pixel heights for each image (or cropped region of an image), which were normalized so that the area under the histogram summed to 1. For samples with a sparse coverage by septin filaments (observed at septin concentrations of 12 and 24 nM), we observed two peaks that could be fitted to a double Gaussian distribution. We assumed that the first peak corresponds to membrane surface areas devoid of septins while the other peak corresponds to septin-covered areas. Therefore, we defined the difference in the mean height of these two peaks as the mean height of the septin filaments and the relative area under the second peak as the areal fraction covered by septins. For samples with a dense septin coverage (observed at 60 nM), where we could not clearly distinguish the bare membrane surface, we discriminated septins from membrane areas devoid of septins by computing a mean membrane peak width across the 12 nM and 24 nM data sets, i.e. for the data where we observed a distinct membrane peak. We then fitted a Gaussian with the peak width fixed to this mean value to the lower height end of the data for the 60 nM data sets and summated the rest towards estimating the surface area covered by septin filaments.

3.3 Results

3.3.1 Fluorescence imaging of septins on supported lipid bilayers

To investigate how fly septin binding to lipid membranes depends on lipid composition, we deposited fly septin hexamers on glass-supported lipid bilayers (SLBs) with different lipid compositions. When septins at a concentration of 1 μM were incubated on a neutral bilayer composed of only phosphatidylcholine (PC) lipids, they formed thick bundles with tapered ends (Fig. 3.1A). The bundles could be visualized only when they were pushed to the surface with a crowding agent (0.1% methylcellulose) and they were mobile. Both observations indicate that septins do not interact with DOPC membranes. This conclusion is confirmed by the observation that the bundles had a similar morphology as the thick bundles with tapered ends formed on inert glass passivated with dichlorodimethylsilane (DDS) or in solution (see Fig. 2.4 in Chapter 2).

By contrast, septins deposited on DOPC membranes doped with 5 mole% of the anionic lipid phosphatidylserine (DOPS) formed filamentous structures on the membrane in the absence of methylcellulose and these were immobile, suggesting that septins do interact with negatively charged membranes (Fig. 3.1B). Interestingly, the membrane-bound septins formed thinner and more elongated bundles compared to the septin bundles formed in solution. This observation suggests that septin-membrane interactions prevail over the lateral septin-septin interactions that drive bundling in solution. The membrane-bound bundles exhibited longitudinal growth on both ends (see Fig. S1 in the supporting information), consistent with the symmetric structure of septin hexamers. On membranes containing 5 mole% of the anionic lipid PIP_2, septins also adsorbed, but they formed a film that covered the entire bilayer and that was so dense that the internal structure could not be resolved by light microscopy (Fig. 3.1C).

To test the stability of the septin films, we performed fluorescence recovery after photobleaching (FRAP) experiments. When we photobleached a circular region in the septin film, we observed no recovery whatsoever during a period of 7 minutes (Fig. 3.2). This observation suggests that the septins are stably anchored to the membrane and that there is negligible exchange of septin subunits. Nevertheless, we did not observe any significant influence of septin binding on the diffusivity of phosphatidylethanolamine (PE) tracer lipids when we compared FRAP measurements on bare membranes versus membranes with bound septins (Fig. 3.2 in the Supporting Information). When we photobleached the lipids, we observed complete fluorescence recovery with a diffusion constant of ~ 1.2 cm^2/s.

Given the different appearance of septins on membranes containing 5% PS versus 5% PIP_2, we wondered whether septin binding is governed by specific recognition of PIP_2 or rather by the amount of negative charge displayed on the membrane. On the one hand, a preference for lipid species is possible given earlier evidence that yeast

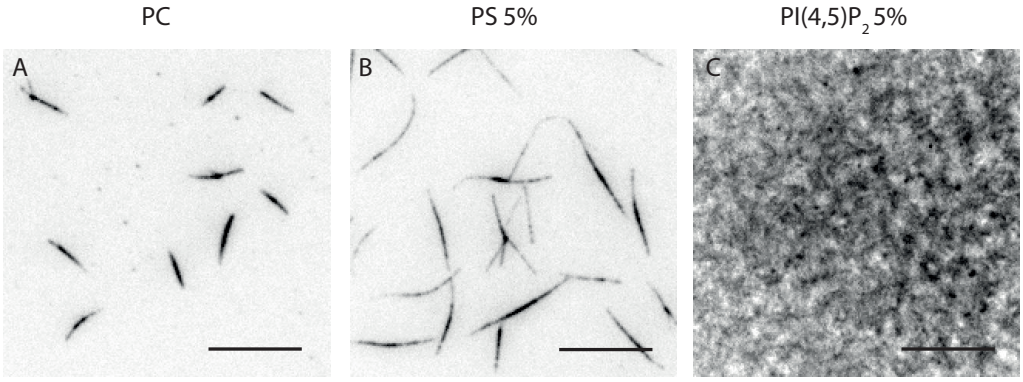

Figure 3.1: TIRF images reveal that fly septin hexamers (1 µM) bind to negatively charged glass-supported lipid bilayers (SLBs) and that membrane binding affects septin self-assembly. (A) On neutral bilayers composed only of DOPC lipids, septins form thick and rigid bundles that are mobile, indicating that septins do not interact with the membrane. Methylcellulose (0.1%) was required to push the septin bundles close enough to the membrane so they were visible in the shallow (~100 nm) TIRF field. (B) On DOPC bilayers doped with 5 mole % PS, septins localize to the membrane in the absence of methylcellulose, and they form long, immobile bundles that grow on both ends (see Fig. S1). (C) On DOPC bilayers doped with 5 mole % PIP $_2$, septins also adsorbed to the membrane in the absence of methylcellulose, forming a dense layer whose internal structure is too fine to resolve by light microscopy. Note that the image contrast is inverted, so dark regions represent septins and white regions are membrane areas devoid of septins. Scale bar: 10 µm.

septins selectively bind to PIP_2 whereas they do not bind to PS [62, 159]. On the other hand, it could be that septins simply have a larger affinity for PIP_2 compared to PS due to the difference in charge on the head group of these two lipids. The head group of PIP_2 has a net charge of -4 at neutral pH, while the head group of PS carries a charge of only -1 [169–172]. We systematically screened the effect of surface charge on septin assembly by incubating septins with DOPC bilayers doped with different mole fractions of PS (Fig. 3.3A). When we increased the PS mole fraction from 5 to 10%, septins formed thinner bundles and covered a larger fractional surface area. When we increased the PS mole fraction further to 20%, we observed a dense septin layer that resembled the septin layers formed on bilayers containing 5 mole% PIP_2.

When septins were incubated with DOPC bilayers doped with different mole fractions of PIP_2 ranging from 1 to 8%, we again observed a gradual transformation from thin septin bundles to dense septin meshworks whose structure could not be resolved (Fig. 3.3C). The comparable evolution from sparse bundles to dense meshworks on bilayers containing increasing amounts of PS or PIP_2 suggests that the membrane-binding affinity of fly septins is governed by the net surface charge of the membrane and not by any specific affinity for PIP_2.

To quantify the amounts of adsorbed septin as a function of lipid composition,

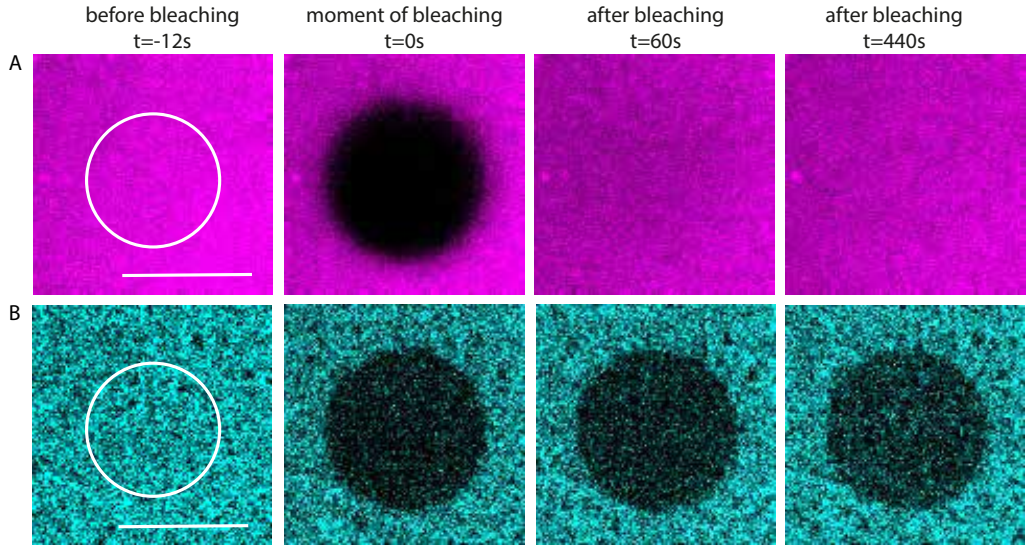

Figure 3.2: Membrane-adhered septin layers are immobile and stable over time. A solution of 500 nM fly septin hexamers tagged with 10 mole% mGFP-labeled hexamers was incubated with glass-supported lipid bilayers containing DOPC, 20% PS, and a small fraction of fluorescently labeled lipids (0.3% rhodamine-PE). After photobleaching a circular region of interest (indicated by the white circle) at time $t = 0$, the lipid bilayer fully recovered, as indicated by the reappearance of the rhodamine-PE fluorescence in the bleached region (A), whereas the septin meshwork did not recover on the time scale of the experiment ($\sim$ 7min) (B). Scale bar: 10 µm.

we extracted the integrated septin intensity from images acquired with constant TIRF angle and illumination settings. As shown in Fig. 3.3B, the septin signal increased almost linearly with PS content, showing a 4-fold enhancement on raising the PS content from 5 to 20 mole%. Furthermore, the septin signal did not increase during a 4 hr incubation time, even though the channel was not washed with buffer. This observation suggests that septins bind strongly and rapidly to the membrane provided that sufficient negative charge is exposed. In all cases, filamentous structures were already present as soon as we could start imaging ($\sim$ 3 min after septin in-flush) and the structures did not appear to change in number or thickness over time (compare first and second row of Fig. 3.3).

Our data show that fly septins interact with both PIP_2 and PS lipids and, for the same net surface charge, the same type of septin structures can be obtained on lipid membranes containing either lipid. This observation is in strong contrast with observations for Cdc11-capped yeast septin octamers, which were shown to be highly selective for $PI(4,5)P_2$, showing negligible binding to bilayers containing up to 20% PS [62, 159]. Apparently, the strongly specific $PI(4,5)P_2$ binding of Cdc11-capped yeast septin octamers is not conserved in fly septin hexamers.

To test the dependence of septin adsorption on bulk septin concentration, we

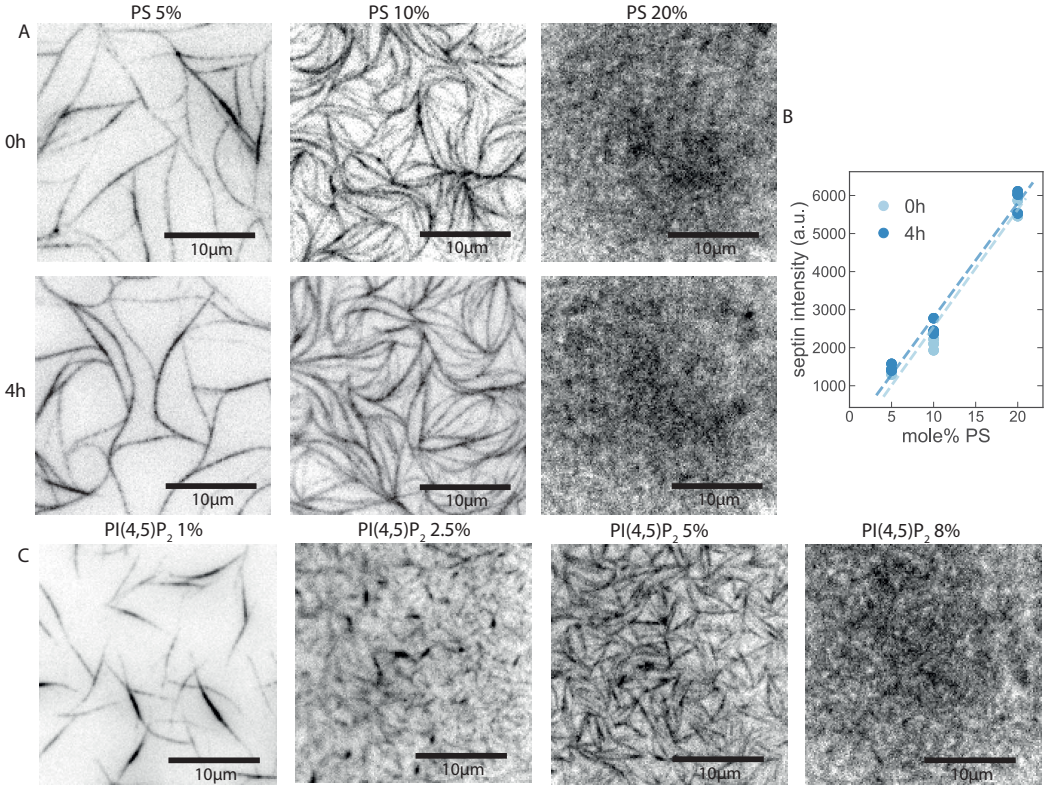

Figure 3.3: TIRF imaging shows that septin assembly on lipid bilayers is governed by the content of negatively charged lipids. (A) TIRF images obtained after ~ 3 min (top row) and after 4 h (bottom row) from the moment of septin deposition on DOPC bilayers doped with 5, 10 or 20 mole% DOPS. The larger the DOPS content, the less bundled and the more dense and grainy the septin layer appears. (B) Corresponding integrated septin intensities, showing a linear increase with PS content (lines are fits). $N = 3$ per condition. (C) Septins incubated on DOPC bilayers containing 1, 2.5, 5, or 8 mole% PIP_2, observed ~ 3 min after protein deposition. Again, septins form thinner filaments and more dense and uniform layers as the fraction of PIP_2 lipids is raised. Note that in this case we cannot plot the septin intensity as a function of PIP_2 content because the images were taken on different days. In all cases, the septin solution concentration was 500 nM.

incubated bilayers containing 20 mole% PS with solutions of septin hexamers at concentrations ranging between 10 and 500 nM. As shown in Fig. 3.4A, we observe uniform septin layers with a texture that cannot be resolved at the resolution of the TIRF microscope over this entire concentration range. We note that septins already form membrane-bound layers at concentrations below the onset of bundle formation in bulk solution, which occurs between 100 - 200 nM (see Chapter 2), suggesting that membrane association catalyzes polymerization. However, at the diffraction-limited resolution provided by TIRF microscopy we cannot distinguish whether these layers truly are filamentous. The septin fluorescence intensity increases roughly linearly

with septin concentration (Fig. 3.4B) even in the concentration range (200-500 nM) where septins in the absence of a membrane form bundles. It should be noted that by confocal microscopy we observe the presence of septin bundles in the solution above the bilayer for septin concentrations above 200 nM.

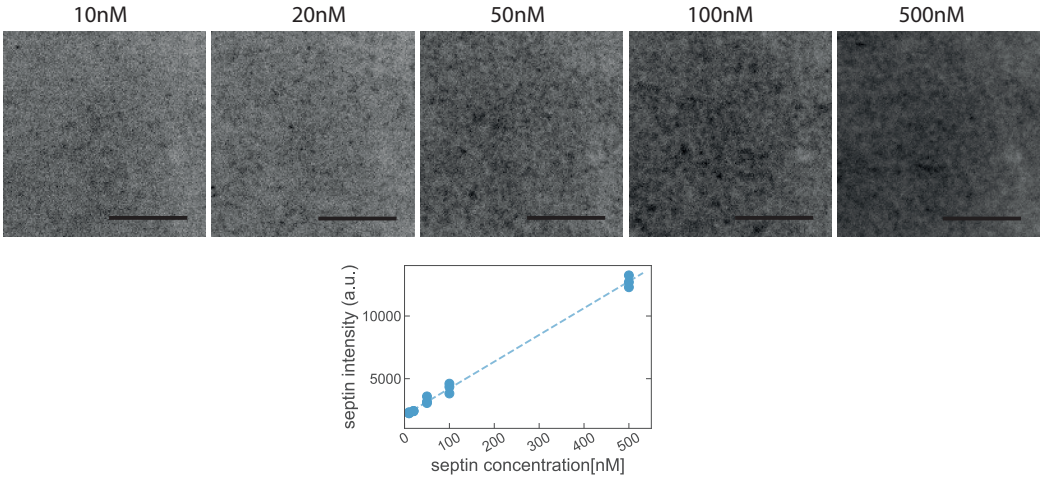

Figure 3.4: Septins bind to negatively charged supported lipid bilayers in a concentration-dependent manner. (A) Septins at concentrations ranging from 10 to 500 nM form dense layers with little discernible structure observable by TIRF microscopy on DOPC lipid bilayers containing 20% DOPS. Scale bars: 10 µm. (B) The amount of adsorbed septins as measured from the integrated intensity of the images normalized by the image size (16 bit images, [AU/px]) increases roughly linearly with the solution concentration of septins. The solid line shows a linear fit to the data; the non-zero intercept reflects background fluorescence. Data is collected from 15 images and 3 independent samples.

3.3.2 Electron microscopy imaging of septins on lipid monolayers

The TIRF images suggest that membrane binding causes septins to form dense layers of thin filaments instead of the thick bundles formed in solution. However, we are unable to observe the precise architecture of the membrane-bound septin layers due to limitations posed by the optical diffraction limit. To circumvent this, we therefore turned to transmission electron microscopy. We incubated septins with lipid monolayers, deposited these on EM grids, and negatively stained the protein with 2% uranyl formate, following a protocol previously established in the context of yeast septins [62]. We used the same lipid compositions for the monolayers as for the TIRF assays, basing the monolayers on DOPC lipids mixed with either 20 mole% PS, 5 mole% PIP_2, or a combination of both that mimics the co-existence of both lipids in the plasma membrane of cells [173, 174].

As shown in Fig. 3.5, we observe densely packed arrays of thin filaments in all three cases, which is qualitatively consistent with the dense meshworks observed by TIRF microscopy. Close inspection of the EM micrographs (see insets) reveals paired filaments with an approximate center-to-center spacing of ~ 6.5 nm. Given a width of 4 nm for septin hexamers [34], the spacing between the two filaments forming a pair is only 2.5 nm. This spacing is much smaller than the ~ 14 nm length of the long coiled-coil carboxy-terminal extensions that emanate from the Pnut and Dsep2 subunits, which are expected to mediate pairing [62]. This implies that the coiled coils must either stick out or be collapsed in-plane. We occasionally observed that adjacent paired filaments merged, either in a parallel fashion to form flat bundles (white arrow in Fig. 3.5A) or under a small angle (red arrowheads). On monolayers containing 20% PS and 5% PIP_2, we could observe clear examples of paired filaments that were bridged by thin (presumably single) filaments having a length of ca. 24 nm and with an axial spacing of 24 nm (Fig. 3.5C blue arrows). These bridges were either perpendicular to the filaments they bridged (white lines) or under an angle (red line). We note that a 24 nm length corresponds to the length of a single septin hexamer [34].

To test whether septin organisation is conserved among species, we repeated these experiments with human septin hexamers. As shown in Fig. 3.5D, we again observed dense arrays of paired filaments. Again the filaments were tightly paired, and they were connected by single filaments that formed orthogonal or diagonal bridges. These observations suggest that membrane-mediated septin organization is conserved between fly and human septins.

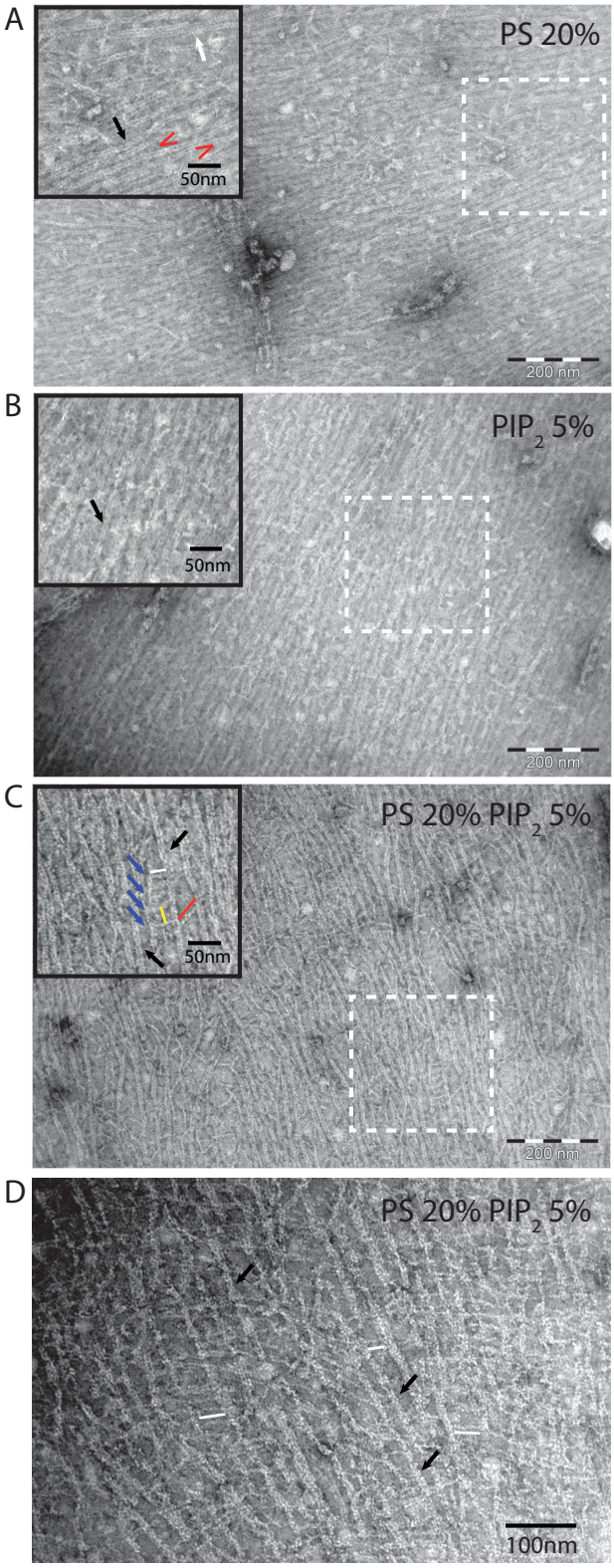
A
PS 20%
50nm
200 nm
B
PIP2 5%
50nm
200 nm
C
PS 20% PIP2 5%
50nm
200 nm
D
PS 20% PIP2 5%
100nm

Figure 3.5 *(preceding page)*: Negatively stained EM images show that fly and human septin hexamers form dense arrays of paired filaments on anionic lipid monolayers. Insets show zoom-ins of the regions indicated by the white dashed squares. Septin hexamers were incubated overnight at a concentration of 65 nM with lipid monolayers composed of DOPC doped with PS and/or PIP_2. (A) Septins on a monolayer containing 20% PS. The black arrow indicates a paired filament, the white arrow indicates two paired filaments joining together into a flat bundle composed of 4 filaments, and the red arrowheads indicate two examples of paired septin filaments that join under an angle. (B) Septins on a monolayer containing 5% PIP_2. The black arrow indicates an example of a paired filament. (C) Septins on a monolayer containing 20% PS and 5% PIP_2. The black arrows indicate examples of paired filaments. In the middle we see an example of a pair of septin filaments separated by a distance of ~24 nm at the narrowest point (white line) and bridged by multiple orthogonal filaments that are themselves also spaced by ~24 nm (yellow line). Red line shows a longer cross-bridging filament (43 nm in length), which bridges two adjacent paired filaments under an angle. (D) Human septin hexamers at 70 nM on a monolayer containing 20% PS and 5% PIP_2 showing paired filaments (black arrows) connected by many crossbridging filaments (white lines).

3.3.3 Electron microscopy imaging of septins on lipid vesicles

The TEM assay has the disadvantage that sample preparation requires drying and negative staining. To validate that these treatments did not affect the supramolecular organisation of the septins, we also performed cryo-EM imaging on vesicles comprised of DOPC and 6 mole% PIP_2 incubated with septin hexamers. As shown in Fig. 3.6 and the inset, the cryoEM images confirm that septins form paired filaments on negatively charged lipid membranes. The center-to-center distance between the filaments forming a pair is again on the order of ~ 6 nm, corresponding to a spacing of only ~ 2 nm. In addition, we observe single filaments, consistent with cryoEM observations for Cdc11-capped yeast septin octamers on vesicles [175]. The difference between the dense arrays on lipid monolayers and the more dilute arrays on vesicles is probably due to the difference in incubation time, which is much longer (overnight) on the monolayers than with the vesicles (30 min). Furthermore, on flat lipid monolayers, the protein can get more highly concentrated at the surface.

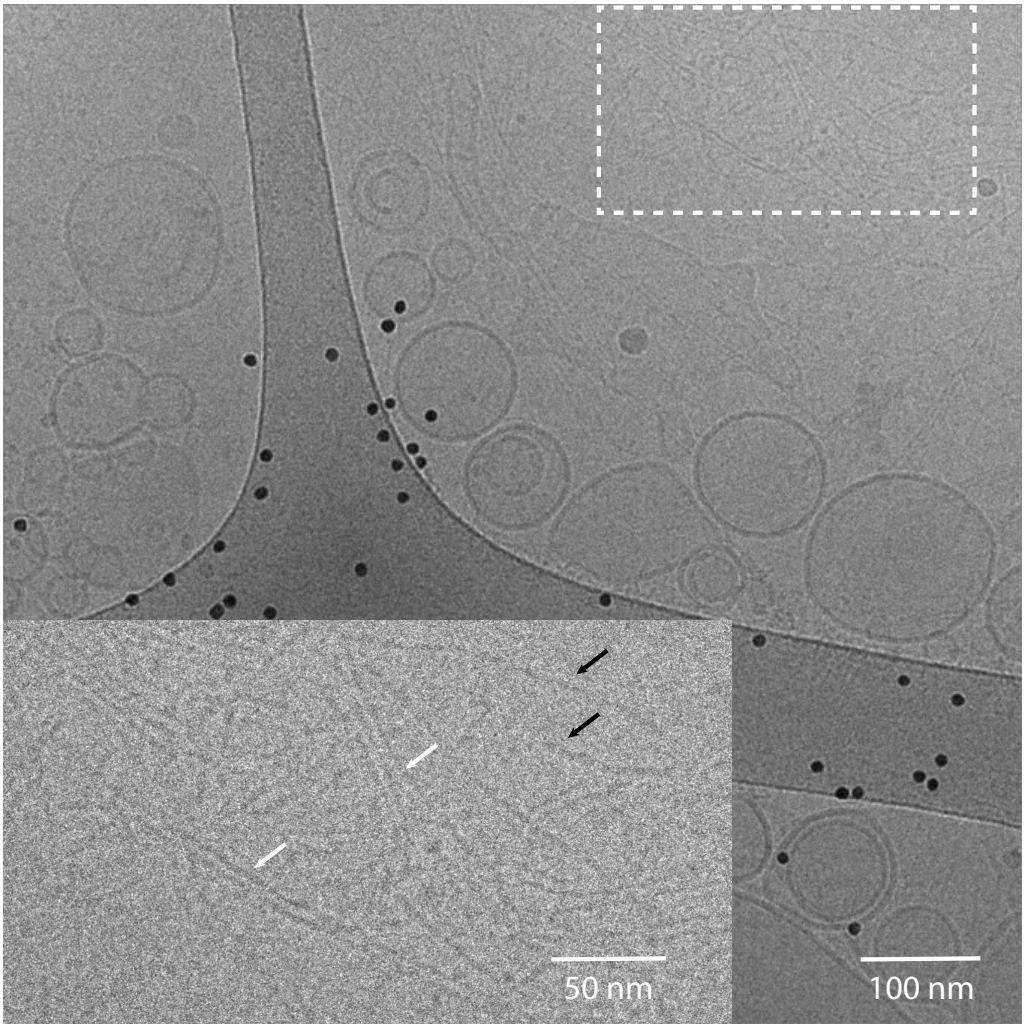

Figure 3.6: CryoEM images show that fly septin hexamers form single and paired filaments on lipid vesicles. Septins were incubated for 30 min at a concentration of 0.3 μM with vesicles composed of DOPC : DOPE : PIP_2 at molar fractions of 83 : 11 : 6%. The image shows septin filaments (linear structures), vesicles of different sizes and shapes, and gold nanoparticles that were included to enable tomography. The inset shows a zoomed-in region, where the black arrows indicate two examples of single filaments while the white arrows indicate two examples of paired filaments.

3.3.4 Atomic force microscopy imaging of septin-membrane interactions

The EM experiments indicate that the dense septin layers observed by TIRF imaging are comprised of predominantly paired septin filaments. However, the negative stain TEM imaging precludes experiments under native, hydrated conditions and on lipid bilayers, while cryoEM is restricted to highly curved bilayers. We therefore decided to complement EM imaging with AFM experiments, which allow us to image septins on flat lipid bilayers under hydrated conditions. Since septins formed identical structures on bilayers containing PS, PIP_2 or both, we decided to perform the AFM experiments only on bilayers containing 20% PS, which have previously been well characterized by AFM on different substrates [176]. We mostly imaged septins after fixation with 1% glutaraldehyde (GTA), because we found that this prevented septin disruption or dislocation by the AFM tip and facilitated reproducible imaging. The morphologies and heights of filamentous septin structures with and without GTA fixation were comparable (see Fig S2).

We first tested the dependence of septin assembly on septin concentration. Figure 3.7 shows examples of topographic images obtained at septin concentrations of 12, 24 and 60 nM, and at two different magnifications (panels A and B). When septins were incubated on bilayers at 12 nM, we observed a random distribution of isolated filaments on the bilayer surface (Fig. 3.7A left). Note that we did not observe filaments in the absence of membranes by TIRF or EM at such low concentrations (Chapter 2), which again highlights the catalytic effect of negatively charged membranes on septin polymerization. Height histograms of the AFM topography images showed two well-separated peaks, which we interpreted as the membrane surface and the septins, respectively (Fig. 3.7A and B). To estimate the fractional coverage of the surface by septins and the average septin filament height, we fitted the height histograms to a sum of two Gaussians and determined the areas under the peaks and the peak positions. The fractional coverage of the surface varied between 4 and 12% among different images, with an average coverage of ~ 9% (Fig. 3.7C). Note that this area fraction may be somewhat overestimated owing to tip convolution effects. The apparent average height of the septin filaments varied between 1.5 and 4 nm, with a systematic trend of smaller heights for larger scan sizes (Fig. 3.7D). These variations are likely due to differences in the force and scan rate with scan size, leading to varying degrees of indentation of the septin filaments by the AFM tip.

When the septin concentration was raised to 24 nM, we still observed mostly isolated filaments, although in certain regions the filaments formed areas of enhanced density (Fig. 3.7A,B middle). Height histograms again showed two well-separated peaks for the membrane surface and for the septins, respectively. The fractional area covered by septin filaments varied between 4 and 33% among different images, with an average coverage of ~ 21% (Fig. 3.7C), about twofold higher than at 12 nM. The apparent average height of the septin filaments ranged between 3 and 5 nm (Fig.

3.7D).

At the highest investigated septin concentration of 60 nM, the septins formed filaments that densely covered the bilayer surface (Fig. 3.7A right). The filaments formed patches comprised of locally aligned filaments, resembling nematic domains observed for other 2D arrays of densely packed semiflexible filaments such as F-actin packed at oil-water interfaces [177]. We often observed that septin bundles joined at a fairly shallow angle of ~15°, qualitatively consistent with the angles we observed in the EM images of septin filaments on lipid monolayers (see Fig. 3.5). Higher resolution scans of 5×5 μm areas more clearly revealed the packing arrangement of the septin filaments, but the lateral resolution was insufficient to confirm whether or not the filaments were paired (Fig. 3.7B). Histograms of the pixel heights no longer showed well-separated peaks for the membrane surface and the septins due to the dense packing arrangement of the septin filaments. Assuming that the membrane contributes to the histogram with a peak of similar width as observed at 12 and 24 nM, we see that the septin height histogram is apparently bimodal with one typical height of ~ 5 nm and one typical height of ~ 10 nm. The effective height obtained by summation of the histogram bars, setting the assumed membrane peak to a height of 0 nm, was ~ 6.6 nm.

The pixel height histogram analysis suggests that septin filaments form monolayers at 12 and 24 nM, and multilayers with a range of heights at 60 nM. To study the origin of this height variation, we performed a more detailed height analysis by determining height profiles along lines drawn perpendicularly to selected filaments imaged at different septin concentrations. As shown in Fig. 3.8A, the filament heights varied between 5 and 8 nm in case of the 12 nM septin sample. As shown in Fig. 3.8B, we observed a wider range of heights, between 6 and 14 nm, for the 24 nM sample. Height profiles of the dense septin filament arrays observed at 60 nM revealed filament heights that mostly ranged between 6 and 12 nm, with rare observations of heights going up to 17 nm (Fig. 3.8C).

To test whether GTA fixation affects the apparent height of the septin filaments, we performed a similar analysis on a 60 nM unfixed septin sample (Fig. 3.9). In areas where the surface coverage happened to be low enough, we could observe isolated septin filaments. The height of these isolated filaments never exceeded 4 nm (Fig 3.8A and B), corresponding to the height of a single septin hexamer. We regularly observed cases where filaments ran close together and in parallel across a part of their length. These bundled regions either had an increased height of up to 12 nm, suggesting that septin filaments can stack on top of each other (Fig. 3.9C), or the height remained the same as for isolated filaments, suggesting that septin filaments can also associate in the plane of the membrane to form flat bundles (Fig. 3.9D). This range of heights is similar to the height range observed for GTA-fixed samples, indicating that the fixation treatment does not affect septin filament organization.

Since AFM imaging involves mechanical scanning across the surface, we can qualitatively test how firmly the septins are attached to the lipid bilayer by performing multiple consecutive scans. As shown in Fig. 3.10A, densely covered regions

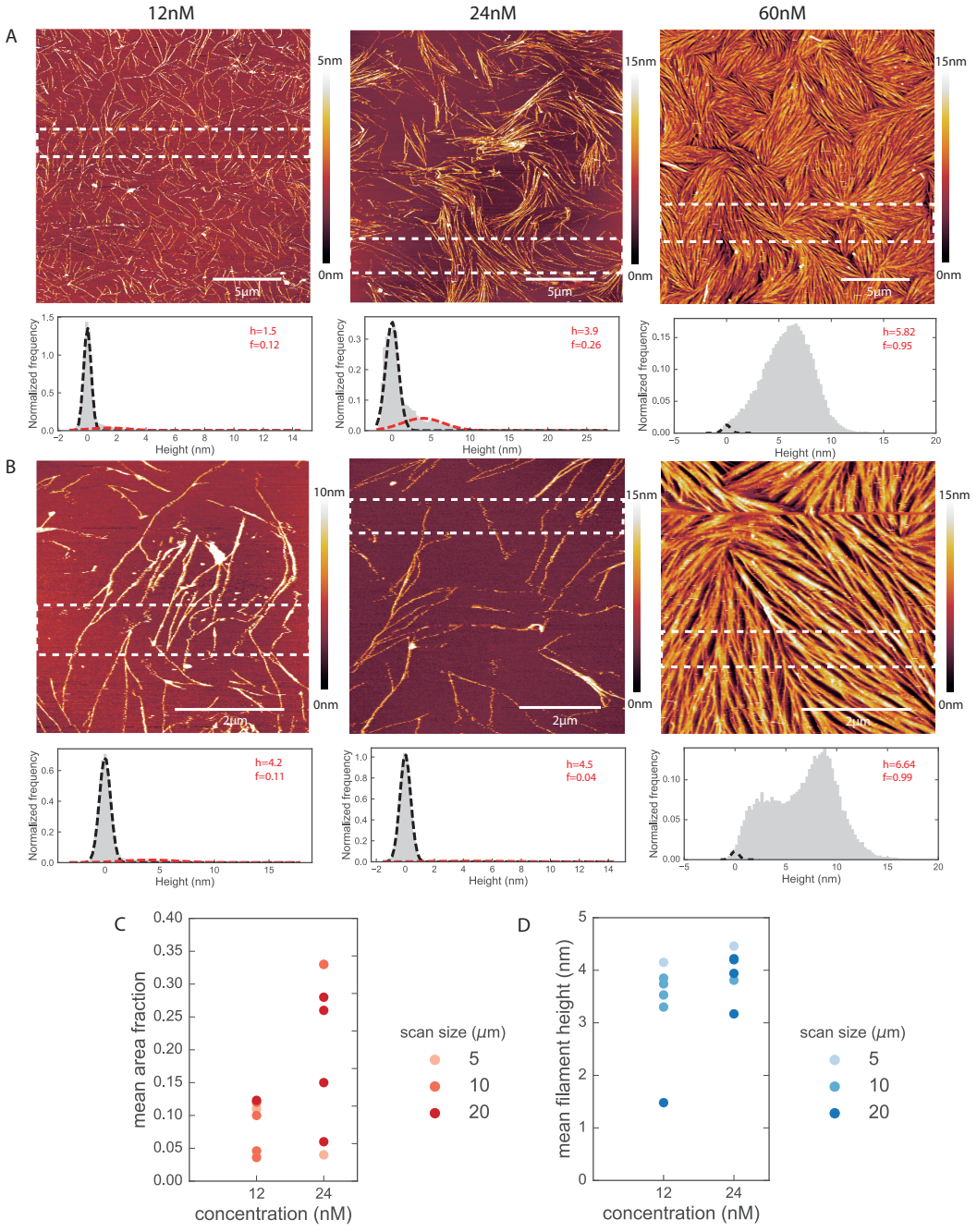
12nM
24nM
60nM
A
B
5nm
15nm
10nm
0nm
5µm
2µm
h=1.5
f=0.12
h=3.9
f=0.26
h=5.82
f=0.95
h=4.2
f=0.11
h=4.5
f=0.04
h=6.64
f=0.99
Normalized frequency
Height (nm)
C
mean area fraction
concentration (nM)
scan size (µm)
5
10
20
D
mean filament height (nm)
concentration (nM)
scan size (µm)
5
10
20

formed at a septin concentration of 60 nM were unchanged after three consecutive scans (which took 10 min each). Both the septin filaments and their higher-order arrangement in nematic-like patches remained unchanged, suggesting that the septin structures are firmly attached and also that they do not remodel on this experimental time scale. By contrast, septin filaments in sparsely covered regions were clearly disturbed by the AFM tip because the filaments appeared ragged. The tip likely moves the filaments over the surface. We observed this behavior for septins imaged with and without GTA fixation (Fig. 3.10B). Unfortunately, this mechanical instability made it impossible to resolve single filaments at higher resolution. Taken together, these observations suggest that individual septin filaments are mechanically fragile, whereas septin filaments that laterally interact within bundles or dense arrays are mechanically stabilized.

The enhanced mechanical stability of dense septin arrays made it possible to obtain a few AFM scans at higher resolution, which revealed some interesting new features that could not be observed at lower resolution (Fig. 3.11). For example, all the bundles we observed had visible striations oriented parallel to the bundle axis, indicative of multiple thin filaments running in parallel (Fig. 3.11A). The bundles with the lowest heights were around 4 nm high (Fig. 3.11B, profiles 1 and 2), suggesting that they are composed of one layer of septins. Thicker bundles had heights of ~12 nm (Fig. 3.11B, profile 4). We furthermore observed height modulations along the bundle axis, with local increases in height up to 16 nm (Fig. 3.11B, profile 3). The spacing between the modulations was irregular, varying from 38 to 60 nm, and did not correspond to an integer multiple of the hexamer length (24 nm) (Fig. 3.11C). Interestingly, the width of the modulations in the direction perpendicular to the bundle long axis was comparable to the bundle width and corresponded to roughly a double hexamer length (Fig 3.11D). The peak heights along profiles 1, 2 and 3 in panel D are 6, 8 and 9 nm, so the interval between the

Figure 3.7 *(preceding page)*: AFM topographic imaging shows that septins form flat filamentous structures on lipid bilayer membranes composed of 80% DOPC and 20% PS. Images show filamentous septin structures obtained at concentrations of 12, 24 and 60 nM (legend on top) and observed at a scan size of 20 ×20 μm (A) and ~5 ×5 μm. (B). Histograms below the images show the height distribution of the pixels for the regions indicated by the white dashed rectangles (see color bar on the right). At 12 and 24 nM, the first peak (black dashed line) corresponds to the membrane while the second peak (red dashed line) corresponds to the septin filaments. At 60 nM, the membrane and septin signals are not well-separated and we observe an apparently bimodal distribution of septin filament heights. (C) Area fraction covered by septin (f) as a function of septin concentration, obtained by integration of the second peak in the height histograms. (D) Mean height of the septin structures (h) as a function of septin concentration, obtained as the position of the second peak (after background subtraction) in the height histograms. Each data point in panels (C) and (D) corresponds to a region of a different image obtained at scan sizes as indicated in the legends.

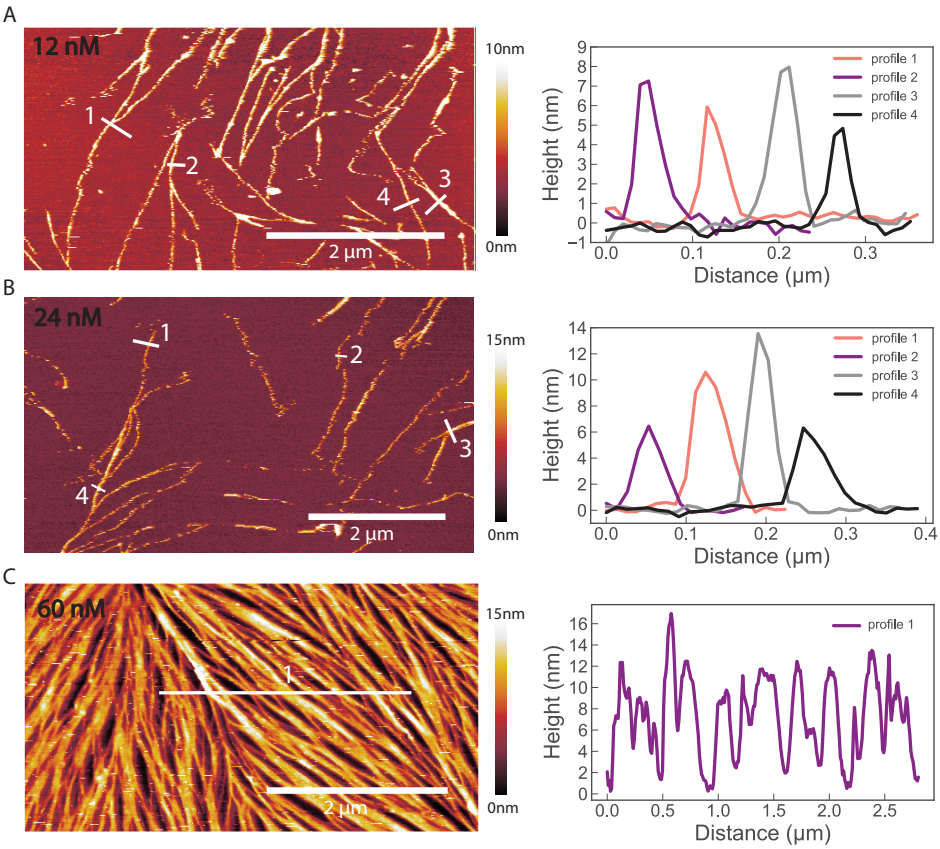

Figure 3.8: Height analysis based on line profiles across septin filaments observed by AFM topographic imaging. The images on the left present selected regions from images presented in Fig. 3.7B. The graphs on the right present height profiles along the lines depicted on each image. (A) At a septin concentration of 12 nM, we observe sparsely distributed filaments ranging in height from 5 to 8 nm. (B) At a septin concentration of 24 nM, we still observe sparsely distributed septin filaments, ranging in height from 6 to 14 nm. (C) At a septin concentration of 60 nM, we observe a densely packed layer of septin filaments. Height profiles show that septin bundles reach heights of 6 to 12 nm and, in rare cases, even 17 nm. Here we assume that the AFM tip can reach the bilayer surface in between adjacent septin bundles despite their dense packing, based on the reproducible height of the troughs.

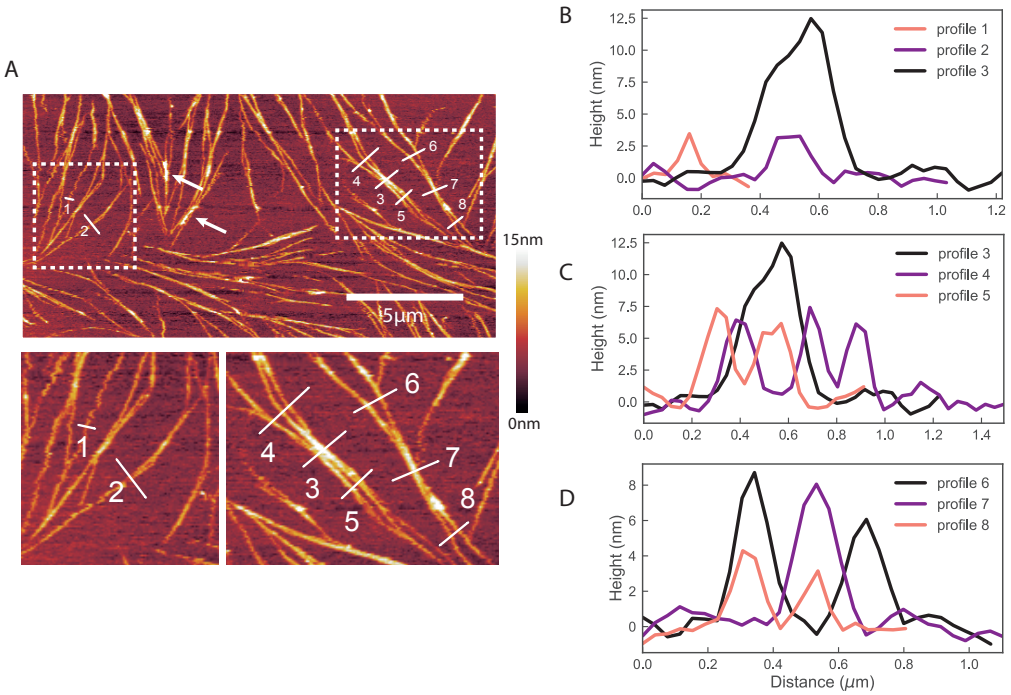

Figure 3.9: Height analysis based on line profiles across unfixed septin filaments imaged by AFM. Septins were incubated at 60 nM on lipid bilayers composed of 80% DOPC and 20% PS. (A) Isolated septin filaments in a sparsely covered region of the bilayer. White arrows indicate filaments with short (~ 1 µm) segments of increased height. Scale bar for the top panel: 5µm. Bottom panels show zoomed-in versions of the dashed rectangles in the top panel. (B) Height profiles along the lines numbered 1, 2 and 3, drawn perpendicularly across septin filaments in panel (A). (C) Height profiles along the lines numbered 3, 4 and 5 in panel (A), drawn perpendicularly across regions where multiple septin filaments join to form a bundle of increased height. (D) Height profiles along the lines numbered 6,7 and 8 in panel (A), drawn across regions where multiple septin filaments join to form a flat bundle.

height modulations is less than the height of a single septin hexamer (4 nm)(Fig 3.11D).

In a single experiment performed in a first round of AFM experiments, we observed flat septin bundles at 60 nM that lacked the height variations described above (Fig. S3). In this experiment, we observed flat bundles with an average height of 4 nm showing striations along the bundle axis indicative of thin filaments joined together. We suspect that these flat bundles composed of single filaments may act as a template for recruiting additional septin hexamers/filaments on top, which were perhaps washed-off during sample preparation.

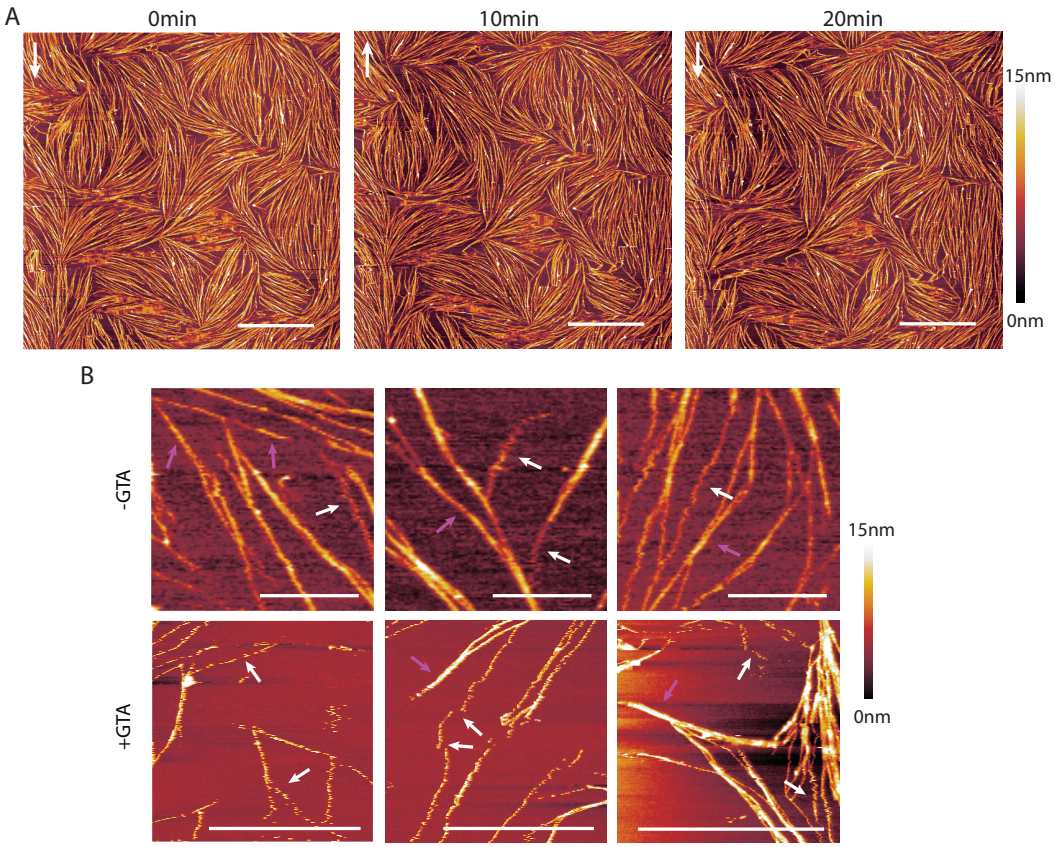

Figure 3.10: AFM imaging shows that septin bundles and dense septin arrays are more mechanically stable than isolated septin filaments. Septins were incubated at 60 nM on lipid bilayers composed of 80% DOPC and 20% PS. (A) Same region of a sample scanned three consecutive times in 10 min intervals ($t = 0$ indicates the initiation of the first scan). Septin filaments and their higher-order arrays are unchanging and immobile. White vertical arrows show direction of the scans. Scale bars: 5 µm. (B) Single septin filaments are mechanically unstable, both in unfixed conditions (-GTA) and after fixation with 1% GTA (+GTA). White arrows show examples of filaments that appear perturbed, as indicated by a 'zigzag' shape, most likely due to the AFM tip moving the filament across the membrane. Pink arrows show stable filaments or bundles.

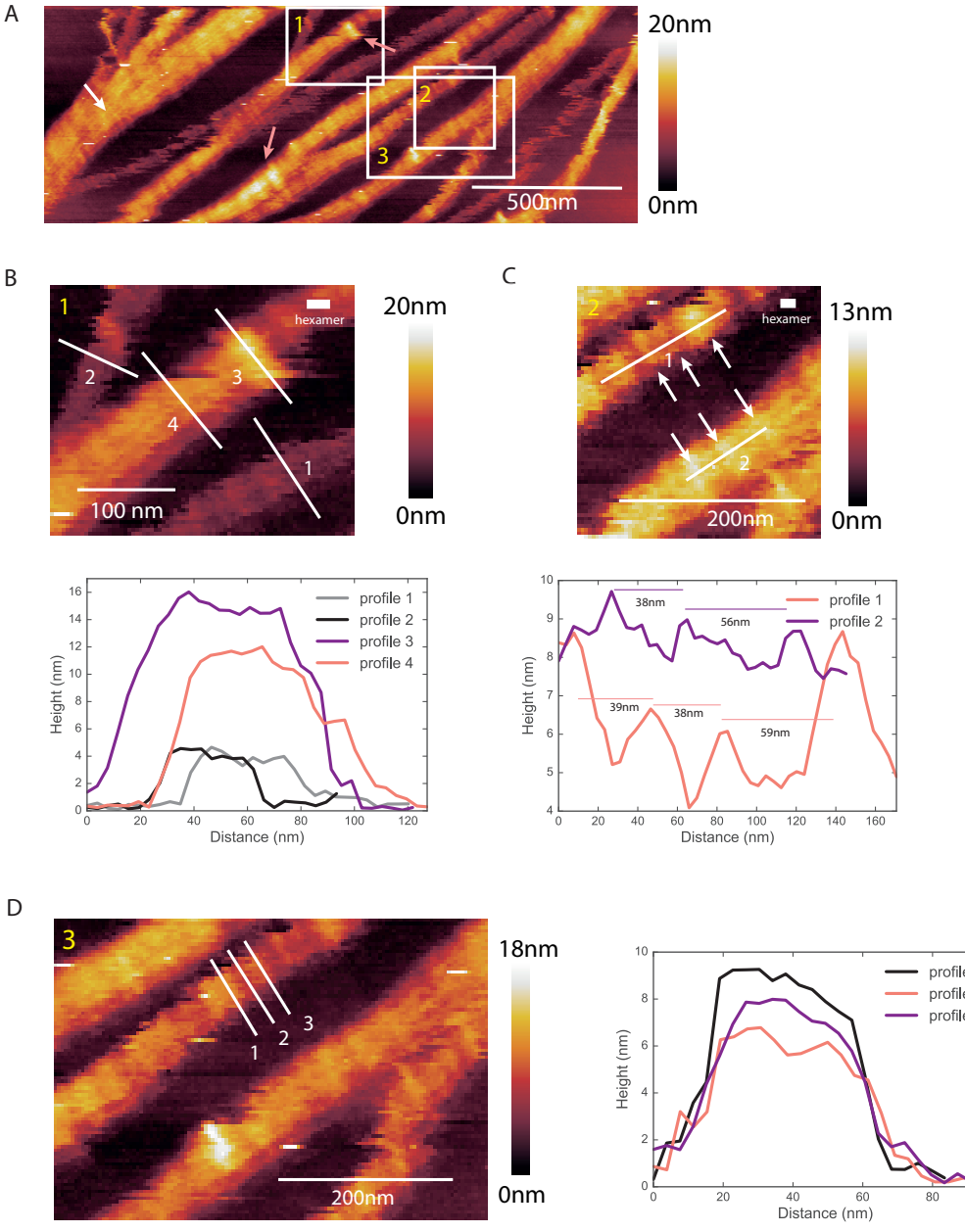
A
1
2
3
500nm
20nm
0nm
B
1
hexamer
2
3
4
1
100 nm
20nm
0nm
profile 1
profile 2
profile 3
profile 4
Height (nm)
Distance (nm)
C
2
hexamer
1
2
200nm
13nm
0nm
38nm
56nm
39nm
38nm
59nm
profile 1
profile 2
Height (nm)
Distance (nm)
D
3
1
2
3
200nm
18nm
0nm
profile 1
profile 2
profile 3
Height (nm)
Distance (nm)

Figure 3.11 ***(preceding page)*****: High resolution AFM images reveal longitudinal and lateral height modulations on septin bundles.** Septins were incubated at 60 nM on lipid bilayers composed of 80% DOPC and 20% PS. (A) Flat septin bundle with striations running parallel to the bundle axis (white arrow), suggesting that the bundle is composed of multiple filaments. Pink arrows show bands of increased height that are oriented perpendicularly to the bundle axis. (B) Zoom-in of region 1 from panel A. Height profiles along the numbered lines reveal the presence of thin bundles with a height of ~ 4 nm and thicker bundles with a height ranging between 12 and 16 nm. (C) Zoom-in of region 2 from panel A. Arrows indicate height modulations along the bundle. Height profiles along the numbered lines show that the spacing between the height modulations is irregular. (D) Zoom-in of region 3 from panel A. Height profiles along the three numbered lines show that the high stripes have different heights with increments of less than 4 nm. The length of the stripes matches the bundle width (~40 nm, measured as the length of the plateau).

3.4 Discussion

3.4.1 Septins form rigid membrane-anchored networks

In this chapter we investigated the influence of membrane-binding on septin assembly by reconstituting recombinant septins on supported lipid bilayers and by imaging septin assembly using several complementary imaging techniques. We showed by fluorescence imaging that fly septin hexamers have a high affinity for negatively charged lipid bilayers and form dense membrane-associated meshworks. The amount of adsorbed septins increased linearly with the areal fraction of anionic lipids present in the membrane and with the bulk concentration of septins in solution. Electron microscopy (EM) imaging of septins on lipid monolayers and on vesicles revealed that these septin meshworks are predominantly comprised of paired filaments and bundles thereof. This finding is consistent with previous observations of native porcine septin hexamers on the outer surface of GUVs [55]. Interestingly, cryoEM imaging of vesicles incubated with septins revealed that paired filaments co-exist with single filaments, which implies that filament pairing is not a necessary requirement for septin polymerization. Finally, atomic force microscopy (AFM) of septins on lipid bilayers showed that septin filaments laterally associate into bundles. At high surface densities, the septin bundles form stable networks that are so dense that adjacent bundles align to form organized domains. Both AFM imaging and fluorescence recovery after photobleaching experiments suggest that the septins are immobile and firmly attached to the membrane.

Prior *in vitro* studies of septin-membrane binding focused mainly on mitotic, Cdc11-capped yeast septin octamers [61, 62]. We find that there are several similarities between the membrane interactions of fly septin hexamers and yeast septin octamers. First, membrane binding in both cases has a catalytic effect on septin polymerization. For fly septin hexamers, the threshold for polymerization is lowered by an order of magnitude, from 200 nM in solution to less than 12 nM on negatively charged membranes (in the presence of 20% PS and with a 15 min incubation time). For yeast septins, a similar catalytic effect was observed on membranes containing PI or PIP_2 [61, 62]. The catalytic effect of membrane binding is likely due to the increase of the effective septin concentration caused by 2D confinement [61, 62]. A second similarity between the behavior of fly and yeast septins on membranes is that they both form paired filaments with a narrow spacing of less than 2 nm, much less than the length of the long carboxy-terminal coiled coil domains that are thought to mediate pairing. A third similarity is that paired filaments of both fly and yeast septins are interconnected by bridges, which appear to be formed by short and thin (single) septin filaments having a length and axial spacing that correspond to the length of a single oligomer [62].

Our work also reveals two striking differences between fly and yeast septins. The first difference is their polymerization in solution. Fly septins form thick and rigid bundles with tapered ends in solution. We showed in Chapter 2 that these bundles

are comprised of tens to hundreds of subunits per cross-section, suggesting that fly septins have strong lateral interactions that promote bundling. On membranes, however, we observed a gradual transition from dilute arrays of thick bundles to dense arrays of paired filaments with increasing net surface charge. This observation suggests a competition of septin-membrane interactions with lateral septin-septin interactions, which suppresses the formation of thick bundles on membranes. By contrast, yeast septin octamers form paired filaments both in solution and on membranes. Thus, in solution fly septins have a stronger propensity for bundling than yeast septins, but on membranes the two septins behave similarly. The second striking difference between yeast and fly septins revealed in this Chapter is their membrane binding selectivity. We find that fly septins form similar structures on membranes containing PS or PIP_2, and that the main determinant of fly septin binding and filament organization in both cases is the net surface charge of the membrane. We also performed experiments with PIP_3 (5%), which resulted in a similar meshwork as in case of PIP_2 (see Fig.S4). By contrast, Cdc11-capped yeast septin octamers were shown to be highly selective for PI, PI(4)P, PI(5P) and PI(4,5)P_2, while they did not interact with PS [40, 61–63, 77, 144, 159, 178]. The origin of the differences in lipid specificity remain unknown. It is thought that septins interact with negatively charged phospholipids via a polybasic region close to the N-terminus that is composed of a sequence of 2-6 basic amino acids [63, 65]. This stretch is very similar to polybasic sequences found in gelsolin, profilin, G-protein-coupled receptor kinases and ion channels [65], which are all reported to interact with PIP_2. In future perhaps molecular dynamics simulations can shed light on the interactions taking place at the septin-membrane interface and identify the determinants of lipid selectivity [179].

3.4.2 Towards a model of septin assembly on membranes

What do the imaging experiments collectively teach us about the assembly mechanism of fly septin hexamers on lipid membranes? A firm conclusion is difficult because there are still a number of important unknowns. It is still under debate where the membrane-binding region is located, what is the precise spatial arrangement of the long carboxy-terminal coiled coils, and whether there are other interactions (for instance through the globular domains) that may contribute to septin-septin interactions. However, our imaging experiments do provide some interesting clues, especially when we consider the similarities to yeast septins, for which more structural information is available. Below we present a speculative model of membrane-templated septin self-assembly, which is illustrated in Fig. 3.12.

Fly septin hexamers are recruited to the membrane by electrostatic interactions with anionic lipids (PS and/or PIP_2), likely via their polybasic domain. Note that the hexamers are drawn with the Pnut subunits at the termini, based on the homology of fly septins to human Sept2-Sept6-Sept7 hexamers, where this arrangement was originally proposed [34]. However, two recent studies show evidence for an alternative

arrangement, with the Pnut subunits in the center, which is more consistent with the subunit arrangement of yeast septins [35, 36]. In the schematic, we also indicate the C-terminal domains of the septin subunits, which are predicted to adopt a coiled-coil arrangement [86]. DSep1 subunits have short coiled coils whose length is predicted to be ~4 nm, while DSep2 and Pnut subunits have long coiled coils with a predicted length of ~13 nm. These lengths were calculated by Dr. M. Mavrakis (Institut Fresnel) using the COILS software [180]. The short coiled coils have been proposed to be involved in stabilization of the hexamer [86], although human septin hexamers comprised of C-terminally truncated subunits have been reported to be stable [34]. As we will show in Chapter 4, we indeed also observe hexamers (and dimers thereof) by EM in solution for septin hexamers where all C-termini are truncated. The long coiled coils have been proposed to be involved in septin filament pairing and in higher-order interactions [62]. The coiled coils are known to be flexible, because they do not show up in in X-ray crystal structures or particle-averaged electron microscopy analysis. EM images of *C. elegans* septins showed that the coiled coils can sweep out a large volume [20]. Based on this evidence, we assume that the coiled coils can rotate in the entire half-plane above the membrane, so they are available for both in-plane and out-of-plane interactions with coiled coils on neighboring septin subunits/filaments.

Once septin hexamers are adsorbed onto the membrane, they form paired filaments in the membrane plane via end-to-end association mediated by homodimerization of the terminal subunits of adjacent hexamers and via lateral associations mediated by the long coiled coils. We observed in EM images that paired filaments have a narrow gap of only 2 nm, which is much smaller than the contour length of the coiled coils. On the other hand, this distance is too large to be explained by interactions mediated by the globular domains. As we will show in Chapter 4, negative stain EM images of C-terminally truncated septins on lipid monolayers reveal aligned filaments with a center-to-center spacing of around 4 nm. In this case, filament-filament interactions can only be mediated by the G-domains. We therefore conclude that pairing of filaments formed by full-length septins must be mediated by coiled coil pairing. But to accommodate the paired long coiled coils in between the filaments, they must either stick out or fold and collapse.

Our EM images showed that paired filaments are often bridged by short septin filaments, whose length corresponds to that of a single hexamer in case the bridge is perpendicular or to that of two hexamers when the bridge is under an angle. Similar bridges were observed for yeast septin octamers on lipid monolayers, where the bridge length and spacing were also multiples of the octamer length [62]. The interpretation in that case was that at least some C-terminal extensions on the terminal Cdc11 subunits of paired filaments were free to engage in interactions with C-terminal extensions on the bridging filaments.

To explain why septins form multi-layers, we hypothesize that some long coiled coils remain unpaired and are therefore available to recruit additional septin hexamers/filaments. These coiled coils can likely mediate both in-plane and out-of-

plane association between septin filaments. Based on our data showing a limiting septin film height of ~17 nm, we conclude that in-plane association is more likely than recruitment of a new layer of septins, so that with increasing layer height, there is a smaller and smaller probability of recruiting additional material on top. We thus end up with septin arrays that are very extensive in-plane, but limited in height.

Our data still leave open a number of questions. First, we observed height modulations by AFM, not shown in the schematic model, which may perhaps represent protruding C-terminal coiled-coils. These height modulations are reminiscent of the periodically spaced density modulations on bundles of paired filaments of monolayer-bound yeast septins seen by EM [62]. Second, it is unclear to what degree the globular domains of septins contribute to septin filament bundling. An earlier EM study of yeast septin octamers on lipid monolayers suggested the possibility that single filaments can pair by interactions of the globular domains [62] and our own EM data for C-terminally truncated fly septins presented in Chapter 4 also suggest that the G-domains are capable of mediating filament-filament interactions. Third, it remains unclear which domain of the septin molecule interacts with the membrane, and therefore what is the exact 3D-orientation of septins on the membrane. It is generally believed that the polybasic domains of septins interact with the membrane, which would leave the coiled coils free to rotate in the half-space above the membrane. However, a recent study on yeast septins suggested that membrane binding is aided by an amphipathic helix [144]. Molecular dynamics simulations and EM tomographic imaging will be needed to resolve these questions.

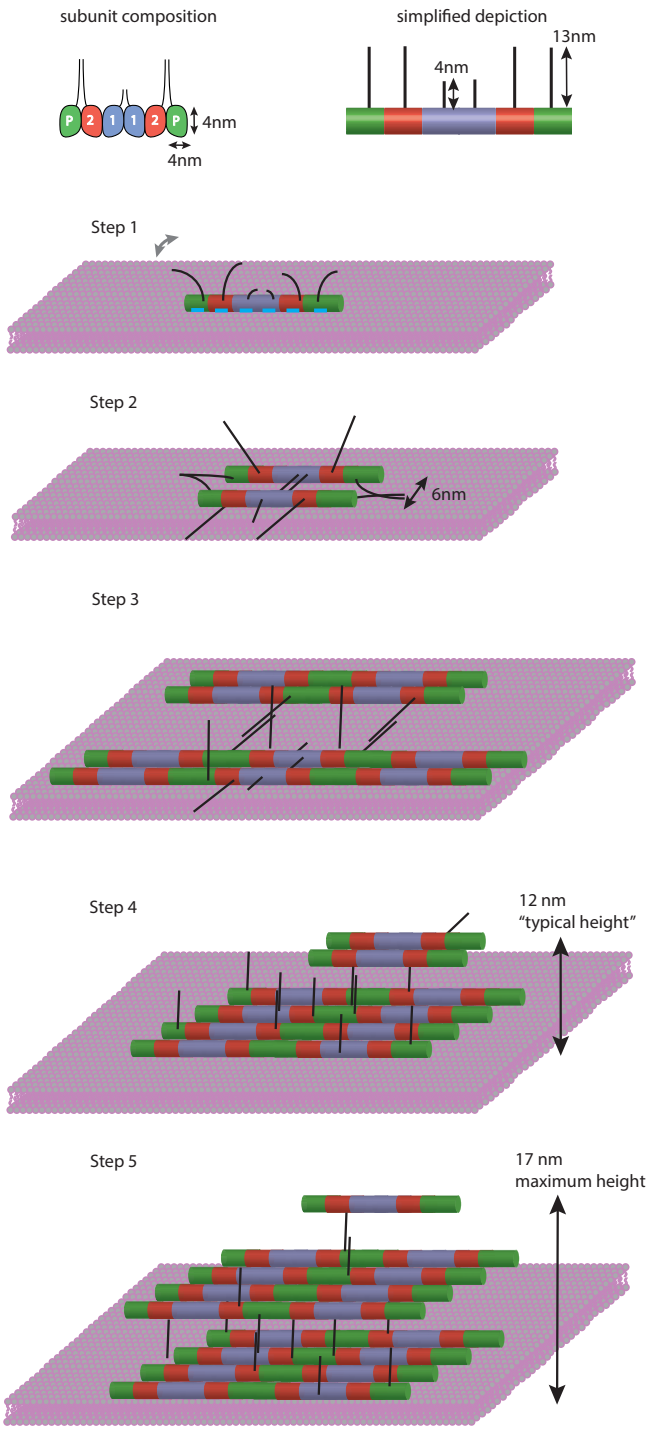

Figure 3.12: Steps of septin filament multilayer assembly. Step1: Binding of septin hexamer to negatively charged lipid membrane, Step 2: Paired septin filament formation, Step 3: Paired filaments form sheets in the membrane plane, Step 4: Stacking of multiple septin layers, Step 5: Final membrane-adsorbed septin layer.

3.4.3 Biological implications

Our observations of extended and mechanically stable septin filament networks on model biomembranes suggest the possibility that septins may directly enhance the cortical rigidity of cells by forming filaments on the inner leaflet of the plasma membrane. With their high stability, septins could furthermore have an important role in mechanical integration of the cell cortex, since the actin-myosin cortex in mesenchymal and epithelial cells is known to turn over rapidly [181–184]. Although septins in cells are more dynamic than *in vitro*, with typical *in vivo* half-times for fluorescence recovery on the order of 100 s (depending on septin subunit), the turnover rate of septins is still slower than for actin (where the half-time for fluorescence recovery time is on the order of tens of seconds) [92]. In the context of amoeboid T-cell migration, it has for instance been suggested that stable septin structures are important to ensure directional extension of leading-edge protrusions [48]. To test whether septins indeed interact directly with the membrane at the cell cortex, one could use advanced 3D-superresolution techniques such as 3D-SIMS [185] and EM tomography [150] to study the proximity of cortical septins to the cell membrane and resolve their ultrastructure.

In our study, we focused on the interactions of septins with flat membranes, motivated by the functions of septins in the cell cortex. In future it will be interesting to test whether fly septins have any preference for curved substrates and whether curved substrates influence septin organisation, as was shown recently for yeast septins by scanning electron microscopy [41, 144].

Acknowledgements

I greatly thank the co-authors of this thesis chapter, Fouzia Bano & Ralf Richter (Leeds University), Manos Mavrakis (Institut Fresnel, Marseille), and Aurélie Bertin (Institut Curie, Paris) for sharing expertise, materials, data and insightful discussions. I thank Cristina Martinez Torres for discussions on the AFM data analysis. I thank Francois Iv (Institut Fresnel, Marseille) for teaching me all the details about septin purification. I thank Marjolein Kuit-Vinkenoog for protein purification. I acknowledge Dimitrios Vavylonis (Lehigh University) for teaching me the use of his software JFilament. For critical reading of the manuscript, I thank Manos Mavrakis, Aurélie Bertin, Ralf Richter and Gerard Castro Linares.

3.5 Supplemental material

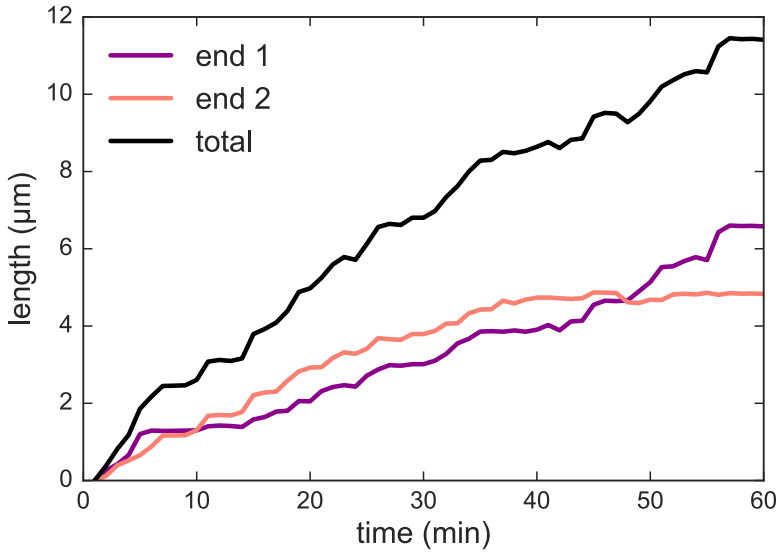

Figure S1: Growth of septin bundles occurs on both ends. Septins at a concentration of 500 nM were flushed onto a DOPC bilayer doped with 2.5 mole% PS. Bundle growth was tracked with the open source J-Filament Plugin for ImageJ developed at Lehigh University [186]. Displacement of the two ends was measured in time. Both bundle ends grow with a similar rate. The total growth rate is 0.26 μm/min. For comparison, the growth rate of budding yeast septin filaments (at 3 nM) was reported to be much faster (~ 4.5 μm/min), although this measurement was taken on a significantly more highly charged membrane containing 22% PI and 3% PI(4,5)P_2.

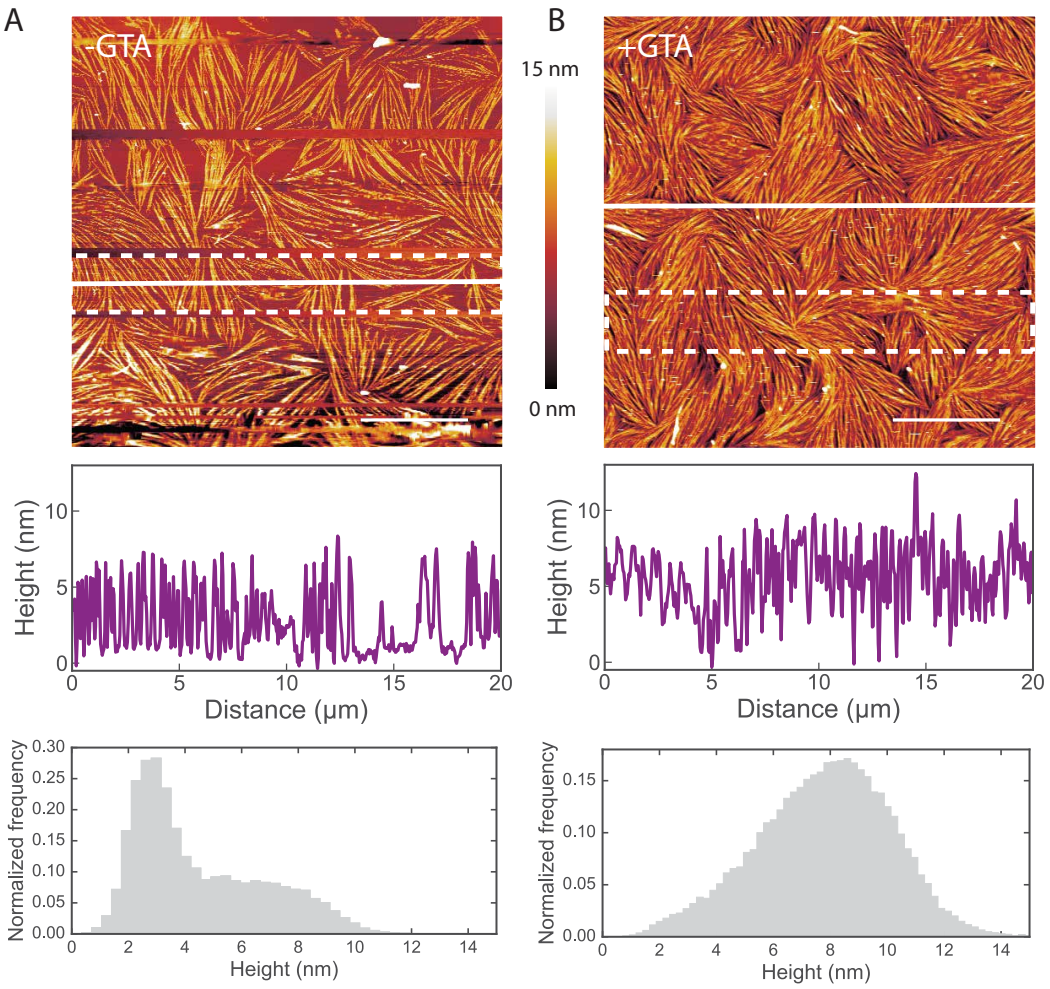

Figure S2: AFM images show that glutaraldehyde fixation does not change the gross morphology of septins (60 nM) adsorbed to supported lipid bilayers (DOPC and 20 mole %DOPS). The bundles and their liquid-crystalline organisation are preserved. (A) Image of unfixed septin filaments. (B) Image of septin filaments fixed by GTA treatment. Scale bar: 5 µm. The graphs below the images present height profiles along the lines depicted on each image Note that the two samples were prepared independently, and that differences in surface density are likely due to slight variations in the sample preparation conditions. Occasional lines appearing empty correspond to phases when the AFM tip lost contact with the surface. The histograms show pixel height distributions within the regions depicted with dashed lines on each image. We suspect that slightly lower heights of unfixed septin filaments are due to higher forces necessary to apply to image the filaments without losing the tip. Another possibility is that lower heights are related to lower surface density.

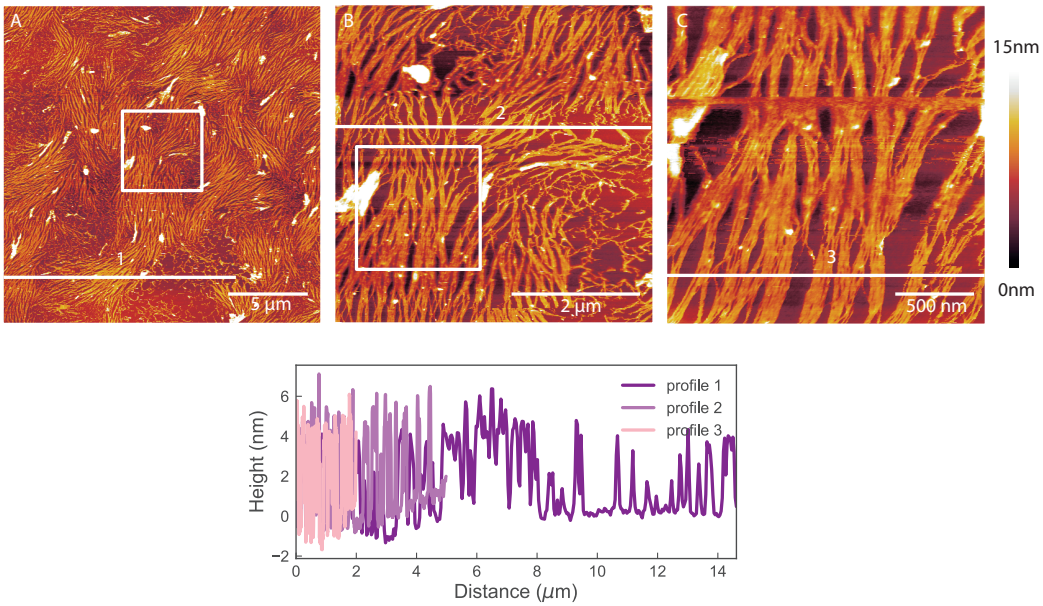

Figure S3: Summary of a single experiment that showed the formation of rather flat arrays of fixed septin filaments at 60 nM. (A) Septin filaments imaged at a large scan size (20 µm). (B) Zoomed-in image corresponding to the boxed region in panel A, and (C) zoomed-in image of the boxed region indicated in panel B. Septins form flat bundles comprised of aligned thinner filaments; some filaments diverge from one bundle and later merge with another. The graph shows line profiles (numbered in panels (A-C)), which suggest that the septin bundles are flat, with a height of 4 nm, corresponding to the thickness of a single filament. Average height for the three selected regions of the images shown here is 3.7±0.2. There are, however, short stretches of filaments or bundles that are clearly higher than 4 nm. These short stretches are aligned with membrane-proximal filaments.

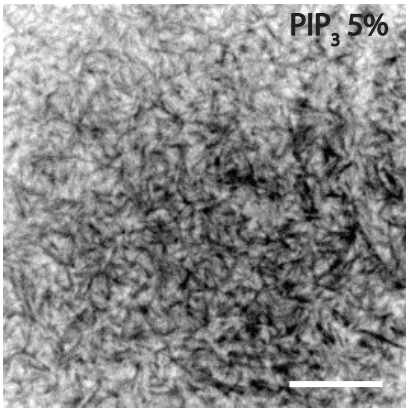

Figure S4: Septins form a thin meshwork on lipid bilayers containing 5% PIP_3. Image shows septins at 1 µM on DOPC bilayers doped with 5% PIP_3 forming a thin meshwork similar to what we observed for DOPC bilayers doped with PIP_2(Fig. 3.1). The image contrast is inverted. Scale bar: 10 µm.

4

Binding and self-assembly of septins on model biomembranes

Septins are cytoskeletal proteins that participate in various cellular processes that depend on the cell cortex. They form filamentous structures that rigidify the cortex and they compartmentalize the plasma membrane, thus regulating cell division and migration. The molecular mechanisms that determine the assembly of septins into filamentous structures in association with the plasma membrane remain poorly understood. In this chapter we use a cell-free reconstitution assay to quantitatively measure the kinetics of septin binding to solid-supported model lipid bilayers. Quartz-crystal microbalance (QCM-D) measurements show that septins strongly adsorb to negatively charged lipids by an electrostatic interaction and that the adsorption kinetics is mass transport limited. We further demonstrate that septins form a relatively rigid film that consists of at most 3 layers of septins. Combined QCM-D and spectroscopic ellipsometry (SE) measurements confirm that the growth of septin films is self-limited over a range (12-60 nM) of septin concentrations. We furthermore find that the fraction of hydrodynamically coupled solvent is nearly 80%, indicating a porous film structure. Consistent with the QCM-D and SE measurements, nanoindentation measurements with an atomic force microscope show a maximal film thickness of 18 nm. Our findings suggest a model for membrane-mediated septin assembly whereby septins form extended networks on the membrane with a limited build-up in height. It will be interesting to compare these in vitro insights with future measurements of the arrangement of cortical septins in cells.

4.1 Introduction

Septins are cytoskeletal proteins that participate in many cellular processes that require reorganization or reshaping of the plasma membrane [16]. In various fungi,

septins for instance form filamentous rings at the membrane that scaffold the cell division machinery [149, 187]. In animals, septins also play scaffolding roles during cell division [75]. In addition, they have a wide range of other functions at the cell cortex. They form ring-shaped collars that reinforce sperm cells [188] and form the base of various membrane appendages such as ciliae and dendritic spines [161, 162]. Septins are typically present all along the cell cortex and control various morphogenetic events by influencing cortical rigidity. Examples are amoeboid cell migration and tissue development [48, 49].

The molecular mechanisms by which septins perform these functions remain poorly characterized. In yeast cells, there is strong evidence that the functional form of septins is provided by rigid fibrillar meshworks bound to the membrane. Yeast cells express several different septins that form rod-shaped hetero-octamers [19, 165]. The octamers can in principle form semiflexible filaments on their own [19, 77, 78, 165], but lipid membranes strongly promote filament assembly by concentrating septins and facilitating diffusion-driven annealing [61, 62, 158]. Reconstitution studies have shown that yeast septins interact with lipid membranes mainly through an N-terminal polybasic domain that specifically binds to certain phosphoinositide lipids [40, 61–63, 159]. Single molecule fluorescence imaging showed that individual yeast septin octamers do not stably associate with membranes, whereas filaments are strongly bound [144]. Quantitative microscopy measurements of septin binding furthermore suggested that septin binding is cooperative [144]. Electron microscopy imaging showed that septins are able to polymerize on membranes under conditions where they do not assemble in solution, such as high-salt conditions [62]. It has been suggested that this cooperativity contributes to the ability of septins to recognize micron-scale membrane curvature [40, 144].

In animal cells it is clear that many functions of septins also play out near the cell membrane [16]. However, it is not yet clear whether septins actually directly associate with the membrane. Purified septins from various animal species have been shown to associate via an electrostatic interaction with anionic lipids, including phosphoinositides [40, 55, 64–66] and phosphatidylserine [51] (see also the evidence shown in Chapter 3 of this thesis). However, purified septins also interact with actin filaments and various actin-binding proteins [43, 53, 54, 71, 94]. Actin-binding could provide an alternative mechanism to recruit septins to the cortex, given that a dense actin meshwork known as the actin cortex lines the entire surface of the membrane in animal cells [189]. Electron microscopy has indeed demonstrated co-localization of septins with actin in the cortex, but has not resolved whether septins are membrane- or actin-bound [91, 92]. It therefore remains an open question whether septins directly reinforce the cell cortex by forming membrane-bound filament arrays, or whether they indirectly regulate the cortex by either tethering actin filaments to the membrane or crosslinking the actin cortex.

To answer the question how septins function in the cell cortex, it is therefore important to disentangle the influence of its many binding partners on its assembly. In vitro reconstitution of cell-free model systems provides an ideal approach because

it allows a quantitative characterization of specific interactions in the absence of confounding factors [190, 191]. Until now there has only been a handful of studies on the interactions of animal septins with lipid membranes. Two studies showed that septins can cause tubulation of cell-sized vesicles and can influence the lipid organization in supported bilayers [55, 66]. It was furthermore shown that porcine as well as human septins form dense filamentous arrays on the vesicles that resemble arrays formed by yeast septins [55, 66]. In our own lab, we recently studied the interactions of recombinant Drosophila septins with solid-supported lipid bilayers by fluorescence, electron and atomic force microscopy, where we found that these septins also form densely packed layers of filaments on membranes containing anionic lipids. (c.f. Chapter 3).

While imaging can provide important information on the structure of membrane-bound proteins, it is often limited in the ability to measure the kinetics of membrane-binding. First, imaging can be invasive. For instance, optical microscopy generally requires fluorescent labeling, electron microscopy (EM) requires freezing or dehydration, and atomic force microscopy (AFM) involves mechanical contact with a scanning force probe. Second, many microscopy techniques (in particular EM and AFM) have a restricted temporal resolution. In recent years, there has been a growing interest in the development of surface-sensitive biosensors that can overcome these limitations [192]. Here we use two complementary surface-sensitive techniques that both provide label-free and real-time measurements of protein-membrane interactions: quartz crystal microbalance with dissipation monitoring (QCM-D) and spectroscopic ellipsometry (SE).

QCM-D is an acoustic technique that measures the adsorption of biomolecules onto the surface of a quartz crystal that is cyclically sheared by the application of an oscillatory voltage. By intermittently switching off the driving voltage, one can measure the decay of the oscillation, which provides information on the resonance frequency f and the energy dissipation D [193]. The frequency shift upon biomolecular adsorption is proportional to the mass of the material that adsorbs to the crystal [194], while the dissipation shift reflects the mechanical properties of the adsorbed film [195, 196]. Since the shear oscillation of the sensor entrains the solvent that is trapped in the adsorbed film, the adsorbed mass sensed by QCM-D always contains a contribution of hydrodynamically coupled solvent [192]. By contrast, SE is an optical technique that measures only the mass of the adsorbed molecules themselves, because it is sensitive to the difference in the optical density between the adsorbate and the solvent [197]. By correlating QCM-D and SE measurements, it is therefore possible to determine the solvent content of the adsorbed film. This is an interesting parameter because it is sensitive to structural features such as protein clustering (in case of low coverage) or film porosity (in case of high coverage) [198–200]. Both techniques, and also a related optical technique known as reflectometry, have been used to monitor supported lipid bilayer formation [167, 168, 201] and the subsequent adsorption of several peripheral membrane proteins such as annexin A[202, 203] and ezrin [167, 204]. Until now there have been only a few studies

employing QCM-D and ellipsometry for filament-forming cytoskeletal proteins, namely actin [205, 206] and the bacterial protein FtsZ [207].

By combining QCM-D and SE, we quantitatively explore the interactions of fly septin hexamers with model biomembranes and elucidate the role of lipid composition and protein concentration. We show that septins strongly adsorb to anionic lipid membranes via electrostatic interactions. We furthermore find that septins form layers with a thickness that is limited to ~ 18 nm, corresponding to no more than 2 or 3 septin filaments packed on top of each other. This observation, taken together with the microscopy data presented in Chapter 3, suggests a model for membrane-templated septin assembly whereby septins form membrane-anchored filaments that preferentially associate with each other in the plane of the membrane while growth in thickness is limited.

4.2 Methods

4.2.1 Vesicle preparation

The lipids DOPC (18:1 1,2-dioleoyl-*sn*-glycero-3-phophocholine), DOPS (1,2-dioleoyl-*sn*-glycero-3-phospho-L-serine), and PIP_2(1,2-dioleoyl-*sn*-glycero-3-phospho-(1'-myo-inositol-4',5'-bisphosphate) (ammonium salt) were purchased from Avanti Polar Lipids (Birmingham, AL). DOPC and PS were stored at a concentration in the range of 10-25 mg/ml in chloroform, while PIP_2 was stored at a concentration of 0.5 mg/ml in a mixture of chloroform:methanol:water (volume ratio 20:9:1). Small unilamellar vesicles (SUVs) were prepared by drying mixtures of DOPC/PS (80:20 molar ratio), DOPC/PIP_2 (95:5 molar ratio) or DOPC/PS/PIP_2 (75:20:5 molar ratio) in glass vials with a gentle stream of N_2 gas and a 2 hr incubation in a vacuum chamber, followed by resuspension in vesicle buffer that was filtered (using a 0.2 μm pore size) and degassed (30 minutes). Lipid mixtures without PIP_2 were dissolved at a total concentration of 2 mg/ml in a 20 mM Tris-HCl buffer (pH 7.4) with 50 mM KCl, and 2 mM $MgCl_2$. Lipid mixtures with PIP_2 were dissolved at a total lipid concentration of 0.2 mg/ml in an acidic, 50 mM citrate buffer (composed of equal molarity trisodium citrate and citric acid mixed in a 2:3 volume ratio to obtain pH 4.8) with 50 mM KCl, and 0.1 mM ethylenediaminetetraacetic acid (EDTA), which was diluted from a stock solution (0.2-0.5M) of pH ~8 prepared in miliQ water. At this pH, the net charge on the head group of PIP_2 due to the phosphate groups is reduced (from -4 to -3) and the net charge of the silicon substrate is reduced as well [167, 208]. The reduced Coulombic repulsion promotes the formation of homogeneous and fluid bilayers. Small unilamellar vesicles (SUVs) were obtained by repeating five freeze/thaw cycles followed by sonication (30 min) with a tip sonicator with a 2 mm microtip (FisherBrand Model 120 Sonic Dismembrator). The sonicator was operated in pulsed mode (1 s on/1 s off) at 30% amplitude while the sample was kept on ice.

Afterwards the vesicle suspensions were centrifuged (15 min at 15000 *g*) to remove any titanium particles present in the solution from the sonicator tip. The suspensions were stored at 4°C for a maximum of 30 days (no PIP_2) or 7 days (with PIP_2).

Just before use in QCM-D and SE experiments, the vesicle suspensions were diluted to a total lipid concentration of 50 µg/ml in vesicle buffer containing 150 mM instead of 50 mM KCl to promote bilayer formation [209]. We used Tris buffer (20 mM Tris-HCl pH 7.4, 150 mM KCl, 2 mM $MgCl_2$) for vesicles containing PS, and citrate buffer (50 mM citrate, pH 4.8, 150 mM KCl, 0.1 mM EDTA) for vesicles containing PIP_2.

4.2.2 Septin preparation

Recombinant *Drosophila* septin hexamers (composed of His6-DSep1, DSep2 and Peanut-Strep) and two mutants thereof were expressed and purified from bacteria as detailed in Chapter 2. The first mutant, referred to as the 'WH mutant', carries two point mutations (W364A and H374D) in the Pnut subunits. These mutations are expected to block septin polymerization by impairing G-interface homodimerization of the terminal Pnut subunits on adjacent septin hexamers, based on the homology of these residues to human septins [34]. The second mutant, referred to as the 'ΔCC mutant', lacks the long C-terminal extensions on the Pnut and DSept2 subunits as well as the short C-terminal extension on DSep1. Specifically, C-terminal truncations were made at residue 416 for Pnut (539 residues), residue 308 for DSep2 (419 residues), and residue 305 for DSept1 (361 residues). The molecular weight and purity of the three septin complexes were checked on SDS-PAGE gels and the length of the complexes (as a readout of the stability of the hexameric arrangement) was checked by negative stain transmission electron microscopy (Fig. S1).

4.2.3 QCM-D

The basic idea behind QCM-D is to oscillate a quartz crystal sensor at its acoustic resonance frequency by applying an alternating current (AC) [210]. Changes in the exponential decay of the oscillation when the AC current is turned off reveal information about changes in mass and energy dissipation due to the adsorption of molecules to the sensor surface. The frequency shift Δf is proportional to the acoustic mass of the adsorbed film, while the dissipation shift ΔD provides information on its mechanical properties. In case of a thin and laterally homogeneous film, ΔD reflects the viscoelastic properties of the film [192]. In case of a film consisting of particles having a similar diameter as the film thickness (as is the case for vesicles and globular proteins), ΔD is instead related to the conformational flexibility of the attachment between the particles and the surface [192]. The frequencies are measured in odd multiples (overtones) of the resonance frequency of the piezocrystal. In our experiments, the fundamental resonance frequency was 5 MHz and data were recorded at all overtones (3 up to 13). For further analysis, we selected data obtained

at the 7^{th} overtone, in view of its stable response across all measurements. Other overtones provided qualitatively similar information and are thus not shown here. The frequency shifts were normalized according to $\Delta f = \Delta f_7/7$.

We used silica-coated QCM-D sensors (QSX303, Biolin Scientific, Sweden) that were cleaned in an aqueous solution of 2% sodium dodecyl sulfate (30 min), rinsed with ultrapure water, blow-dried with N_2 gas, and exposed to UV/ozone (BioForce Nanosciences, Ames, IA) for 30 min. The sensors were then immediately mounted in the Q-Sense flow modules of the Q-Sense E4 system (Biolin Scientific) and experiments were started within 15 min. The instrument was operated in flow mode, meaning that sample solution was continuously perfused through the measurement chamber at a rate of 20 µL/min (unless stated otherwise) with a peristaltic pump. All measurements were performed at a temperature of 23°C.

Experiments were performed by sequential incubation of the sensors with SUVs and then septins, interspersed by rinsing steps. The surface was first equilibrated with vesicle buffer before flowing in the SUV suspension. The adsorption of the SUVs onto the sensor surface and the subsequent formation of a Supported Lipid Bilayer (SLB) were monitored by measuring Δf and ΔD. Once Δf and ΔD reached stable values, indicating that the SLB was fully formed, the surface was rinsed with vesicle buffer to remove any residual SUVs, and with septin buffer to equilibrate the ionic conditions. Next, septins were diluted in septin buffer (20 mM imidazole pH 7.4, 1 mM dithiothreitol (DTT), 50 mM KCl and 2 mM $MgCl_2$) to a concentration between 6 and 60 nM and the solution was flushed in. We continued perfusion with septins for at least 60 min, after which we rinsed the sensor with septin buffer (to test the strength of septin binding), high salt (1 M KCl) septin buffer (to test whether binding can be reversed, which is expected in case the protein-membrane interaction is electrostatic in origin), and 6 M guanidinium hydrochloride (to remove all septins and test whether the membrane had been left unaffected by any septin binding and self-assembly processes). The experiments were performed at least in duplicate, unless indicated otherwise (for details on statistics, see Table S1).

4.2.4 Combined QCM-D/SE measurements

To obtain simultaneous QCM-D and SE measurements of septin adsorption on SLBs, we performed measurements with a Q-Sense E1 QCM-D system (Biolin Scientific) mounted on a spectroscopic rotating compensator ellipsometer (M2000V, J.A. Woollam Co.) that is described in detail in Ref. [211]. Spectroscopic ellipsometry measures the changes in the ellipsometric angles Δ and Ψ of polarized light upon reflection at a planar surface [212]. These angles depend on the optical properties and thickness of the investigated material. The angles were measured over a wavelength range (λ) from 380 to 1000 nm at a fixed incident angle of 65°. We used QCM-D sensors with a special coating consisting of an opaque Ti layer and transparent layers of TiO_2 and SiO_2 (QSX335, Biolin Scientific). The sensors were cleaned according to the same procedure as for standard silica-coated (QSX303) sensors.

The experiments were performed in an open fluid cell with a working volume of 2 mL [200, 211]. The solution was exchanged using a syringe needle immersed in the cell and connected to a peristaltic pump.

Prior to each measurement, the optical properties of the sensor coating were determined by performing measurements in air and in septin buffer. Next, an SUV suspension was injected into the solution at a total lipid concentration of 50 µg/ml to form an SLB on the sensor surface. Once the SLB was fully formed, as indicated by equilibration of the QCM-D signal, a concentrated septin solution (between 3 and 8 µl of a ~ 15 µM solution in low salt septin buffer) was injected into the fluid cell to obtain a final septin concentration in the range of 6 to 120 nM. We used low salt septin buffer considering that at concentrations below 200 nM septins do not form any filaments in solution (Chapter 2). Continuous stirring with a magnetic stirrer bar ensured rapid sample homogenization (i.e. within a few seconds).

Determining the optical thickness d of the SLB and of the septin film from the measured ellipsometric angles requires numerical nonlinear regression fitting because the Fresnel equations that relate Δ and Ψ to d and the refractive index $[n(\lambda)]$ are nonlinear [211]. We therefore fitted the ellipsometric data to a multilayer model using CompleteEASE software (Woollam). The sensor was modeled as a multilayer, using tabulated optical constants for the TiO_2 layer (CompleteEASE) and SiO_2 layer (Biolin Scientific) and measurements in air and buffer to obtain the optical constants of the opaque Ti layer [213].

The bulk solution was treated as a transparent and homogeneous Cauchy medium with a refractive index given by the Cauchy relation:

$$n_{\text{cauchy}}(\lambda) = A + B/\lambda^2 \tag{4.1}$$

where A and B are optical constants. For the solution, we used values (that are adjusted for the salt concentration of the buffer) of $A_{\text{sol}} = 1.323$ and $B_{\text{sol}} = 0.00322$ µm^2 [200] . Similar to previous work [200], the SLB and the adsorbed septins were treated as a single layer (Cauchy medium), to reduce the number of fitting parameters. The optical parameters associated with the SLB are its refractive index change (compared to buffer), n_{SLB}, and thickness d_{SLB}. The combined SLB+septin layer is characterized by the refractive index $n_{SLB+Septin}$ and effective thickness $d_{SLB+Septin}$. The areal mass density of the septins was determined using de Feijter's equation [197]:

$$mass_{SE} = \frac{\Delta n_{SLB+septin} * d_{SLB+septin} - \Delta n_{SLB} * d_{SLB}}{dn/dc} \tag{4.2}$$

Here dn/dc is the refractive index increment, which is around 0.18 cm^3/g for most proteins [197]. For thin films (such as we have for septins and SLBs), we expect the areal mass density thus derived to be accurate to within about 10%, even if Δn and d are 'effective' parameters, because Δn and d are covariant [200]. We treated $d_{SLB+septin}$ and the optical constant $A_{SLB+septin}$ as fitting parameters, while assuming $B_{SLB+septin} = B_{\text{sol}}$ as in previous studies [200, 214]. The two fit parameters

were varied until the Mean Squared Error (MSE) that quantifies the difference between the measured and predicted ellisometry spectra reached a minimum value. In each case, the MSE for the best fit was below 2 (between 1.3 and 1.7), which is considered an indication of a good fit [214].

4.2.5 AFM force indentation

Samples for AFM force indentation measurements were prepared on silicon wafers with a thickness of 500-550 µm (BT Electronics, Prime Silicon, Les Ulis, France), which were cut into squares of 9 × 9 mm^2. The wafer pieces were cleaned with absolute ethanol, blow-dried with N_2 gas, and treated with UV/ozone (Bioforce Nanoscience, Ames, IA) for 30 min. This treatment cleans the surface from organic contamination and makes it hydrophilic, making the surface similar to the sensor surface used in the QCM-D and SE measurements [176]. We performed one AFM experiment directly on a QCM-D sensor to test whether surface roughness plays a role. We observed that septins form filamentous structures (Fig. S2) that look comparable to those formed in the same conditions on silicon wafers (see Fig. 3.7). Substrates were glued (Picodent Twinsil glue, Wipperfurth, Germany) on a 15 mm diameter metal disc (Agar Scientific) covered with hydrophobic Fluorinated Ethylene Propylene (FEP) film protector (Bytac surface protection laminate, Sigma).

When the glue was set (after 10 min), we deposited 100 µl of SUV suspension (composed of 80% DOPC and 20% PS), which was diluted to a lipid concentration of 100 µg/ml in septin polymerization buffer supplemented with 150 mM KCl to promote vesicle fusion (20 mM imidazole (pH 7.4), 1 mM DTT, 150 mM KCl and 2 mM $MgCl_2$). After 30 min incubation, excess vesicles were washed off by replacing the liquid with 1 mL of septin polymerization buffer using a pipette, leaving 100 µl buffer on the surface to keep the SLB hydrated. We then pipetted in 50 µL of septin solution, bringing the final septin concentration to 12, 24, or 60 nM. After 15 min incubation, unbound protein was washed off with 1 mL of septin buffer. Bound septins were fixed by incubating the sample for 1 min with 2 wt% glutaraldehyde (GTA) in septin buffer and washing with septin buffer. We confirmed by AFM imaging that the morphology of the septin films is largely unaffected by the fixation and washing treatment (see Chapter 3).

Force indentation experiments were performed using a JPK NanoWizard 4 using cantilevers with a nominal spring constant of 0.06 N/m (NP-S from Bruker, nominal tip-radius = 10 nm). For samples prepared at 24 and 60 nM septin, the same tip was used, while measurements on 6 and 12 nM septin samples were performed with different tips. The actual spring constant of the tips was determined by the thermal noise method [215] and found to be within 10% of nominal values provided by the manufacturer. For each condition, 3 × 256 force-distance curves were collected over three different scan areas of 10 × 10 $µm^2$ each. Indentation measurements were performed at a constant velocity of 1 µm/s and with a maximum applied load of 2 nN.

The force-indentation curves were analyzed using JPK Data Processing software. To test the variability between different regions, we analyzed force curves from all three positions for one sample (wild type septins at 60 nM). For all other samples (wild type septins at 0, 12, 24 nM, and the ΔCC mutant at 100 nM), we analyzed one data set (256 curves). Height values were extracted from every 4^{th} curve, giving a total of 64 curves per condition (and 191 curves for the 60 nM WT septin sample). We defined the approach distance where the tip first contacted the sample as the distance where the force first reached a threshold value of 50 pN above the baseline. The force jump that is characteristic for SLB penetration [216] was used as a fingerprint to select reliable force curves. The hard wall contact of the tip with the silicon surface was defined as the distance where the force diverged.

4.3 Results

4.3.1 Septins bind charged lipid membranes through electrostatic interactions

To quantitatively analyze the binding of septins to solid-supported lipid bilayers (SLBs), we performed QCM-D experiments in which we first formed an SLB on the surface of a sensor crystal by perfusing the channel with a vesicle (SUV) suspension and next perfused with a solution of septin hexamers. To investigate the kinetics of SLB formation and septin binding, we monitored the resulting shifts in the resonance frequency Δf (which is proportional to the mass of protein plus hydrodynamically coupled solvent that is adsorbed to the sensor) and in the dissipation ΔD (which is an indicator of the mechanical properties of the adlayer). A typical QCM-D experiment to illustrate this stepwise protocol is presented in Fig. 4.1A. In the example, the bilayer is composed of 75 mole% DOPC, 5 mole% PIP_2, and 20 mole% PS. This lipid composition was chosen as a simple model of the cytoplasmic leaflet of the plasma membrane of animal cells [1].

SUV perfusion (denoted as phase 2 in Fig. 4.1A) caused immediate changes in Δf and ΔD in a two-stage process that is characteristic for the initial adsorption of intact SUVs to the sensor surface followed by SUV rupture and spreading [209, 217]. In the first stage, Δf decreased to a large negative value of ≈ -30 Hz, indicative of the addition of mass, which decreases the resonance frequency of the sensor crystal. At the same time, ΔD increased due to the large dissipation associated with the solvent trapped inside the SUVs. After reaching peak values, Δf increased to ~ -25 Hz while ΔD decreased to a small value of ~0.1 10^{-6}. These values are typical for high-quality phospholipid bilayers composed of DOPC/POPC and PIP_2 lipids [201, 217]. Subsequent rinsing with vesicle buffer to remove residual vesicles (phase 3) did not result in appreciable changes in Δf and ΔD.

After equilibrating the channel with septin buffer (phase 4), we perfused the channel with a solution of 24 nM septins (phase 5). Septin perfusion produced an

immediate decrease of Δf and a concurrent increase of ΔD, indicating that septins adsorbed onto the SLB. The changes started to level off after about 60 minutes. Perfusion with buffer (phase 6) after 60 minutes caused only small changes in Δf (on average by 11% in 39 experiments, see Fig. S4), suggesting that septins strongly adsorb to the membrane. To test whether septin binding is mediated by electrostatic interactions, we next rinsed the surface with a high-salt buffer containing 1 M KCl (phase 7) followed by septin buffer (phase 8). This released nearly all the protein from the surface (on average 97% across 39 experiments, see Fig. S4). To test whether septin binding affects membrane integrity, we finally rinsed the surface with a 6 M solution of the denaturing agent guanidinium chloride (phase 9) followed by septin buffer (phase 10). Now Δf returned to that of the intact bilayer before septin injection, indicating that septin adsorption does not affect membrane integrity. We conclude that septins strongly bind to lipid bilayers containing both 5% PIP_2 and 20% PS and that binding is dominated by electrostatic interactions. We indeed did not observe any adhesion of septins to pure DOPC membranes (Fig. S3), indicating that septin binding requires the presence of negatively charged lipids.

To further test the dependence of septin binding on membrane composition, we repeated the QCM-D experiments at a fixed septin concentration of 60 nM in the presence of membranes containing either 20% PS or 5% PIP_2 (Fig. 4.1B). Note that we plotted -Δf on the y-axis and subtracted the bilayer signal, and we shifted the curves along the time axis such that time zero corresponds to the start of septin perfusion. Although the variability between duplicate experiments was rather large, we observed a clear difference between the initial adsorption rate on membranes containing both 20% PS and 5% PIP_2 compared to membranes containing either lipid alone. The initial (peak) adsorption rate was nearly 2-fold higher on membranes containing both lipids and also the final amount of adsorbed septins was higher than on the membranes containing only a single charged lipid species.

Fig. 4.1C summarizes the dependence of septin adsorption on membrane composition by comparing the values for -Δf measured after 60 min: -Δf was highest when both lipids were present, intermediate in case only 20% PS was present, and lowest in case only 5% PIP_2 was present. To interpret these findings, we note that PIP_2 has a higher negative charge per molecule than PS. PIP_2 has a net charge of about -4 due to the phosphate groups, while PS carries two negative charges and one positive charge, which give a net charge of -1 at pH 7. Also, LUVs containing 5% PIP_2 are slightly less negatively charged than those containing 20% PS [167, 169–172]. Therefore, our findings suggest that the total negative surface charge of the membrane governs septin adsorption, indicating that the septin-membrane interaction is primarily electrostatic in origin.

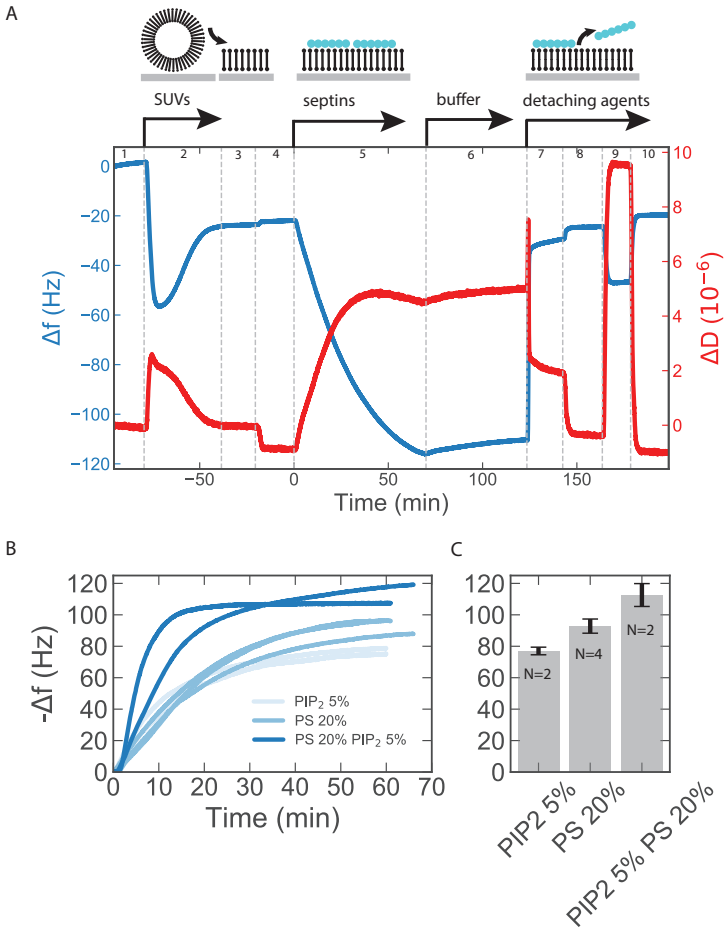

Figure 4.1: QCM-D measurements of septin adsorption on and desorption from DOPC bilayers containing anionic lipids (5% PIP_2 and 20% PS) show that septins bind through electrostatic interactions. A) Time-dependence of the frequency Δf and dissipation ΔD shifts upon sequential perfusion of the QCM-D sensor crystal with: 1) vesicle buffer to equilibrate the sensor, 2) SUVs in vesicle buffer (50 µg/mL lipids) to form an SLB, 3) vesicle buffer to wash out residual SUVs, 4) septin buffer, 5) septin hexamers in septin buffer (24 nM), 6) septin buffer , 7) high salt septin buffer (1 M KCl), 8) low salt septin buffer (50 mM KCl), 9) 6 M GnHCl, and 10) low salt septin buffer. B) Adsorption kinetics for septins (60 nM) on DOPC bilayers containing different anionic lipids (see legend) expressed in terms of -Δf, which is proportional to the areal mass density of septins, including hydrodynamically coupled solvent. The baseline -Δf shift after SLB formation was subtracted off. Duplicate or triplicate measurements are shown for each condition. C) Dependence of -Δf (measured after an incubation time of 1 hour) on bilayer composition. Error bars represent standard deviations based on N experiments per data point (see legend).

4.3.2 Mass transport limits the rate of septin adsorption

We noted that septin adsorption was rather slow, often not reaching saturation even after 60 minutes. This observation suggests that the adsorption process may be limited by the diffusion rate of the septin hexamers, which are indeed expected to diffuse slowly on account of their large molecular weight (307 kDa). To test this hypothesis, we performed QCM-D measurements of septin binding (at a concentration of 20 nM) to membranes composed of DOPC and 5% PIP_2 for a wide range of flow rates between 5 and 100 µl/min. In case mass transport limits the adsorption rate, the adsorption rate should be linearly proportional to the cube root of the flow rate given the geometry of the flow chamber [218]. By contrast, we expect no dependence on flow rate in case protein binding limits the adsorption rate.

The time traces for the increase of $-\Delta$f upon septin perfusion show a clear dependence on flow rate, as shown in Fig. 4.2A. To determine the septin adsorption rate, we computed the time derivatives of the -Δf data (smoothed over 10 frames) for each individual experiment. As shown in Fig. 4.2B, each curve shows a clear maximum, which we take as the peak adsorption rate. As shown in Fig. 4.2C, the peak adsorption rate increases approximately linearly with the cube root of the flow rate, consistent with mass transport (by flow and diffusion) of the septins to the bilayer being rate-limiting for bilayers containing both PS and PIP_2. However, we note that the slower adsorption on membranes containing only one charged lipid species (20% PS or 5% PIP_2) compared to membranes containing both lipids (see Fig. 4.1B) suggests that in those cases surface kinetics influence the rate of adsorption. The adsorption rate may for instance be limited by the local accumulation of negative charges in case of these less highly charged membranes.

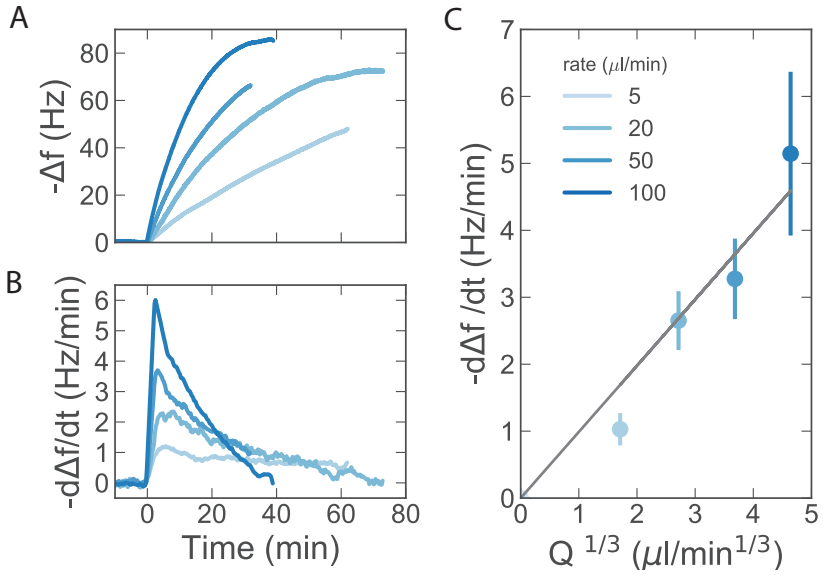

Figure 4.2: QCM-D measurements at different flow rates show that mass transport limits the kinetics of septin adsorption to lipid bilayers. Experiments were performed with 20 nM septins on lipid bilayers composed of 95% DOPC and 5% PIP_2. (A) Time dependence of the frequency shift for different flow rates Q (see legend) and (B) corresponding first derivatives, smoothened over 10 frames. (C) Dependence of the peak adsorption rate on $Q^{1/3}$. The grey line indicates the linear dependence with a fixed origin at (0,0) expected when mass transport is rate-limiting. Error bars represent standard deviations of the mean, based on 2 experiments per condition.

4.3.3 Dependence of septin adsorption on septin concentration

To test how septin adsorption to anionic lipid bilayers depends on septin concentration, we performed QCM-D measurements for four different septin concentrations (6, 12, 24 and 60 nM) on membranes with different lipid compositions. As shown in Fig. 4.3A, the rate of adsorption on DOPC membranes doped with 5% PIP_2 and 20% PS, as quantified through the time dependence of -Δf, increases with increasing septin concentration. Unexpectedly there is quite some variability between duplicate measurements, which could reflect either inaccuracies in the concentration or the influence of additional factors on the adsorption kinetics. The acoustic areal mass density, as quantified by $-\Delta f$ measured after 60 minutes, increases sublinearly with septin concentration on membranes of all compositions, going from 20 Hz at 6 nM septin to 110 Hz at 60 nM septin (Fig. 4.3B). Septins could be desorbed in all cases by rinsing with a high salt (1 M) buffer, although the fraction that remained bound showed a trend of being slightly higher when the amount of adsorbed septins was larger (Fig. S5).

Due to the slow kinetics of septin adsorption, the QCM-D measurements performed in flow mode do not provide equilibrium data for septin adsorption. Moreover, the QCM-D measurements do not provide a direct measure of the adsorbed amount

of protein because they include hydrodynamically coupled solvent. To obtain equilibrium measurements of septin adsorption and to eliminate any solvent contribution, we therefore performed coupled QCM-D/SE measurements in an open chamber where the solution was stirred.

Fig. 4.3C shows typical time traces of the areal mass density measured with SE at different septin concentrations and on membranes composed of DOPC and 20% PS. When we compare these time traces with the time dependent increase in the acoustic areal mass density measured with QCM-D in the presence of flow (Fig. 4.3A), we clearly see that stirring enhances the kinetics of septin adsorption. The areal mass density measured by SE increases with time and reaches saturation within about 60 minutes. This observation confirms our earlier conclusion that mass transport limits the rate of septin adsorption. When we plot the optical mass in steady-state as a function of septin concentration, we observe a linear dependence (Fig. 4.3D).

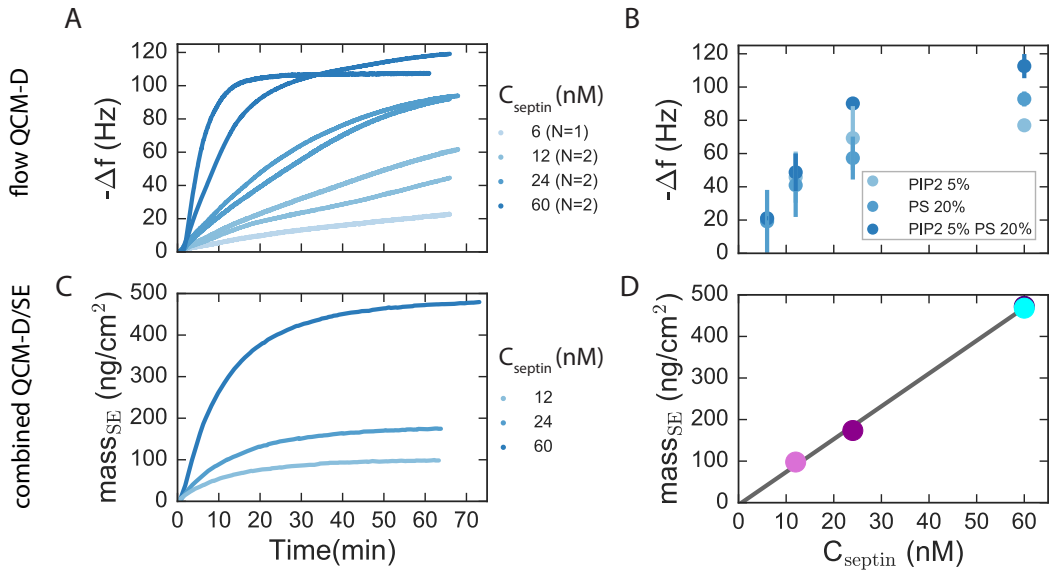

Figure 4.3: Dependence of septin adsorption on septin concentration measured by QCM-D operated in flow mode and by SE for stirred solutions. (A) QCM-D measurement of the adsorption kinetics for septins at different concentrations (see legend) on DOPC membranes doped with 20% DOPS and 5% PIP_2. Duplicate measurements are shown for each condition, except for the 6 nM septin condition. (B) Dependence of the acoustic areal mass density ($-\Delta f$) measured after 60 min on septin concentration for different membrane compositions (see legend). Averages and error bars correspond to different numbers of experiments per condition (see Table S1). (C) Time dependence of the areal mass density measured by SE at different septin concentrations (see legend) on membranes composed of DOPC and 20% DOPS. (D) Steady-state areal mass density as a function of the solution concentration of septins, shown with a linear fit. Note there are 2 data points that nearly perfectly coincide at 60 nM.

4.3.4 Impact of septin polymerization on membrane binding

We showed in Chapter 3 by direct imaging that fly septin hexamers form filaments on anionic lipid bilayers. It was recently shown in the context of yeast septins that filament formation strongly enhances the affinity of septins for lipid bilayers [144]. To test whether this is also true for fly septins, we investigated membrane binding of the ΔCC truncation mutant septin. The C-terminal extensions that are predicted to form coiled coils necessary for filament pairing were removed from all three subunits (Pnut, DSept2, and DSep1). Transmission electron microscopy images indeed showed that the ΔCC mutant only forms short rods with lengths of ~48 nm (corresponding to dimers of hexamers) or 60 nm (trimers) in solution (Fig. S1E). Interestingly, we saw that the ΔCC mutant still forms filaments on negatively charged lipid monolayers (Fig. S6). However, unlike filaments formed by full length septins, these filaments are not paired and they are much more closely spaced, with a

center-to-center distance of ~4 nm. QCM-D measurements showed that the ΔCC septin hexamers exhibit markedly less binding on DOPC/20% PS bilayers compared to the WT septins (Fig. 4.4C). We could only observe appreciable binding when the septin concentration was raised to 60 or 120 nM, and even then the $-\Delta f$ values remained less than 20 Hz. We conclude that septin-septin interactions mediated by the coiled coils are important for membrane binding.

As a further test of the importance of filament formation for membrane binding, we also performed QCM-D measurements on septin hexamers carrying two WH point mutations on the Pnut subunits. The Pnut subunits have traditionally been thought to form the terminal subunits on the basis of the homology between fly and human (hSep2, hSep6, hSep7) septin hexamers, for which a crystal structure is available [34]. If this is true, the WH mutations should abolish polymerization by impairing end-to-end association of septin hexamers, since these two conserved residues are localized at the interface between the Pnut subunits of adjoining hexamers [34]. However, two recent preprints showed evidence for an alternative subunit arrangement for human septin hexamers, which would imply that the Pnut subunits are actually in the center [35, 36]. In this case, the WH mutations should destabilize hexamers and also abolish polymerization. TEM images indeed showed that the WH septin mutant did not form any higher order structures in low salt Tris buffer (Fig. S1F). QCM-D measurements showed that the WH septin hexamers, like ΔCC septin hexamers, bound less to DOPC/20% PS bilayers compared to the WT septins (Fig. 4.4B). We conclude that septin polymerization is important for enhancing membrane binding.

To summarize these findings, we compare the $-\Delta f$ values after a 60 min incubation time for WT septins and the two mutants in Fig. 4.4D. Both mutants exhibited markedly less binding compared to WT septins on membranes of different compositions (DOPC mixed with 5% PIP2, 20% PS, or a combination thereof).

We note that high-salt (1 M KCl) buffer caused only partial (20-40 %) desorption of the two mutant septins (see Fig. S5), suggesting that other interactions besides electrostatic interactions may contribute to membrane binding or that some protein aggregates may be present that stick to the membrane. Negative stain EM measurements of the two mutants on lipid monolayers showed some binding in case of ΔCC septins but did not show binding of the WH mutant (see Fig. S7). Rinsing with GnHCl did return the frequency shift to that of the bare bilayer, meaning that the mutants did not influence bilayer integrity (Fig. S5).

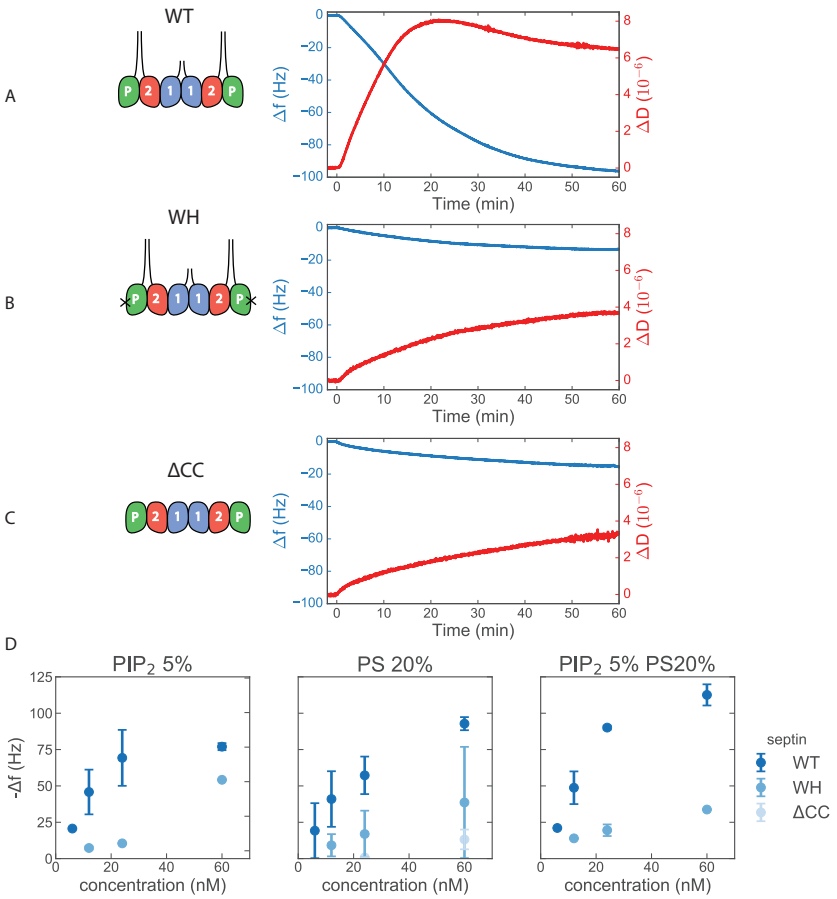

Figure 4.4: QCM-D measurements show that non-polymerizing septin mutants bind less to anionic lipid membranes compared to wild type septins. Schematics of the oligomer structure (left) and example QCM-D measurements of Δf and ΔD for (A) wild type septin hexamers (60 nM), (B) the WH mutant with a W364A and H374D mutation in the Pnut subunits (here drawn as terminal, although they may alternatively be central) that abrogates end-to-end assembly (60 nM), and (C) the ΔCC septin truncation mutant that lacks the C-terminal extensions that are thought to be necessary for filament pairing (120 nM). The septins were incubated with 80% DOPC/20% DOPS bilayers. (D) Adsorbed amounts of septins after 60 min incubation for WT septins and the two mutants (see legend) as a function of septin concentration and for three different lipid compositions, (left) DOPC with 5% PIP_2, (middle) DOPC with 20% PS, and (right) DOPC with 5% PIP_2 and 20% PS. Note that the ΔCC mutant was only tested on membranes containing 20% PS. Averages and standard deviations correspond to different numbers of experiments in each condition (see Table S2).

4.3.5 Septin organization revealed through analysis of hydrodynamically trapped water content

By comparing the acoustic mass measured by QCM-D with the optical mass measured by SE, we can determine the amount of solvent that is hydrodynamically coupled to the protein film. Studies of various membrane-binding proteins have shown that the amount of hydrodynamically coupled solvent depends on the structure of the protein film. By plotting the time-dependent acoustic mass expressed in terms of $-\Delta$f (Fig. 4.5A) as a function of the optical mass measured at the same time (Fig. 4.5B), we obtain a calibration curve that relates the QCM-D mass to the molecular coverage of the membranes. Fig. 4.5B shows that the correlation between the acoustic mass (i.e. $-\Delta f$) and the optical mass (mass_{SE}) is identical for different septin concentrations between 12 and 60 nM. Data obtained for the non-polymerizing WH septin mutant also fall onto the same calibration curve (Fig. 4.5B, cyan curve).

Although the areal mass density measured by QCM-D systematically increases with the areal mass density measured by ellipsometry, the relation between the two measurements is not exactly linear. Apparently the fraction of hydrodynamically coupled solvent contributing to the QCM-D mass changes with time. To probe this time dependence more directly, we define the mass fraction of hydrodynamically coupled solvent as [200]:

$$H = 1 - mass_{\text{SE}}/mass_{\text{QCM-D}}, \tag{4.3}$$

Note that $mass_{\text{QCM-D}}$ was determined by the Sauerbrey relation. As shown in Fig. 4.5C, H starts out high, at a value in the range of 80 to 95%, and progressively decreases with time, to reach a final value of 80% once septin adsorption reaches saturation. Interestingly, the mass fraction of hydrodynamically coupled solvent is higher than typical values of 50-60% observed for dense monolayers of globular membrane-binding proteins such as streptavidin [219] and annexin A5 and cholera toxin [198, 200]. This could be an effect associated with the filamentous network structure of the septin films observed by AFM imaging, which presents large pores that likely trap a large amount of water that is dragged along with the septins as the sensor oscillates (c.f. Chapter 3).

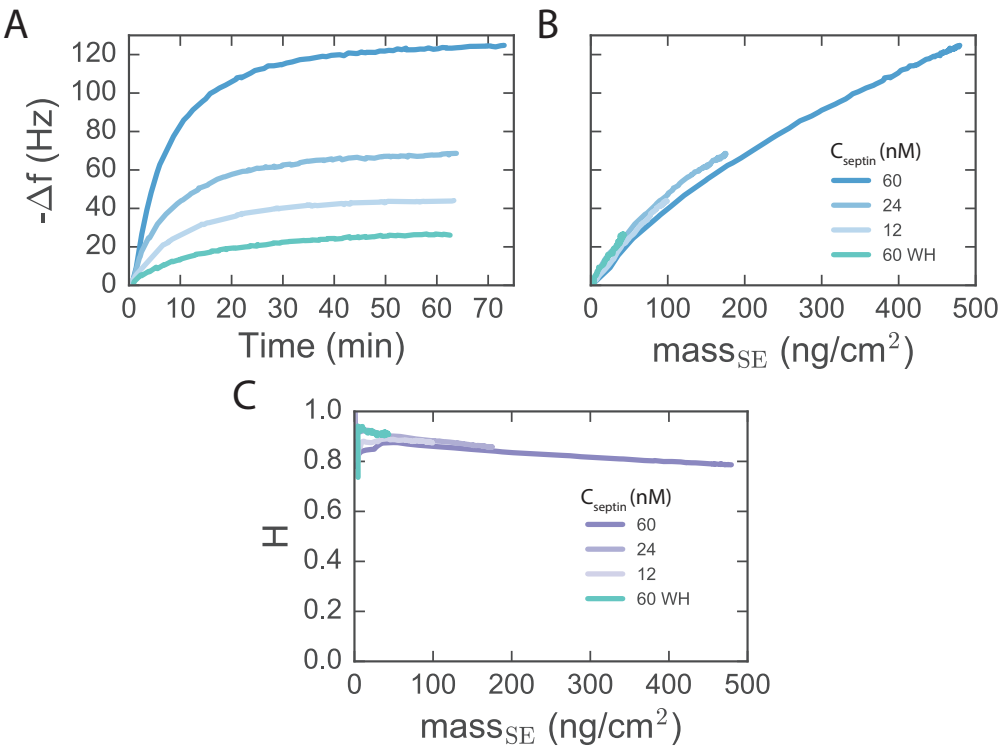

Figure 4.5: Combined SE and QCM-D measurements of septin adsorption to 80% DOPC/20% PS bilayers reveal a large mass fraction of hydrodynamically coupled solvent. (A) Frequency shift as a function of time and the concurrent (B) areal mass density measured by SE (same experiment as shown in Fig. 3C) for wild type septins and for the WH mutant. The correlation between the acoustic mass measured by QCM-D and the optical mass measured by SE falls on a single master curve for wild type septins at different concentrations (12, 24, or 60 nM) and for the WH-mutant at 60 nM (see legend). (C) Mass fraction of hydrodynamically coupled solvent as a function of the areal mass of adsorbed septins. Note that the data at low coverage are affected by measurement noise.

4.3.6 Mechanical properties of the septin films

In the QCM-D measurements, changes in Δf upon septin adsorption were always accompanied by changes in the dissipation shift ΔD. When we incubated membranes of different compositions with a high concentration (60 nM) of septins, we typically observed a quick rise of ΔD upon septin addition, a pronounced peak, and then an evolution towards a steady-state value (Fig. 4.6A). Such transient peaks have also been observed for various globular proteins [196] and have been attributed to the presence of soft linkage regions that connect the proteins to the surface or to each other [196]. In both these cases, the dissipation is caused by rocking motions of globular domains pivoting around the soft linker regions and the concomitant solvent flow. Such rocking motions are effectively reduced at higher coverage owing to hydrodynamic coupling between the adsorbed proteins, thus reducing dissipation.

Our data therefore suggest that the septin organization on the surface contains soft linkage regions. Similar observations were made when we incubated membranes with different concentrations of septins (Fig. 4.6B).

To compare the mechanical properties of the septin films to those of other membrane-binding proteins, we calculate a softness parameter, defined as the ratio $\Delta D/-\Delta$f. In the limit of thin films such as polymer brushes [192, 214], this parameter is proportional to the elastic compliance of the film. In case of films composed of discrete nanoscale objects, the $\Delta D/-\Delta$f ratio has no simple equivalent rheological parameter. However, it remains a reporter of mechanically compliant elements within the film. As shown in Fig. 4.6C and D, the softness gradually decreased with increasing coverage (-Δf) for all septin concentrations and membrane compositions that were tested. This is consistent with prior observations for other discrete nanosized objects such as colloidal particles, SUVs, virus particles, and spherical proteins [196, 198, 220]. Simulations of discrete particles adsorbed through narrow linkers or contact zones predicted a linear decrease of softness with coverage [196, 220] due to mechanical stabilization of the film by hydrodynamic interactions between neighboring particles. Interestingly, septin adsorption on membranes containing both PS and PIP_2 produced less soft films than membranes containing either lipid alone, especially under conditions of low coverage. This observation suggests that the fibril morphology may change as a function of lipid charge density. A high lipid charge density might for instance promote alignment of membrane-bound filaments.

The $\Delta D/-\Delta$f ratio of the septin films after 60 min incubation ranged from 0.2 × 10^{-6}/Hz for the sparsest films to 0.05 × 10^{-6}/Hz for the densest films. To interpret these numbers, it is instructive to compare them to measurements on other peripheral membrane-binding proteins. The smallest $\Delta D/-\Delta$f ratios have been reported for the pentameric B-subunit of cholera toxin (0.05 × 10^{-6}/Hz [200]) and for annexin (0.01 × 10^{-6}/Hz [203]). Both proteins are compact and flat, and they make a firm contact with the membrane. A larger softness was observed for a PIP_2-binding fragment of ezrin (0.125 × 10^{-6}/Hz [204]), which has a more narrow and flexible contact with the membrane. The softness we find for the densest septin films falls in between these two scenarios.

To test whether septin polymerization affects the mechanical properties of the septin films, we compare the dissipation shift for wild type septins with that of the non-polymerizing mutants. As shown in Fig. 4.7A, ΔD/-Δf for the ΔCC truncation mutant starts out at a similar level of 0.2 × 10^{-6}/Hz as for wild type septins. ΔD/-Δf for the WH mutant is slightly higher, at 0.3 × 10^{-6}/Hz. When we plot the ΔD(t)/-Δf ratio as a function of -Δf, we find similar ratios for the mutants and wild type septins at a given coverage. This holds true for all septin concentrations and lipid compositions investigated, as shown in Fig. 4.7C, where we compare the softness of wild type and mutant septin films 60 min after the initiation of septin perfusion. Apparently the softness is primarily determined by the surface coverage. Therefore, the different time dependencies of the softness for mutant versus wild type septins

during septin adsorption can be explained by the lower surface coverage reached by the mutant septins. Note that septin films on PS+PIP_2 membranes consistently show lower values for the softness parameter than septin films on membranes containing either charged lipid alone, consistent with the data shown in Fig. 4.6.

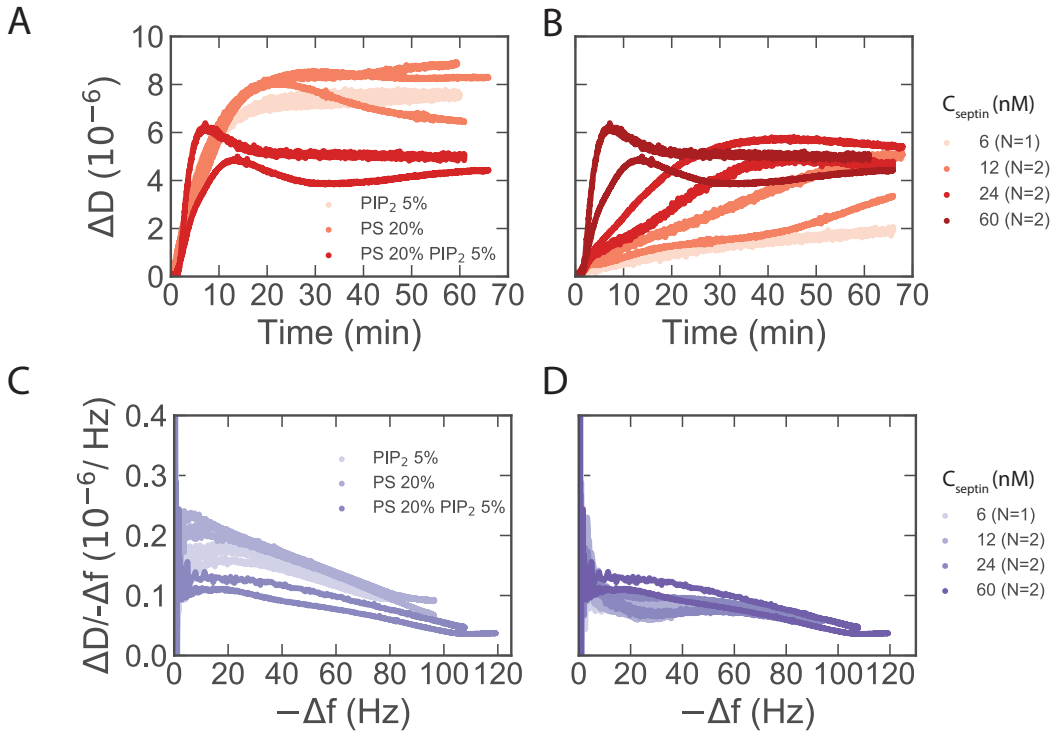

Figure 4.6: QCM-D analysis of the mechanical properties of membrane-bound septin films. (A) Time traces of the dissipation shift measured after septin addition (at time 0) to bilayers with different lipid compositions (see legend) at a fixed septin concentration of 60 nM. Measurements were performed in duplicate or triplicate. Corresponding frequency shift traces are shown in Fig. 4.1B. (B) Same as (A), now showing time traces obtained at different septin concentrations (see legend) on DOPC/20% PS bilayers. Measurements were performed in duplicate, except for the 6 nM condition. Corresponding frequency shift traces are shown in Fig. 4.3A. (C) By combining ΔD data with the frequency shifts measured at the same time (shown in Fig. 1B), we find that the softness parameter ΔD /$-\Delta$f decreases linearly with $-\Delta$f. (D) Same as (B), for different septin concentrations, derived from dissipation data in panel B combined with frequency data in Fig. 3A.

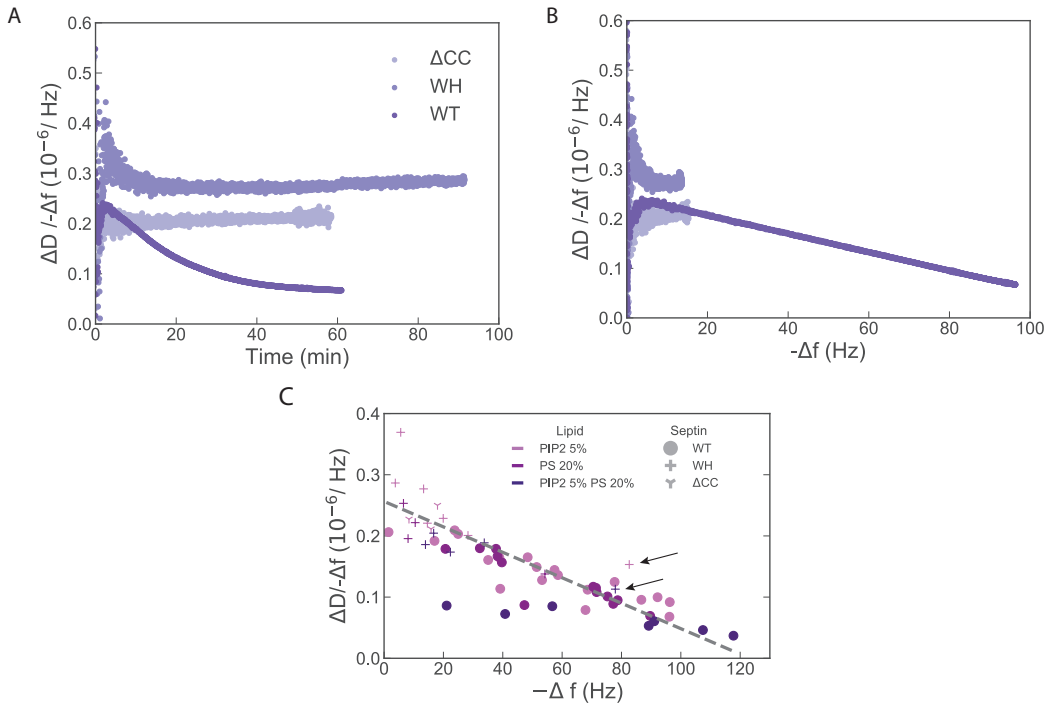

Figure 4.7: Comparison between the mechanical properties of membrane-bound films of wild type septins versus two non-polymerizing mutants. (A) Time traces of the ΔD/-Δf ratio for wild type (WT) septins and the WH and ΔCC mutants. Corresponding time traces of -Δf are shown in Fig. 4.4(A-C). (B) Parametric plot for the time-dependent softness parameter as a function of the adsorbed amount (expressed as -Δf), showing that for the same adsorbed amount, the three septin variants exhibit a similar softness. (C) Parametric plot of the softness measured after 60 minutes as a function of adsorbed amount for different septins and for different membrane compositions (see legend). The data mostly fall onto a single linear master curve (dashed grey line). Note that septin films on PS+PIP_2 membranes consistently show lower softness parameter values than the corresponding films on membranes containing either charged lipid alone, consistent with the data shown in Fig. 4.6. The arrows point to two measurements of WH mutants showing higher-than-usual adsorption.

4.3.7 Thickness of the membrane-bound septin films

QCM-D measurements can in principle provide information on the thickness of the adsorbed septin films. Provided that the septin layer is sufficiently uniform, dense and rigid, the Sauerbrey equation relates the frequency shift to the areal mass density of the film, $m_{\text{QCM-D}}$, which equals the layer density $\rho_{\text{QCM-D}}$ times the layer thickness $d_{\text{QCM-D}}$ [194]:

$$\Delta f_n = -n/C \times m_{QCM-D} = -n/C \times \rho_{QCM-D} \times d_{QCM-D}. \tag{4.4}$$

The mass sensitivity constant C is 18 ng/cm^2/Hz for QCM-D sensors with a resonance frequency of 5 MHz [192] and the mass density for protein films is 1.1 g/cm^3 to a

good approximation, considering that the film consists of proteins (ρ = 1.4 g/cm^3) and more than 50% solvent (ρ = 1.0 g/cm^3) [192]. The film thickness $d_{\text{QCM-D}}$ is therefore proportional to Δf with a proportionality constant of 6.1 Hz/nm.

We thus estimate that the film thickness for wild type septins ranges from 3 nm at a concentration of 6 nM to 18 nm at 60 nM. The thickness for the most dilute samples is consistent with a single septin monolayer, given that septins have a diameter of 4 nm. However, these values should be interpreted with caution, because the Sauerbrey equation is valid only in case of films that are uniform, dense and rigid. Based on the AFM images shown in Figure 3, only the films formed at the highest concentration of 60 nM are likely sufficiently dense to satisfy this criterion. For the ΔCC mutant, the highest −Δf values were around 20 Hz, consistent with a single septin monolayer. For the WH mutant, 6 out of 16 −Δf values exceeded 20 Hz. Higher coverages for WH mutant correlated with higher septin concentrations, but did not show any correlation with the lipid bilayer composition.

Given the uncertainty associated with the thickness values inferred from QCM-D measurements, we decided to use AFM force-indentation to obtain a more direct and model-independent measure of the thickness of the septin films. Fig. 4.8A shows typical force-indentation curves for a bare bilayer and a bilayer incubated with 24 nM septins. Both curves are shifted along the x-axis such that the hard-wall contact with the substrate (evidenced by a divergence of the force) is located at a distance of 0 nm. In both cases we observe a clear signature of SLB penetration by the AFM tip in the form of a peak in the force (indicated by the arrow) [216]. The peak typically occurred at a distance of about 4 nm from hard-wall contact, consistent with the expected thickness of the lipid bilayer [201]. We defined the first point of contact of the AFM tip with the sample as the height where the force recorded during the approach of the sample first reached 50 pN (horizontal dashed line in Fig. 4.8A). For the two selected examples shown here, contact was made at a distance of 6 nm in case of the bare bilayer (orange curve) and 12 nm in the presence of 24 nM septins (purple curve).

Histograms of the total (SLB + septin) film heights measured at different septin concentrations are shown in Fig. 4.8B. The peak was centered around a height ranging between 5.0 and 6.1 nm from the substrate, consistent with bilayer thickness values between 4 and 6 nm observed in prior nanoindentation studies [201, 221]. In the presence of septins, we still observe the membrane peak. This is to be expected considering that septins cover only a fraction of the surface. With increasing septin concentration, we observe more and more events where the contact distance is larger than 6 nm, indicating the presence of adsorbed protein. At a septin concentration of 24 nM, we observed apparent heights ranging up to 12 nm, which implies a maximum septin film height of 6 nm. This height is consistent with a monolayer of septins. At a septin concentration of 60 nM, we observed apparent heights ranging up to 20 nm, corresponding to a maximum septin film height of 14 nm. Both heights are quite comparable to the average film heights of 4 and 18 nm, respectively, determined by QCM-D. The heights measured by AFM force indentation are also quite consistent

with the heights inferred from AFM topography images of the same regions shown in Chapter 3. For the ΔCC truncation mutant (bottom-right panel in Fig.4.8B) we could not detect any protein on the membrane by AFM force indentation. Also this finding is qualitatively consistent with QCM-D, which showed little adsorption for this mutant.

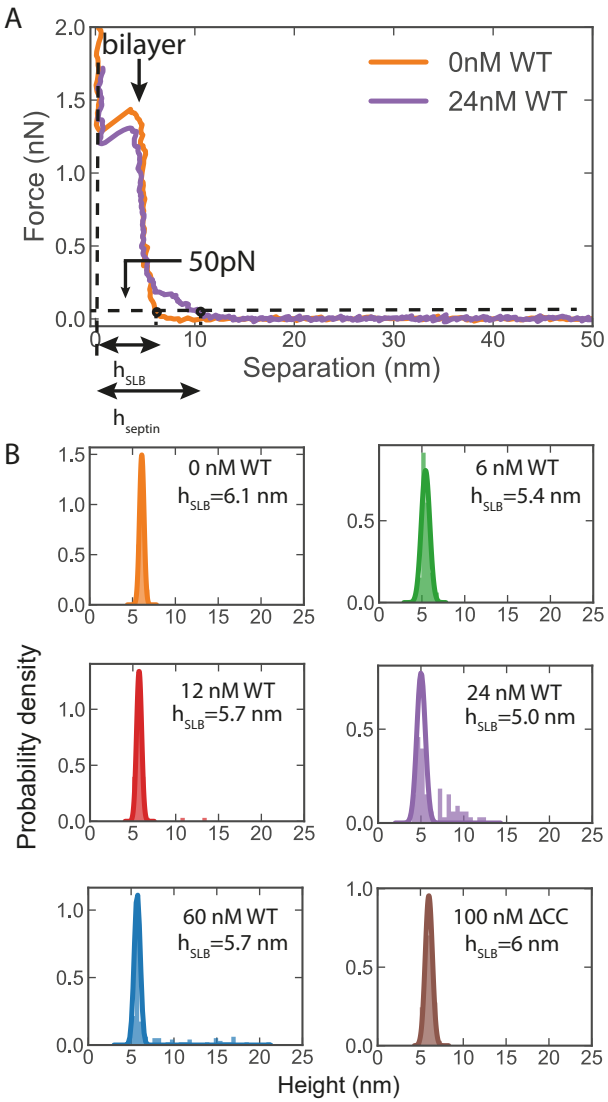

Figure 4.8: Determination of septin film thickness by AFM nanoindentation measurements. (A) Example force-indentation curves for a bare SLB (orange) and for an SLB incubated with wild type septins (60 nM). The arrow indicates force peaks caused by bilayer penetration. The curves were shifted along the x-axis such that substrate contact (where the force diverges) is located at a height of 0 nm. The height of the SLB and any adsorbed septin is defined as the approach distance where the force first reaches a threshold value of 50 pN (horizontal dashed curve). (B) Histograms showing film height distributions for wild type septins at different concentrations (6-60 nM) and for the ΔCC mutant (100 nM) (see legends). The histograms are normalized such that the area under the histogram equals 1 and the bin size is 0.5 nm. Each histogram corresponds to 64 measurements, except for the 60 nM sample, where the histogram is based on 191 curves. Lines represent Gaussian fits to the membrane peaks; the peak positions h_{SLB} are specified in the legends.

4.4 Discussion

4.4.1 Comparison of QCM-D and SE data with AFM measurements

We showed that QCM-D and SE provide complementary insights in the adsorption of septins to solid-supported lipid bilayers. The QCM-D measurements revealed that septins only interact with SLBs in the presence of anionic lipids (PS or PIP_2) and that membrane binding is dominated by electrostatic interactions. We furthermore found that the rate of septin adsorption is limited by mass transport since it depended on the flow rate. However, the composition of the bilayers also impacted the adsorption kinetics, suggesting that other factors such as membrane remodeling also play a role. At the highest septin concentration investigated (60 nM), the QCM-D measurements indicate an average film thickness of about 18 nm (consistent with AFM indentation measurements, showing a characteristic thickness of 12-17 nm). This thickness is clearly larger than the thickness of a single septin hexamer (4 nm), indicating that septins form multilayers. However, upon prolonged perfusion with septins the films eventually reached a constant thickness, suggesting the presence of a mechanism that limits film growth. For sparse films formed at low septin concentrations and in case of non-polymerizing septin mutants we could not reliably determine the film thickness by QCM-D measurements. AFM imaging under these conditions showed that (wild type) septins form filaments with a thickness of 3 to 4 nm (Chapter 3). Finally, the mechanical properties of the septin films inferred from the dissipation shifts are consistent with the presence of a rather rigid septin film with limited conformational flexibility in the septin-membrane attachment and/or septin-septin connections.

The SE measurements showed that septin binding increases linearly with septin concentration in the range of 6 to 60 nM. By correlating QCM-D and SE measurements, we found that the septin films carry a large mass fraction (~80%) of hydrodynamically coupled water. This finding is consistent with the meshwork-like structure of the septin layers we observed by AFM (Chapter 3), which likely traps large amounts of water in the pores. The septin films are relatively rigid, with a softness parameter measured by QCM-D that is in between that of rigid and conformally attached proteins like annexin A5 [202, 203] and that of flexibly adsorbed globular proteins such as ezrin [167, 204]. The multivalent interactions of septin filaments with the membrane probably provide a tight membrane anchor with little conformational freedom, and the lateral association of septin filaments probably makes also the film itself rather rigid. Consistent with this interpretation, the softness decreases approximately linearly with increasing surface coverage.

How consistent are the QCM-D and SE measurements with information on the mass density and thickness of the membrane-bound septin films from AFM imaging (Chapter 3) and nanoindentation measurements? To answer this question, we first consider the various measurements we obtained of the thickness of the septin films.

As summarized in Table4.1, we have on the one hand QCM-D and SE measurements providing the ensemble-averaged film thickness, and on the other hand spatially resolved information from AFM imaging and nanoindentation on the range of heights. It should be noted, however, that the combined QCM-D and SE measurements were performed on septin films formed after 60 minutes of incubation while stirring, whereas the AFM measurements were performed on septin films formed after 15 min of incubation in the absence of stirring or flow. With QCM-D, we find average film heights ranging from 4 nm at 6 nM septins to 18 nm at 60 nM septins, with the caveat that these values are inferred using the Sauerbrey equation. With AFM imaging, we also find heights of ~4 nm at low septin concentrations (12, 24 nM) and we observe thicker films with an average height of 12 nm at high septin concentration (60 nM). Both AFM imaging and indentation data show maximum film heights of ~14-17 nm at 60 nM. We note that these values may underestimate the actual geometrical height because the tip can potentially indent or otherwise disturb the soft septin layer. Nevertheless, the heights measured by QCM-D and SE are in good agreement with the heights obtained by AFM.

As a further test of the consistency between QCM-D/SE measurements on the one hand and AFM measurements on the other hand, we consider the areal mass density of septins. By analyzing the distribution of pixel heights observed in AFM images, we obtain an estimate of the fraction of area covered by septins and the typical septin film height, and thus the protein volume per unit area (see Chapter 3). Assuming an average protein density of 1.1 g/cm^3, we thus obtain the areal mass density. We can compare this with the areal mass density measured by SE. As summarized in Table4.1, the areal mass density inferred from AFM images and QCM-D is respectively ~5-fold and ~8-fold higher than the areal mass density obtained by SE. Considering the uncertainties associated with both types of measurements (tip convolution effects for AFM and hydrodynamic coupling of solvent for QCM-D), we consider this to be reasonably good agreement.

4.4.2 Towards a model for membrane-templated septin assembly

What do the QCM-D and SE measurements tell us about the organisation of septins on the membrane? As discussed above, both surface analytical techniques provide measures of the septin film thickness and density that are consistent with the AFM and EM images presented in Chapter 3. In that chapter, we proposed a model whereby septin hexamers adsorb to the membrane and form paired filaments through coiled-coil association. We proposed that a certain fraction of coiled coils is not used in pairing and is free to associate with neighboring septin hexamers or filaments. Because of the large flexibility of the coiled coils, the association between neighboring septins can probably occur both in-plane and out-of-plane.

The observation from QCM-D and SE measurements that the thickness of the films reaches a limiting value over time suggests that in-plane association is

more likely than out-of-plane association. This could have to do with the initial rapid adsorption of septins all over the membrane. Moreover, there could be a cooperativity effect from the simultaneous interaction of many septin hexamer units with the membrane. The large amount of hydrodynamically coupled water seen from correlated QCM-D/SE measurements as well as the large softness of the septin films observed by QCM-D are both consistent with the presence of septins that extend somewhat into the third dimension rather than lying perfectly flat against the membrane. We speculate that for each subsequent layer, there remain fewer and fewer coiled coil (or other) interacting groups on top that are available for further septin layer deposition.

Acknowledgements

I greatly thank the co-authors of this thesis chapter, Fouzia Bano & Ralf Richter (Leeds University), Manos Mavrakis (Institut Fresnel, Marseille), and Aurélie Bertin (Institut Curie, Paris) for sharing expertise, materials, data and insightful discussions. I thank Stef van der Meulen for introducing me to QCM-D measurements, and I thank the Bionanoscience Department at the TU Delft for their kind hospitality. I thank Nesrine Aissaoui and Leire Díaz Ventura (CIC biomaGUNE, Donostia-San Sebastián) for teaching me the technical details of operating the QCM-D and Ellipsometry instruments. I thank Marjolein Kuit-Vinkenoog for protein purification. For critical reading of the manuscript, I thank Manos Mavrakis, Aurélie Bertin, Ralf Richter and Gerard Castro Linares.

	AFM		
C_{septin} (nM)	height (nm) (imaging)	max height (nm) (indentation)	areal mass density (ng/cm^2)
12 nM	3.3 ± 1	-	
24 nM	4.2 ± 0.7	6	
60 nM	5.8	14	638
	SE		
	film thickness(nm)		
24 nM	8		57.7
60 nM	8		120
	QCM-D (open chamber, after 15min with no stirring)		
	film thickness(nm) (Sauerbrey)		areal mass density (ng/cm^2) + solvent coupled
24 nM	5.1		562
60 nM	8.6		945

Table 4.1 ***(preceding page)*****: Table comparing septin film heights and areal mass densities measured by AFM imaging, AFM nanoindentation, QCM-D, and SE. AFM:** The septin filament heights were obtained from peak fitting of pixel height histograms (see 3.7). For 60 nM, where the septin peak could not be distinguished from the membrane peak, we calculated a weighted height by summation of the histogram bars, setting the assumed membrane peak to a height of 0 nm. The maximum film heights from the AFM nanoindentation measurements were obtained from data sets presented in Fig. 4.8. The areal mass density was calculated by multiplying the septin volume by the mass density (1.1g/cm^3). **SE:** Film thickness and areal mass density were obtained from combined QCM-D/SE measurements in an open chamber, 15 min after protein deposition, and with no stirring, to enable a direct comparison with the AFM sample preparation.**QCM-D:** The thickness of the films was calculated from measured frequency shifts using the Sauerbrey equation (using a conversion factor Δ f $\times$ 6.1 Hz/nm).The areal mass density (which includes hydrodynamically coupled solvent) is calculated by multiplying the frequency shift by the mass sensitivity constant C = 18 ng/cm^2/Hz.

4.5 Supplemental material

4.5.1 Figures

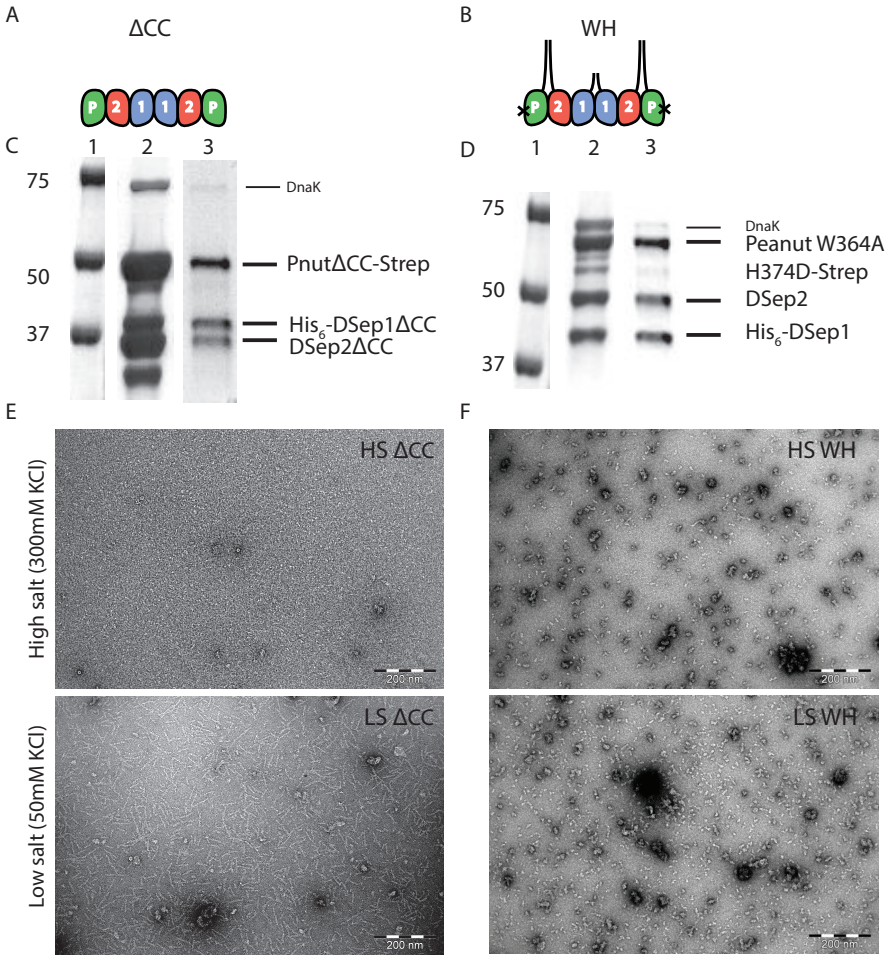

Figure S1: Characterization of septin mutants. (A) Schematic of the ΔCC septin mutant lacking the C-terminal extensions predicted to form coiled-coils on all its subunits, which should abolish filament pairing. (B) Schematic of the WH septin mutant, with two point mutations on the Pnut units. Assuming that the Pnut subunits are on the termini, these mutations should abolish end-to-end association. Alternatively it is possible that the Pnut subunits are central, such that the mutation generates trimers. (C) SDS-PAGE gel of the purified ΔCC mutant. (D) SDS-PAGE gel of the purified WH mutant. In (C) and (D), the lanes show: 1) Reference marker (molecular weights indicated on the left), 2) Nickel column eluate, 3) Strep column eluate. (E) TEM images of negatively stained samples of the ΔCC septin mutant at 210 nM in a high salt (HS: 300 mM KCl) buffer and at 84 nM in a low salt (LS: 50 mM KCl) buffer. In the LS conditions, we observe predominantly dimers of hexamers with a length of ~ 48nm. (D) TEM images of the WH septin mutant at 165 nM in HS and at 65 nM LS buffer conditions. The WH mutant does not polymerize at all in the LS conditions.

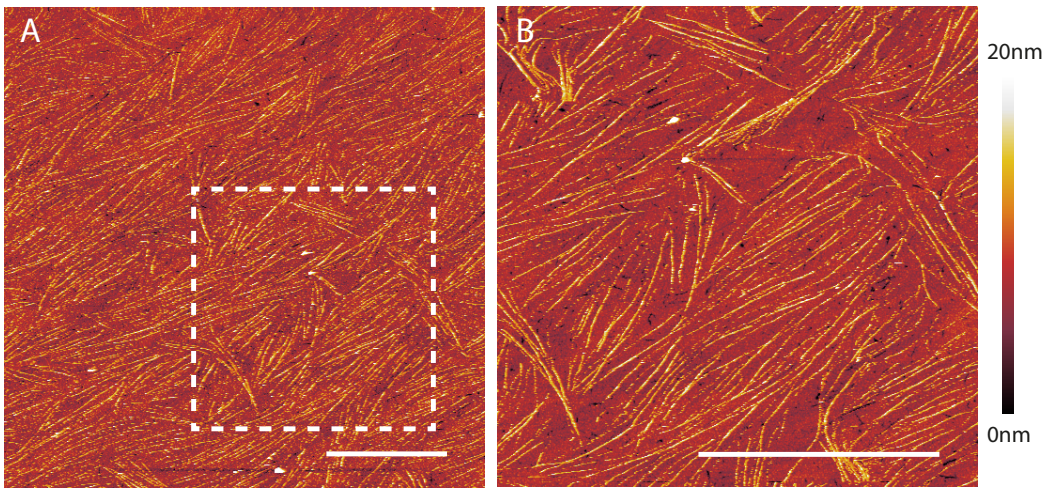

Figure S2: Topographic images obtained by AFM show that fly septin hexamers form filaments on bilayer-coated QCM-D sensor. (A) Septins (60 nM) fixed with GTA at 1 wt-% on a lipid bilayer composed of 80% DOPC and 20% PS on a QCM-D sensors. We observe similar filaments to those imaged in the same conditions on silicon wafers (see Chapter 3). (B) Zoom-in of the region indicated by the white rectangle in panel (A). Scale bars: 5 µm. Color bar on the right displays the height scale. The images show the presence of small defects (darkest color) in the bilayer, likely due to the larger roughness of the QCM-sensor surface compared to that of silicon wafers. Notably, the nanoscale membrane roughness (of typically a few nanometers out of plane over a few tens of nm in plane) does not affect septin polymerization much, if at all.

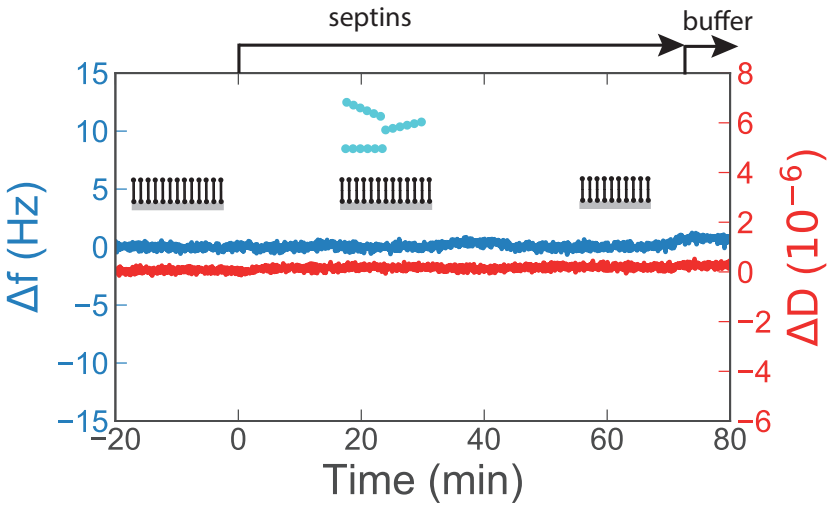

Figure S3: QCM-D measurements show that septins do not adsorb to uncharged lipid membranes. The frequency and dissipation shifts upon injection of 100 nM septins in the presence of an SLB composed of DOPC lipids only do not change over time, demonstrating that septins do not adsorb.

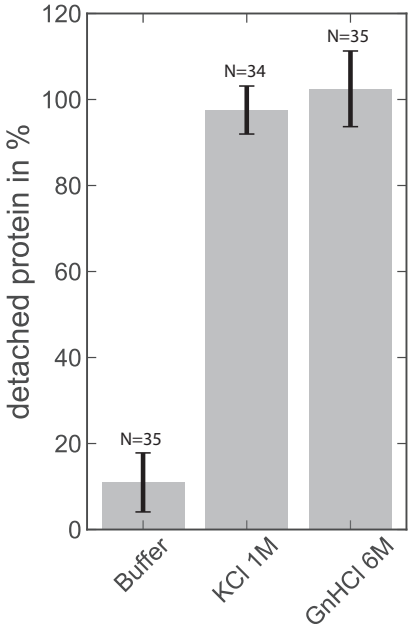

Figure S4: QCM-D measurements show that wild type septins are stably adsorbed to anionic lipid bilayers in a low salt buffer, whereas they desorb almost completely upon perfusion with a high salt buffer. Fraction of protein detachment after different rinsing steps, as quantified by the ratio between the frequency shift, Δf, measured before and after washing. After allowing septins to adsorb to bilayers for 60 min, the surface was sequentially rinsed with i) septin buffer (30 min), ii) septin buffer supplemented with 1M KCl (20 min) and iii) 6 M GnHCl (15 min). Error bars represent standard deviations of the mean for duplicate measurements. Data obtained on membranes with different compositions (PIP_2 5%, PS 20%, PIP_2 5% PS 20%) and with different septin concentrations (data for 6, 12, 24 and 60 nM were pooled together).

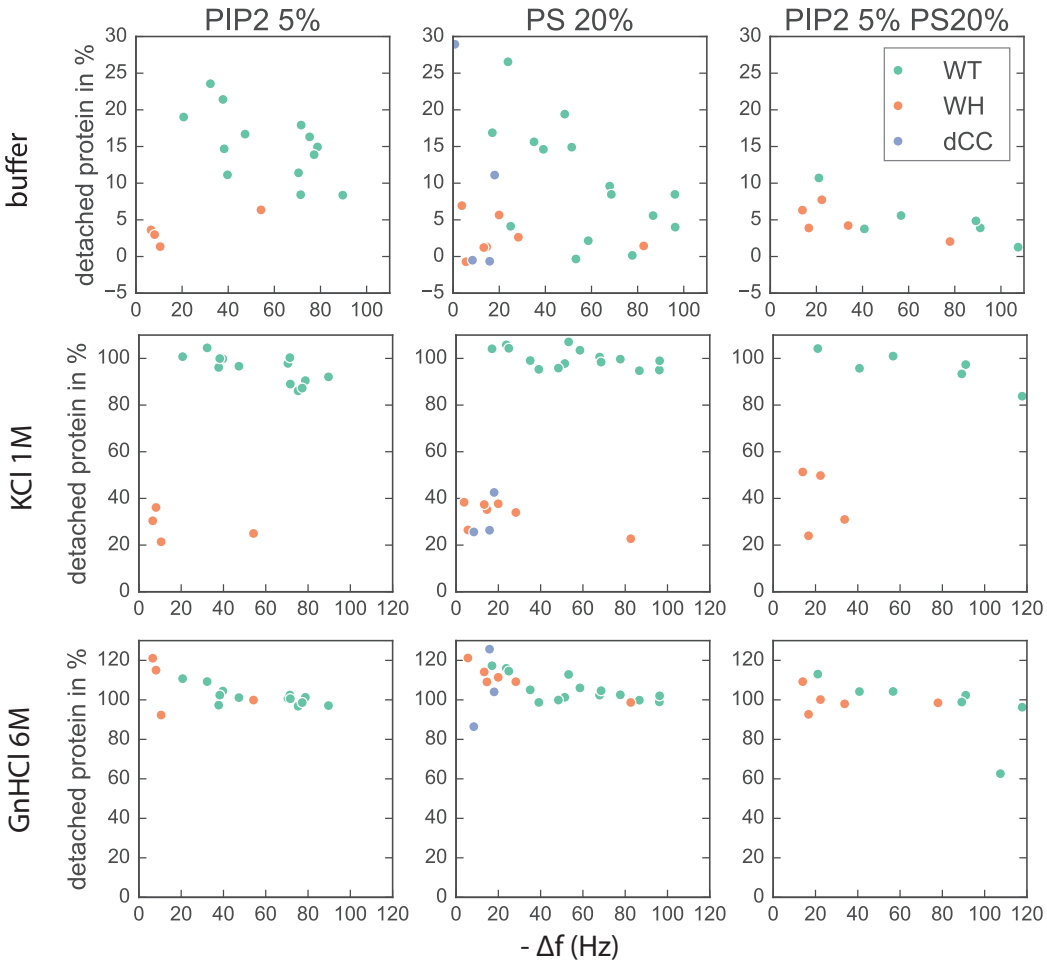

Figure S5: Adsorption of the WH septin mutant and the ΔCC septin mutant to lipid bilayers is only partially reversible in high salt buffer. Fraction of protein (wild type (WT) or mutants, see legend) detached after different rinsing steps, as quantified by the ratio between the frequency shifts Δf before and after washing, plotted as a function of the initial Δf before washing. Septins were allowed to adsorb for 60 min on bilayers composed of DOPC doped with (A) 5% PIP_2, (B) 20% PS, and (C) 5% PIP_2 and 20% PS. The surface was sequentially rinsed with i) septin buffer (30 min), ii) septin buffer supplemented with 1 M KCl (20 min), and iii) 6 M GnHCl (15 min). Total number of experiments per condition: N=39 (WT), 16 (WH), 4 (ΔCC). Each data point correspond to a single experiment (see table S3)

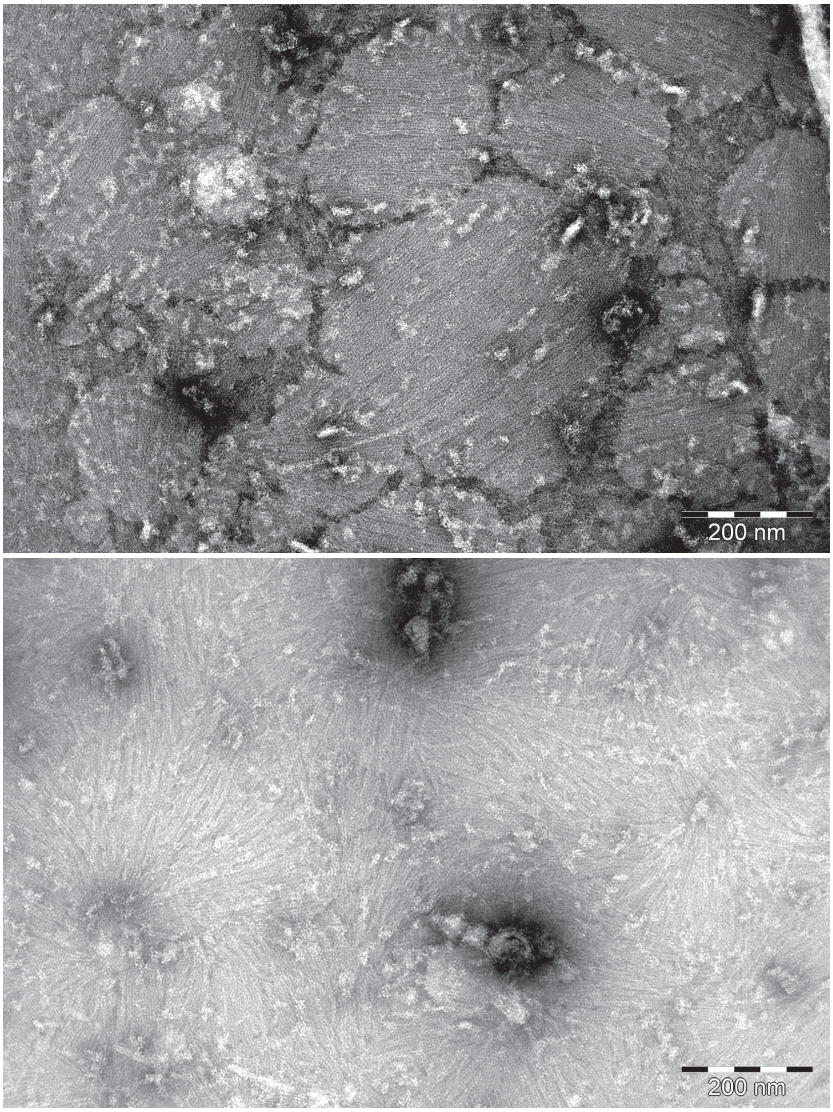

Figure S6: The ΔCC septin mutant forms filaments on negatively charged bilayers. Addition of 210 nM of the protein on a negatively charged lipid monolayer composed of 80% DOPC, 10% PS and 10% PIP_2 results in the formation of sheets of closely spaced, long and unpaired filaments. Both images are obtained in the same conditions.

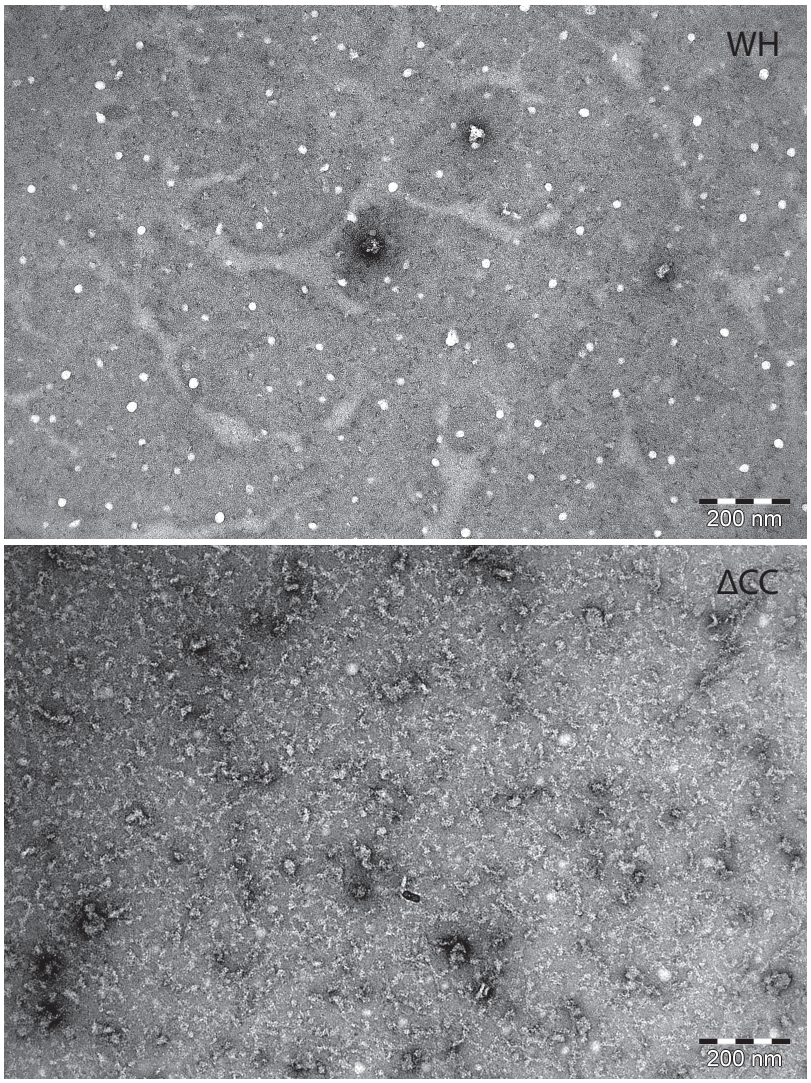

Figure S7: Electron microscopy images to test for binding of the WH and ΔCC septin mutants to pure DOPC monolayers. TEM images of negatively stained DOPC monolayers incubated with (top) the WH septin mutant (0.05 mg/ml, corresponding to 165 nM) and (bottom) the ΔCC mutant (0.05 mg/ml, corresponding to 210 nM). We do not observe any binding of the WH mutant, while the ΔCC septin mutant binds in an unorganized manner.

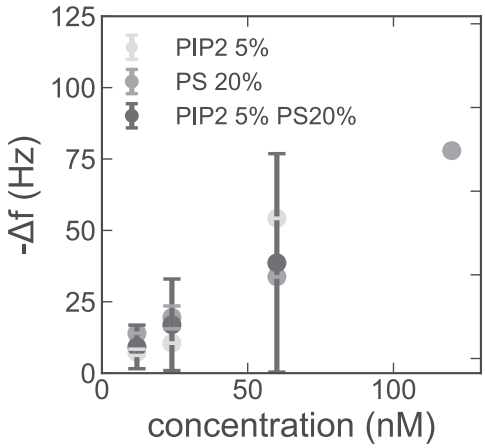

Figure S8: WH septin mutant attachment to the lipid bilayer correlates with septin concentration but not lipid composition Plot shows septin coverage -Δf after 60 min of protein deposition of WH septin mutant for different bilayer compositions and septin concentrations. Note that 6 out of 16 data points exceed 20 Hz (see Table S4), indicating the formation of a septin multilayer.

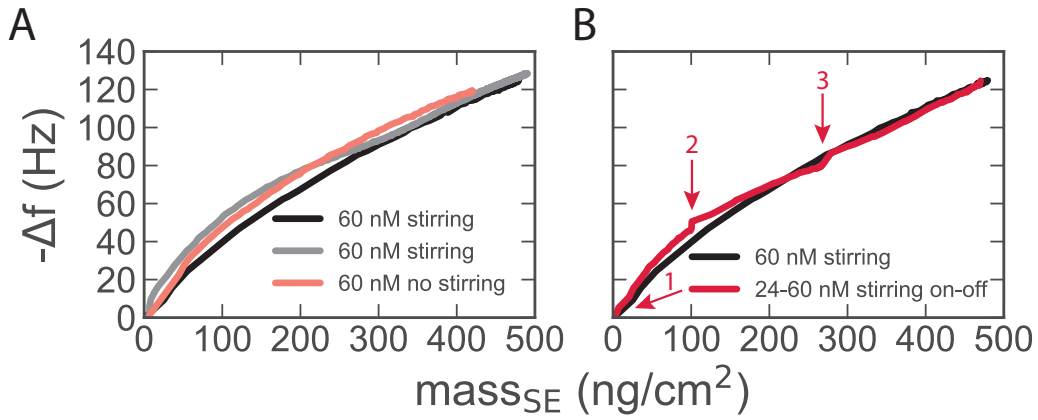

Figure S9: The frequency shifts measured by QCM-D are correlated with areal mass densities obtained by SE. (A) The correlation between the frequency shift measured by QCM-D and the areal mass density of septins quantified by SE is similar in the presence and absence of stirring. Septins (60 nM) were incubated with DOPC bilayers containing 20% PS. (B) The correlation is also similar when septins are immediately adsorbed at 60 nM, or when septins are first incubated at 24 nM and then at 60 nM. Arrows indicate different steps of the experiment 1: 24 nM of septin is added in non-stirred conditions, 2: stirring is switched on, 3: septins are added up to 60 nM final septin concentration, while still stirring.

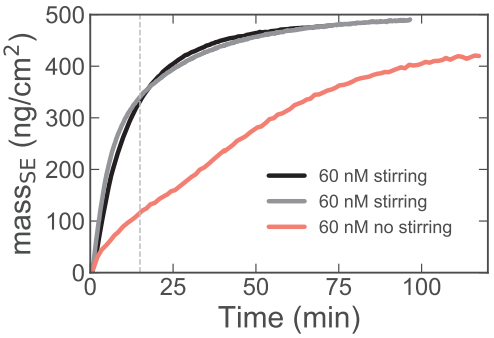

Figure S10: Stirring enhances the kinetics of septin adsorption to lipid bilayers. Binding curves for septins (60 nM) adsorbing to a lipid bilayer composed of DOPC doped with 20 mole% of PS in an open chamber with either stirring or no stirring conditions (correspond to experiments in Fig. S9A). Black and grey curves represent 2 repeat measurements obtained in stirring conditions, showing their reproducibility. The vertical grey line corresponds to 15 min of measurement, which is the time point where we can compare the septin mass deposited in non-stirring conditions (SE) with the mass of septin deposited during AFM experiments (see Table 4.1).

4.5.2 Tables

lipid	c_{septin}(nM)	N
PIP_2 5%	6 12 24 60	1 5 5 4
PS 20%	6 12 24 60	3 5 7 4
PIP_2 5% PS 20%	6 12 24 60	1 2 2 2

Table S1: Number of experiments (N) per condition corresponding to data points in Fig. 4.3B.

lipid	c_{septin}(nM)	septin	N
PIP_2 5%	6	WT	1
	12	WH	2
		WT	5
	24	WH	1
		WT	5
	60	WH	1
		WT	2
PS 20%	6	WT	3
	12	WH	2
		WT	5
	24	WH	2
		WT	7
		ΔCC	7
	60	WH	3
		WT	4
		ΔCC	2
PIP_2 5% PS 20%	6	WT	1
	12	WH	1
		WT	2
	24	WH	2
		WT	2
	60	WH	1
		WT	2

Table S2: Number of experiments (*N*) per condition corresponding to data points in Fig. 4.4D.

detaching agent	lipid	septin	N
buffer	PIP_2 5%	WH	4
		WT	13
	PS 20%	WH	7
		WT	15
		ΔCC	4
	PIP_2 5% PS 20%	WH	5
		WT	7
KCl 1M	PIP_2 5%	WH	4
		WT	13
	PS 20%	WH	7
		WT	15
		ΔCC	4
	PIP_2 5% PS 20%	WH	4
		WT	6
GnHCl 6M	PIP_2 5%	WH	4
		WT	13
	PS 20%	WH	7
		WT	15
		ΔCC	4
	PIP_2 5% PS 20%	WH	5
		WT	7

Table S3: Number of experiments (N) per condition corresponding to data points in Fig. S5.

lipid	c_{septin}(nM)	N
PIP_2 5%	12	2
	24	1
	60	1
PS 20%	12	2
	24	2
	60	3
PIP_2 5% PS 20%	12	1
	24	2
	60	1
	120	1

Table S4: Number of experiments (N) per condition corresponding to data points in Fig. S8.

5

Summary and Outlook

5.1 Summary

Cells constantly undergo shape changes that are necessary to perform their functions, such as cell migration, cell division, and tissue (re)generation. Cytoskeletal proteins play a crucial role in driving these shape changes, yet at the same time they maintain the mechanical integrity of the cell. Microtubules, intermediate filaments and actin filaments are the main components of the cytoskeletal machinery of animal cells. These proteins are all filamentous, but differ in their spatial distribution in the cell, and in their dynamical and mechanical properties. The main cytoskeletal component that drives cell shape changes is actin, which forms a thin crosslinked meshwork at the cell cortex, right underneath the plasma membrane. Myosin motor proteins exert forces on actin filaments and drive actin network contraction. However, for contraction to result in cell shape changes, the actomyosin cortex has to be linked to the plasma membrane.

In this thesis we focus on an understudied cytoskeletal protein known as septin, which likely acts as a linker between the actomyosin cortex and the plasma membrane. Like actin, septin is found mostly at the cell cortex, forms filamentous structures, and is important to maintain cell rigidity. Septins are important in a variety of cell functions that involve cell shape changes, like cell division and migration. They interact with actin and microtubules, contributing to cytoskeletal crosstalk. Moreover, septins provide diffusion barriers at specialized regions of the cell membrane, especially in regions where the plasma membrane exhibits high curvature. The available data suggest that 1) septins themselves can locally influence cell shape and rigidity, and that 2) septins can act as linkers of actomyosin to the plasma membrane, allowing for the transduction of actomyosin forces directly to the plasma membrane.

However, there is a lack of knowledge on the assembly properties of septins, alone and in the presence of lipid membranes.

The main goal of this thesis is to understand how septins assemble into higher order filamentous structures, and how these structures allow septins to perform their functions at the cell cortex. To simplify the complex cell environment, we design *in vitro* reconstitution experiments based on recombinantly expressed septins from the genetic model organism *Drosophila melanogaster*.

In **Chapter 2** we characterize septin self-assembly in bulk solution. We use fluorescence microscopy to investigate fly septin bundle formation across different concentrations and compare this with the so far better characterized assembly properties of yeast septins. We find that fly septins form rigid bundles above an onset concentration of 200 nM, while yeast septins form paired filaments at concentrations that are 10 times lower. We investigate further features of the septin bundles using STEM, an electron microscopy method that permits spatially resolved measurements of the protein mass. First, we confirm prior findings that yeast septins form predominantly paired filaments in solution. Then we characterize fly septin bundles formed at high septin concentrations, and find that they form thick structures up to 250 nm in width and with tapered ends. By mass mapping, we calculate that these bundles are composed of hundreds of hexamers per cross-section. Close to the onset concentration for bundling (200 nM), we observe similar tapered bundle structures, although thinner (~20 hexamers per cross-section), and we also find another type of bundle, with a constant width of ~60 nm, blunt ends, around 6 to 8 subunits per cross-section, and a characteristic groove along the long axis. These findings allow us to speculate about the intermediate steps of septin bundle assembly.

In **Chapter 3** we characterize septin assembly in the presence of biomimetic lipid membranes. We observe that in contrast to the thick bundles formed in solution, septins form a dense layer of thin filaments on lipid bilayers containing negatively charged lipids. We show that the septin-lipid interaction is electrostatic in origin, unlike in the case of yeast septins, which specifically bind phosphoinositide lipids. To resolve the ultrastructural details of the membrane-bound septin layers, we turned to higher resolution microscopy techniques. Transmission electron microscopy (negative stain and cryoEM) revealed that septins form single and paired filaments, which are tightly packed together in flat, ribbon-like bundles. Atomic force microscopy (AFM) imaging in liquid showed that the septin film thickness increased from 4 nm at 12 nM septins to 18 nm for 60 nM septins. Furthermore, we showed that flat ribbon-like septin bundles are resistant to the mechanical force exerted by the AFM tip while scanning, whereas single filaments are more prone to get dislocated. This finding suggests that lateral interactions between septin filaments impart mechanical strength to septin films. Our findings prove that membrane binding catalyzes septin higher order assembly and that septin-lipid interactions compete with septin-septin interactions in the solution. These findings provide new evidence that the presence of septins at the cell cortex may be (at least in part) driven by direct interactions with the plasma membrane and that membrane-bound septins

may potentially contribute to cortical rigidity.

In **Chapter 4** we characterize the kinetics of membrane-binding of septins using a surface analytical technique known as quartz-crystal microbalance with dissipation monitoring (QCM-D). We show that septin binding to the lipid bilayer is driven by electrostatic interactions and is mass transport limited. Furthermore we show that septins do not desorb upon washing with buffer, suggesting a strong interaction with the lipid bilayer. We also show that the septin layer is thin (being composed of at most 3 septin layers), relatively rigid, and self-limited in growth. We directly confirm by AFM nanoindentation measurements that the septin films have a maximum thickness of 14 nm. By combining QCM-D with concurrent optical measurements of septin adsorption by spectroscopic ellipsometry, we reveal that the septin films contain a large (80%) mass fraction of hydrodynamically coupled solvent, consistent with the porous architecture of the filamentous films. All these findings together allow us to propose a model of septin higher order assembly on model lipid membranes, which may guide future studies of the architecture and mechanical functions of septins at the cell cortex.

5.2 Outlook

In this thesis we characterized septin-septin and septin-membrane interactions. Our results provide evidence that septins can interact with lipid membranes with a lipid composition that resembles that of the inner leaflet of the plasma membrane, and that this interaction modulates septin higher order assembly. Given that septins are known to interact also with actin filaments [15, 53], our results imply that septins could act as an actin cortex-membrane linker.

We investigated this possibility by designing an *in vitro* model system, in which we linked actin filaments to a solid-supported lipid bilayer via septins. In this assay all the components are added sequentially. We first formed a lipid bilayer containing DOPC and 20 mole% DOPS lipids on a glass surface (as described in Chapter 3). We doped the bilayer with a small percentage of Rhodamine-PE lipids for visualization by total internal reflection fluorescence (TIRF) microscopy. We washed the lipid bilayer with buffer to remove residual vesicles and flushed in a solution of fly septin hexamers at a concentration of 500 nM, where 10% of the hexamers were GFP-labeled. We next washed the channel with buffer to remove septins remaining in the solution. We pre-polymerized actin filaments at a concentration of 2.4 μM by combining unlabeled monomeric actin with 10% actin that was labeled with Alexa Fluor 647. We flushed in the actin filaments together with 24 nM of the human cross-linking protein α-actinin-1 to create a connected actin network, and with 0.1% methylcellulose, to prevent shear-induced rupture of actin filaments [222]. We selected all the fluorescent labels such that we could image the lipid bilayer, septins and actin filaments at the same time. Fig. 5.1A shows a schematic depiction of the assay, while Fig. 5.1B shows fluorescence images of the lipid membrane, the septins,

and the actin filaments. The septins formed a homogeneous meshwork on top of the bilayer, consistent with the results reported in Chapter 3. The actin filaments formed a random network all across the channel. The actin signal did not co-localize with the septin signal. Importantly, the attached actin filaments were not bundled or curved, which would be expected in case septins and actin are co-polymerized [53]. This observation suggests that the septins are firmly attached to the membrane and that they do not detach from the lipid membrane when actin is added.

To investigate whether it is possible to induce contraction of the septin-anchored actin cortex, we added myosin II motor proteins purified from rabbit skeletal muscle [223]. We aimed at a final actin : α-actinin : myosin molar ratio of 1:0.1:0.1, which should promote large-scale contraction [222]. Interestingly, after myosin addition, we observed that septin and actin concurrently reorganized and formed aster-like structures (Fig. 5.2). Within 20 minutes, septin and actin clustered together. This observation provides clear evidence that actin is indeed interacting with septin. We observed that septins, while remodeling, left behind septin-depleted zones, suggesting that septins can 'slide' along the membrane surface. Septin structures did not go out of the focal plane or rapidly change location, indicating that they are not detached from the surface.

To quantify the degree of colocalization between actin and septins, we used the ImageJ plugin Coloc2 [134] to calculate the Pearson's correlation coefficient R at different time points for 4 different samples (Fig. 5.3). This coefficient can take on values between $R = -1$ (which signifies perfect anti-correlation), $R = 0$ (which means no correlation), and $R = 1$ (which means perfect (linear) correlation). In our experiments, the initial R-values varied between 0.4 and 0.7. The variability in the initial R-values could be due to variations in the time needed to place the sample on the microscope after myosin addition, as well as to the inhomogeneous distribution of actin. In all cases, the R-value progressively increased over time while the samples were contracting, reaching final values between 0.8 and 0.93. We note that after $\sim$1.5 hours of imaging we observed actin and septin clusters all over the channel surface, but their sizes and spacing varied, suggesting that the amount and distribution of actin is not the same throughout the channel.

To test the role of septins in regulating contractility of the acto-myosin network, we repeated the experiments in a control experiment, in which an acto-myosin network of the same composition was deposited on the membrane in the absence of septins. In this case, we observed a much faster formation of the actin clusters (Fig. 5.4): it took about 2 minutes to observe aster-like structures for the unattached actomyosin network, compared to 10-20 minutes for the septin-anchored actomyosin network. Thus, septins slow down network contraction, confirming our previous conclusion that septins can act as an actin-membrane linker.

In our proof of principle experiment we proved that septins can simultaneously interact with actin and a bilayer membrane. This finding suggests that the membrane binding domain of septins is distinct from the actin-binding domain. This observation may help future efforts to identify the actin-binding domain of septins. Remarkably,

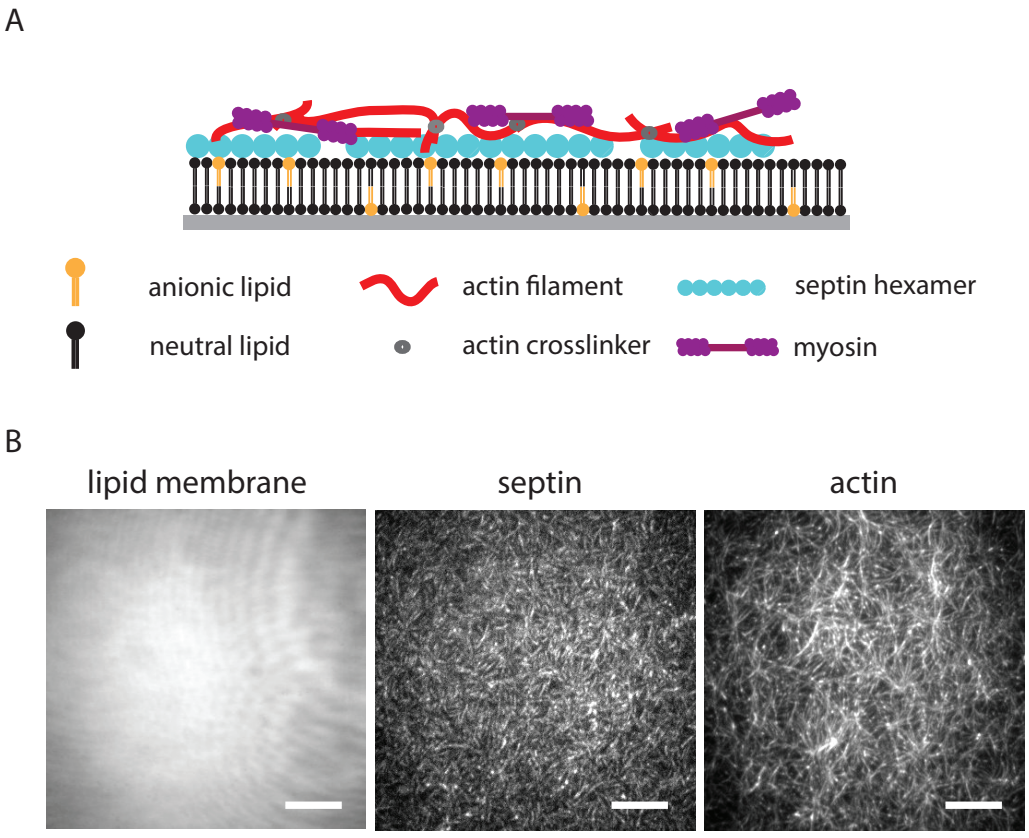

Figure 5.1: *In vitro* reconstitution assay where a contractile actin-myosin cortex is linked to a glass-supported lipid bilayer via septins . (A) Schematic depiction of the model system, which is built up in a sequential fashion: 1) Small unilamellar vesicles containing DOPC and 20% PS lipids are flushed onto a glass surface to form a supported lipid bilayer. 2) Remaining vesicles are washed out. 3) Septin hexamers at a concentration of 500 nM are added. 4) Unattached septins are washed out. 5) Pre-polymerized actin filaments (2.4 µM) crosslinked with 24 nM α-actinin-1 are added on top. 6) Contraction is initiated by flushing in rabbit skeletal muscle myosin II. B) TIRF images of a supported bilayer (left) with septins (middle) and actin filaments (right), observed before myosin addition. The bilayer is homogeneous (the striations are an imaging artefact). The septins form a homogeneous meshwork on the bilayer. Actin filaments deposited on the septin layer form an unorganized filamentous network. The septin and actin signals do not co-localize. Scale bars: 10 µm.

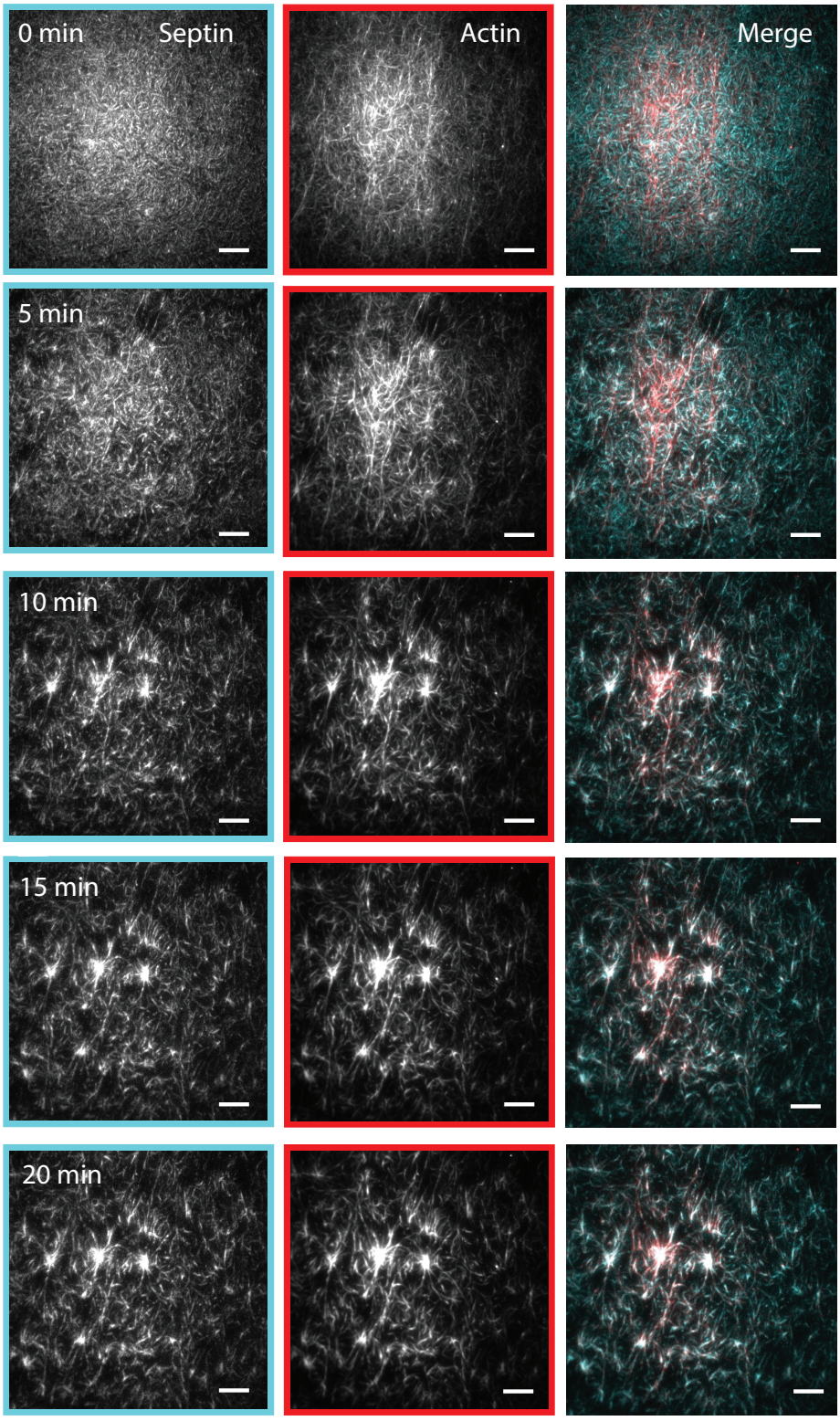
0 min
Septin
Actin
Merge
5 min
10 min
15 min
20 min

we observed that actomyosin contraction can cause sliding of septins across the membrane. We showed in Chapter 3 of this thesis that septins form bundle arrays on the membrane, whose formation is facilitated by lateral interaction between the filaments. Therefore, the overall interaction area of each septin structure with the lipid membrane is large. Our findings suggest that directed pulling forces from myosins are large enough to rupture the bonds involved in septin-lipid interactions, but not large enough to pull septin structures from the membrane. This observation may have implications in the cell, where large forces generated by the actomyosin cortex can be directly transferred onto the plasma membrane via septins, which can sustain such forces without detaching either from the actin cortex or from the plasma membrane.

It will be interesting to study the consequences of septin-mediated anchoring on actomyosin network contraction in more detail. An exciting next step would for instance be to label the negatively charged lipids that interact with the septins and test whether myosin-driven contraction can remodel the membrane and sequester the charged lipids underneath septin-actin asters. Three-dimensional lipid membrane model systems such as giant unilamellar vesicles could then become a useful tool to investigate actomyosin-septin induced membrane deformations [41].

Acknowledgements

I thank my talented and devoted students: Jasmijn van Loo, who set up the contractile assay, and Cees de Wit, who collected a lot of exciting data, part of which is shown in this chapter. I thank Marjolein Kuit-Vinkenoog and Jeffrey den Haan for protein purification.

Figure 5.2 *(preceding page)*: TIRF imaging shows that myosin addition causes coupled septin and actin remodeling. The images show the distribution of septins (left column) and actin (center column) at different moments in time (rows) after the addition of myosin. The time is arbitrarily set to zero for the first acquired image, which is taken as soon as possible after adding myosin and placing the sample on the microscope. On average, this takes about 30 seconds from the moment of myosin addition. The right-hand column shows merged septin (blue) and actin (red) signals. Co-localization of actin and septin in aster-like structures is evident from the white pixels.

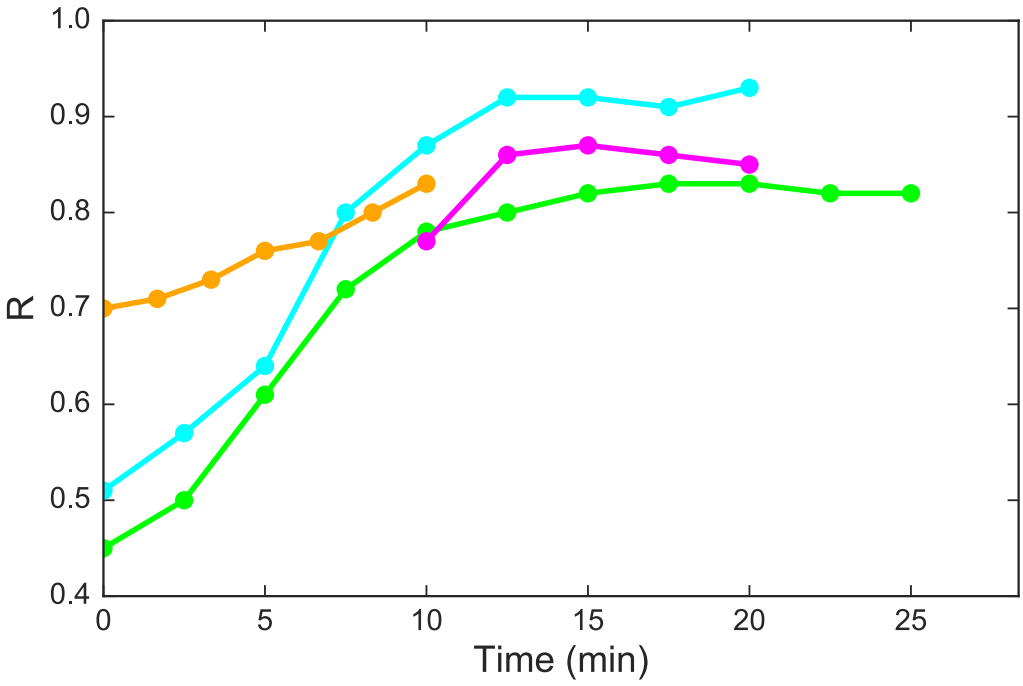

Figure 5.3: Actin-myosin co-localization increases in time upon myosin addition. Quantification of the time-dependent co-localization of septin and actin expressed in terms of the Pearson's correlation coefficient R for 4 different samples. In all cases, myosin-driven contraction causes progressive co-localization of actin and septins. Cyan line corresponds to the experiments presented in Fig. 5.2.

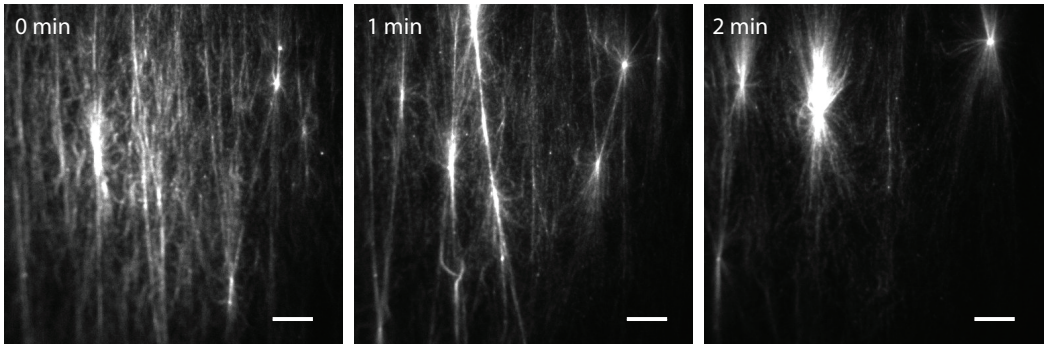

Figure 5.4: Actomyosin contraction on a solid-supported lipid membrane in the absence of septins. Pre-polymerized actin filaments (2.4 µM) crosslinked with 24 nM α-actinin-1 were added to the channel. Next, myosin (24 nM) was added to initiate contraction. Time zero indicates the moment when the first image was acquired, which is about 30-60 seconds after the addition of the myosin. The actin filaments are somewhat flow-aligned. Over time, myosin remodels the actin filaments into asters.

Acknowledgements

I would like to greatly thank Gijsje for her supervision. You are a very inspiring scientist and wonderful mentor. I appreciate your involvement in the project at its every step. Every meeting with you gave me new hope and motivation. Under your guidance, I learned to critically look at the data and get as much as possible out of it, not to jump too fast into conclusions, express my thoughts in a clear(er) manner and to look at the findings in a wider picture, which allowed me to put my work into perspective. All these skills will help me in the future, regardless of how my career evolves. I also always admired your time-managing skills. It is incredible how much high-quality work you can do, yet having a good life-work balance. Finally, I would also like to point out a unique combination of constructive feedback, subtle criticism and empathy when you manage people. I always felt that there was a good mentor-team relationship because there was always will for understanding and help.

Aurélie, Manos, Ralf, I was very grateful to have you all as my collaborators. The discussions with you were always very inspiring. Thank you for many hours you spent with me to explain the new techniques and to perform experiments. Thank you for your very insightful feedbacks and suggestions. I travelled to see you many times, and you always made me feel part of your own groups. Aurélie, the way you pour liquid nitrogen is just something else. Manos, your experimental precision sometimes felt overwhelming but was often life saving. Ralf, it was hard to hear you sometimes, but whatever you said, was always worth noting down.

Biological Soft Matter Group was a source of inspiration and help throughout my whole PhD. Yuval, you've been a fun project partner. You are very clever with an interesting personality, so I predict you a great future as far as your job is based on digital writing exclusively. Viktoria, it has been a pleasure to have you as a postdoc in our MINICELL team. I took me a while to understand your unique sense of humour, but now I consider it as a good one. Anders, you are a true social animal and your energy spans over the lab and way beyond it. Thank you for all the discussion and time spent together in Amsterdam and in Leeds. Cristina, you are a superhero of coding and image analysis, without you some of my work would have not been so thoughtfully analysed. STEM sessions under scary caffeine levels were a pleasure. Fede, I was very happy the day you accepted your position at AMOLF, as I knew

you would be a great person to interact with and I was not mistaken. You are always hungry for new adventures and your optimism and cheeky jokes are always very attractive. Celine, you are a very chilled yet responsible and hard-working person and I really loved your soft-but-sharp comments. Bart, thank you for your critical remarks and very careful attention during the group meetings. I also enjoyed your pure happiness when talking about vegetarian food (including chocolate plums), unusual instruments and far-away travels. Aditya, our Science paper never happened, but we did some rocket science together, didn't we? Galja, you are a walking sunshine, even torture rooms in Germany were not that terrifying in your presence. Florian, you are the best all-rounder I have ever known. Your knowledge is so wide that I could listen to you all day and night. At least now I can enjoy your blog from everywhere. Adeline, your time at AMOLF was short but your sweetness and devotion is well remembered. Jeanette, I loved listening about your many hobbies and now I am a big fun of your pottery. Feng, thank you for showing me septin and actin filaments for the first time. They were beautiful. Jeffrey, let the AKTA power be with you, you started your battle with full commitment and thank you for that. Jasmijn and Cees, I appreciated that you were so motivated and engaged in the project. I could not ask for nicer and better students. I am very glad you jumped with full energy for your next career steps. Karin, Corianne, Nicholas, Tatjana, thank you for sharing with me some of your expertise. Luci, Lennard, Gerard, it was great to see you joining the lab and bringing new energy. With you on board, future of Biosoft group is secure.

The office has been undoubtedly a second home to me. Maga, you were the first person to introduce me to absolute richness of Amsterdam culture life. Thank you for sharing with me your experiences and for an unforgettable road trip in Mexico. Simone, thank you for keeping a little bit of German order in the office, but not too much. We have drunk many beers, watched many movies, and experienced a lot of jazz together. Michele Monti, our colonel-simple soldier relationship allowed us to enjoy 4 years in one office. I will never forget what happened there, for your sake I will not share it with public. Joleen, Guizela, Jason, Eline, Sim and Antoine, I was happy to spend some office time with you.

I would like to thank my science girls with who I spent litres of coffee and discussed everything good and bad, important, and not relevant at all. Parisita, thank you for your reliability, honest opinions, engagement in discussions and for showing me your beautiful country. Cristina thank you for stimulating my body and soul with many fantastic events including your birthdays, every year celebrated in a very unique way. I trust in your yoga teaching skills and will remain your long-life ambassador. Jenny, your laugh will always ring in my ears. Whenever I see you on the horizon I already have to smile. Thank you for your 'goat' stories that very often made my day. Giada, your talents are so versatile, I hope you will manage to combine your interest in art, science and sustainability in the future.

Next, I would like to thank what is already commonly called as 'Levantkade crew'. Thank you for making your place so cosy and welcoming. Michele, special

tribute here for introducing me to peculiar style of consuming fruits, cakes and greens. Jacopo you have a real artistic soul. You have an amazing ability to bring together different types of very interesting people. Shanti, Titta, Tarque, Francesca, Diego, Ben, Steven, Bertus, Pepe, Oreste: it was always a pleasure to see you.

Mario and Olga, we met in Dresden, and I am so happy you made Amsterdam your further choice as well. Mario, you have a perfect set of skills to become a great scientist. I admire your scientific vision, programming skills and ability to convey and illustrate your ideas. I approve your tennis skills, board game dictatorship and engaging people for dancing and singing to trash music. Olga, it has been great to have you around, with your unique calmness and a great ability to tell Mario to shut up (or down). I enjoyed our hikes together, sharing a tent in total wildness of Russia, and getting excited about Georgian cuisine. Nicola, my favourite zerbino, you are a great friend. We have spent unforgettable time together. Thank you for analysing the evenings with a morning croissant and coffee, and analysing the days with an evening beer and burger. Thank you for saving my life from infamous tissue attack, and for many hikes together, especially reaching Toubkal with swollen fingers in Morocco. Martijn, you are passionate about science but also politics and fairness in the world, it was always refreshing to chat with you. Ale, thank you for always being up for a party and to eat something out as well as nice coffees and chats out of office hours. Marco, you are a topic of many funny anecdotes, thank you for that and for the way you express yourself. Giulia, your cooking is widely renown, memories of your tasty dishes and Italian hospitality will remain in my memory for long. Judith, you have a great understanding for often overwhelming presence of Expat community. Thank you for explaining to us Dutch language, habits and actions. Mathijs, I have never seen a person with so much energy, it was an interesting experience to have seen it being released. Further, I would like to thank multiple people who helped me or shared a discussion, laugh or coffee at AMOLF/ARCNL (and not only): Giorgio, Lorenzo, Roberto, Agustin, Giorgos, Konrad, Carolyn, Moritz, Kévin, Stef, Stephen, Steffen, Adithya, Joris, Noreen, Fatemeh, Vanda, Zuzana, Simone B., Yvonne, Katja, Lukas, Harmen, Vanessa, Keita, Ioana, Sander M., Sebastian O., Sebastian G., Clara, Jan-Bonne, Marko, Nuria, Sophie, Felipe, Erçağ, Andrea T., Verena, Christian, Nasim, Xuan, Bela, Peter-Rein, Jeroen, Kristina, Clyde, Wiebe, Tatiana, André, Arnelli, Angela, Wouter, Henk-Jan, Lutz, Hinco, Ad and Juliette.

I was very lucky to be involved in a few international collaborations which allowed me to travel to different places, get to know other labs and people. Jeanette and Feng, thank you for taking care of me when I was visiting Paris. I was always looking forward to catch up with you and experience Asian Parisian food. Francois, thank you for your patience in teaching me and Yuval septin purification. You are the only person in the world who thinks that Dutch kebab is the best. Nesrine, Leire, Boris, thank you for helping me out during my visits to San Sebastián and for nice chit-chats during coffee breaks. Aline and Karolina, you made me feel like at home in Donostia. Thank you for all the activities we did together including serious pintxos excursions. Aline, thank you for designing my beautiful cover. I would like

to thank other people in BiomaGUNE: Jimena, Suzana, Eliana, Desire, Paolin for nice moments together. Jon and Maider, thank you for sharing the flat with me and for introducing me to local culture. Fouzia, when I arrived to Leeds you were my full time-guide everywhere. Thank you for the fun time imaging in the AFM lab, for many coffees and trips together. Lewis, Rickard and Ashley, thank you for all for shared time in Ralf's part of the corridor.

I would like to thank people not associated with AMOLF who were also very important throughout my PhD journey. Laura, we became friends in Dresden during our studies, and we both ended up in Amsterdam. Thank you so much for all the precious time we spent together. Meetings and travels with you were always giving me a pleasant feeling of continuity and comforting friendship. Joanna, it is incredible how a person out of science can grasp it so well. I think the trick is that you listen to people carefully and with full understanding. Thank you for that and for all activities which were dragging me out of scientific circle and mindset. Marta, thank you for keeping me updated about life in Dresden, skiing trips and deep discussions. Agata, thank you for our irregular but efficient catch-ups and for a feel of folk in the Netherlands. Abel, Taraneh, Levania, Thijs, Olesia, Laura, Elena, Sonja, Jan, Andrea G., Sebastian M., Valeria, Masha, Wróbel, Ania Wróblowa, Ania S., Olga S., Ola, Margaux, Maria, Suvi, Felipe, Richard, Suzi, Felix R., Jaro, Santiago, Coleman, Franziska, Diana, Adam, Georg, Aniruddha, Rahul, Anastasia, KGW, Karen V., Karen. M., Alex, Douwe, Luca, Fabio, thank you for willingly or unwillingly getting updated about my progress.

Scott, I'm sorry to phrase it like this, but you are the best outcome of my collaborations. Thank you for helping me to survive long weeks in northern England and for being so cool about everything. I learned from you appreciating importance of 'baby steps' and 'routina'.

Finally, I would love to thank my family. I am very grateful to my parents for always giving me opportunities and support to follow my dreams and for teaching me what is really important in life. I would like to thank Jacek and Justyna for always giving me a warm welcome home. Babcia, your wisdom of life always gives me inspiration.

Bibliography

[1] G. van Meer, D. R. Voelker, and G. W. Feigenson, *Membrane lipids: Where they are and how they behave*, Nature Reviews Molecular Cell Biology **9**, 112 (2008).

[2] E. Sezgin, I. Levental, S. Mayor, and C. Eggeling, *The mystery of membrane organization: Composition, regulation and roles of lipid rafts*, Nature Reviews Molecular Cell Biology **18**, 361 (2017).

[3] A. Kapus and P. Janmey, *Plasma membrane–cortical cytoskeleton interactions: a cell biology approach with biophysical considerations.*, Comprehensive Physiology **3**, 1231 (2013).

[4] W. S. Trimble and S. Grinstein, *Barriers to the free diffusion of proteins and lipids in the plasma membrane*, The Journal of Cell Biology **208**, 259 (2015).

[5] A. Kusumi, K. G. Suzuki, R. S. Kasai, K. Ritchie, and T. K. Fujiwara, *Hierarchical mesoscale domain organization of the plasma membrane*, Trends in Biochemical Sciences **36**, 604 (2011).

[6] F. Huber, A. Boire, M. P. López, and G. H. Koenderink, *Cytoskeletal crosstalk: When three different personalities team up*, Current Opinion in Cell Biology **32**, 39 (2015).

[7] S. Mostowy and P. Cossart, *Septins: the fourth component of the cytoskeleton.*, Nature reviews. Molecular cell biology **13**, 183 (2012).

[8] H. Kang, M. J. Bradley, B. R. McCullough, A. Pierre, E. E. Grintsevich, E. Reisler, and E. M. De La Cruz, *Identification of cation-binding sites on actin that drive polymerization and modulate bending stiffness*, Proceedings of the National Academy of Sciences **109**, 16923 (2012).

[9] G. Salbreux, G. Charras, and E. Paluch, *Actin cortex mechanics and cellular morphogenesis*, Trends in Cell Biology **22**, 536 (2012).

[10] L. Blanchoin, R. Boujemaa-Paterski, C. Sykes, and J. Plastino, *Actin Dynamics, Architecture, and Mechanics in Cell Motility*, Physiological Reviews **94**, 235 (2014).

[11] S. Köster, D. A. Weitz, R. D. Goldman, U. Aebi, and H. Herrmann, *Intermediate filament mechanics in vitro and in the cell: From coiled coils to filaments, fibers and networks*, Current Opinion in Cell Biology **32**, 82 (2015).

[12] B. Nding and S. Kster, *Intermediate filaments in small configuration spaces*, Physical Review Letters **108**, 1 (2012).

[13] G. Borisy, R. Heald, J. Howard, C. Janke, A. Musacchio, and E. Nogales, *Microtubules: 50 years on from the discovery of tubulin*, Nature Reviews Molecular Cell Biology **17**, 322 (2016).

[14] F. Gittes, B. Mickey, J. Nettleton, J. Howard, F. Gittes, B. Mickey, J. Nettleton, and J. Howard, *Flexural Rigidity of Microtubules and Actin Filaments Measured from Thermal Fluctuations in Shape*, **120**, 923 (1993).

[15] E. T. Spiliotis, *Spatial effects-site-specific regulation of actin and microtubule organization by septin GTPases.*, Journal of cell science **131**, jcs207555 (2018).

[16] A. A. Bridges and A. S. Gladfelter, *Septin Form and Function at the Cell Cortex.*, The Journal of biological chemistry **290**, jbc.R114.634444 (2015).

[17] L. Hartwell, *Genetic control of the cell division cycle in yeast: IV. Genes controlling bud emergence and cytokinesis*, Experimental Cell Research **69**, 265 (1971).

[18] M. Kinoshita, *Assembly of Mammalian Septins*, Journal of Biochemistry **134**, 491 (2003).

[19] A. Bertin, M. A. McMurray, P. Grob, S. S. S. Park, G. Garcia, I. Patanwala, H. L. L. Ng, T. Alber, J. Thorner, and E. Nogales, *Saccharomyces cerevisiae septins: supramolecular organization of heterooligomers and the mechanism of filament assembly.*, Proceedings of the National Academy of Sciences of the United States of America **105**, 8274 (2008).

[20] C. M. John, R. K. Hite, C. S. Weirich, D. J. Fitzgerald, H. Jawhari, M. Faty, D. Schläpfer, R. Kroschewski, F. K. Winkler, T. Walz, Y. Barral, and M. O. Steinmetz, *The Caenorhabditis elegans septin complex is nonpolar*, EMBO J. **26**, 3296 (2007).

[21] C. M. Field, O. Al-Awar, J. Rosenblatt, M. L. Wong, B. Alberts, and T. J. Mitchison, *A purified Drosophila septin complex forms filaments and exhibits GTPase activity.*, The Journal of cell biology **133**, 605 (1996).

[22] M. E. Sellin, L. Sandblad, S. Stenmark, and M. Gullberg, *Deciphering the rules governing assembly order of mammalian septin complexes*, Mol. Biol. Cell **22**, 3152 (2011).

[23] N. F. Valadares, H. d' Muniz Pereira, A. P. Ulian Araujo, R. C. Garratt, H. d' Muniz Pereira, A. P. Ulian Araujo, and R. C. Garratt, *Septin structure and filament assembly*, Biophysical Reviews **9**, 481 (2017).

[24] M. Sirajuddin, M. Farkasovsky, E. Zent, and A. Wittinghofer, *GTP-induced conformational changes in septins and implications for function*, Proc Natl Acad Sci U S A **106**, 16592 (2009).

[25] M. Abbey, M. Gaestel, and M. B. Menon, *Septins: Active GTPases or just GTP-binding proteins?*, Cytoskeleton **76**, 55 (2019).

[26] A. Alonso, M. Greenlee, J. Matts, J. Kline, K. J. Davis, and R. K. Miller, *Emerging roles of sumoylation in the regulation of actin, microtubules, intermediate filaments, and septins*, Cytoskeleton (Hoboken) **72**, 305 (2015).

[27] Y. Hernández-Rodríguez and M. Momany, *Posttranslational modifications and assembly of septin heteropolymers and higher-order structures*, Current Opinion in Microbiology **15**, 660 (2012).

[28] J. Dobbelaere, M. S. Gentry, R. L. Hallberg, and Y. Barral, *Phosphorylation-dependent regulation of septin dynamics during the cell cycle*, Dev Cell **4**, 345 (2003).

[29] R. A. Meseroll, P. Occhipinti, and A. S. Gladfelter, *Septin phosphorylation and coiled-coil domains function in cell and septin ring morphology in the filamentous fungus Ashbya gossypii*, Eukaryot Cell **12**, 182 (2013).

[30] E. S. Johnson and G. Blobel, *Cell cycle-regulated attachment of the ubiquitin-related protein SUMO to the yeast septins.*, The Journal of cell biology **147**, 981 (1999).

[31] Y. Takahashi, M. Iwase, M. Konishi, M. Tanaka, A. Toh-e, and Y. Kikuchi, *Smt3, a SUMO-1 homolog, is conjugated to Cdc3, a component of septin rings at the mother-bud neck in budding yeast*, Biochemical and Biophysical Research Communications **259**, 582 (1999).

[32] D. Ribet, S. Boscaini, C. Cauvin, M. Siguier, S. Mostowy, A. Echard, and P. Cossart, *SUMOylation of human septins is critical for septin filament bundling and cytokinesis.*, The Journal of cell biology **216**, 4041 (2017).

[33] M. A. McMurray, A. Bertin, G. Garcia, L. Lam, E. Nogales, and J. Thorner, *Septin Filament Formation Is Essential in Budding Yeast*, Developmental Cell **20**, 540 (2011).

[34] M. Sirajuddin, M. Farkasovsky, F. Hauer, D. Kühlmann, I. G. Macara, M. Weyand, H. Stark, and A. Wittinghofer, *Structural insight into filament formation by mammalian septins.*, Nature **449**, 311 (2007).

[35] F. Soroor, M. S. Kim, O. Palander, Y. Balachandran, R. Collins, S. Benlekbir, J. Rubinstein, and W. S. Trimble, *Revised subunit order of mammalian septin complexes explains their in vitro polymerization properties*, bioRxiv , 569871 (2019).

[36] D. C. Mendonça, J. N. Macedo, R. Itri, S. L. Guimaraes, F. L. Barroso da Silva, A. Cassago, R. C. Garratt, R. Portugal, and A. P. U. Araujo, *Repositioning septins within the core particle*, bioRxiv , 569251 (2019).

[37] M. S. Kim, C. D. Froese, M. P. Estey, and W. S. Trimble, *SEPT9 occupies the terminal positions in septin octamers and mediates polymerization-dependent functions in abscission.*, The Journal of cell biology **195**, 815 (2011).

[38] V. Torraca and S. Mostowy, *Septins and Bacterial Infection.*, Frontiers in cell and developmental biology **4**, 127 (2016).

[39] S. Mostowy, M. Bonazzi, M. A. Hamon, T. N. Tham, A. Mallet, M. Lelek, E. Gouin, C. Demangel, R. Brosch, C. Zimmer, A. Sartori, M. Kinoshita, M. Lecuit, and P. Cossart, *Entrapment of Intracytosolic Bacteria by Septin Cage-like Structures*, Cell Host & Microbe **8**, 433 (2010).

[40] A. A. Bridges, M. S. Jentzsch, P. W. Oakes, P. Occhipinti, and A. S. Gladfelter, *Micron-scale plasma membrane curvature is recognized by the septin cytoskeleton*, The Journal of Cell Biology **213**, jcb.201512029 (2016).

[41] A. Beber, C. Taveneau, M. Nania, F. C. Tsai, A. D. Cicco, P. Bassereau, D. Lévy, J. T. Cabral, H. Isambert, S. Mangenot, and A. Bertin, *Membrane reshaping by micrometric curvature sensitive septin filament*, Nature Communications .

[42] D. Lobato-Márquez and S. Mostowy, *Septins recognize micron-scale membrane curvature*, The Journal of Cell Biology , jcb.201603063 (2016).

[43] L. Dolat, J. L. Hunyara, J. R. Bowen, E. P. Karasmanis, M. Elgawly, V. E. Galkin, and E. T. Spiliotis, *Septins promote stress fiber-mediated maturation of focal adhesions and renal epithelial motility*, Journal of Cell Biology **207**, 225 (2014).

[44] J. Saarikangas and Y. Barral, *The emerging functions of septins in metazoans*, EMBO Rep **12**, 1118 (2011).

[45] K. Neubauer and B. Zieger, *The Mammalian Septin Interactome*, Frontiers in Cell and Developmental Biology **5**, 3 (2017).

[46] J. Gilden and M. F. Krummel, *Control of cortical rigidity by the cytoskeleton: Emerging roles for septins*, Cytoskeleton **67**, 477 (2010).

[47] S. Mostowy, S. Janel, C. Forestier, C. Roduit, S. Kasas, J. Pizarro-Cerdá, P. Cossart, and F. Lafont, *A role for septins in the interaction between the Listeria monocytogenes invasion protein InlB and the Met receptor*, Biophysical Journal **100**, 1949 (2011).

[48] A. J. Tooley, J. Gilden, J. Jacobelli, P. Beemiller, W. S. Trimble, M. Kinoshita, and M. F. Krummel, *Amoeboid T lymphocytes require the septin cytoskeleton for cortical integrity and persistent motility*, Nature Cell Biology **11**, 17 (2009).

[49] A. Shindo and J. B. Wallingford, *PCP and septins compartmentalize collective cell movement*, Science **343**, 649 (2014).

[50] M. Ihara, A. Kinoshita, S. Yamada, H. Tanaka, A. Tanigaki, A. Kitano, M. Goto, K. Okubo, H. Nishiyama, O. Ogawa, C. Takahashi, S. Itohara, Y. Nishimune, M. Noda, and M. Kinoshita, *Cortical organization by the septin cytoskeleton is essential for structural and mechanical integrity of mammalian spermatozoa*, Dev Cell **8**, 343 (2005).

[51] J. D. Steels, M. P. Estey, C. D. Froese, D. Reynaud, C. Pace-Asciak, and W. S. Trimble, *Sept12 is a component of the mammalian sperm tail annulus*, Cell Motility and the Cytoskeleton **64**, 794 (2007).

[52] T. Tada, A. Simonetta, M. Batterton, M. Kinoshita, D. Edbauer, and M. Sheng, *Role of Septin cytoskeleton in spine morphogenesis and dendrite development in neurons*, Curr Biol **17**, 1752 (2007).

[53] M. Mavrakis, Y. Azou-Gros, F. C. Tsai, J. Alvarado, A. Bertin, F. Iv, A. Kress, S. Brasselet, G. H. Koenderink, and T. Lecuit, *Septins promote F-actin ring formation by crosslinking actin filaments into curved bundles*, Nature cell biology **16**, 322 (2014).

[54] C. Smith, L. Dolat, D. Angelis, E. Forgacs, E. T. Spiliotis, and V. E. Galkin, *Septin 9 Exhibits Polymorphic Binding to F-Actin and Inhibits Myosin and Cofilin Activity*, Journal of Molecular Biology **427**, 3273 (2015).

[55] Y. Tanaka-Takiguchi, M. Kinoshita, and K. Takiguchi, *Septin-Mediated Uniform Bracing of Phospholipid Membranes*, Current Biology **19**, 140 (2009).

[56] J. K. Gilden, S. Peck, Y. C. M. Chen, and M. F. Krummel, *The septin cytoskeleton facilitates membrane retraction during motility and blebbing.*, The Journal of cell biology **196**, 103 (2012).

[57] S. K. Kim, A. Shindo, T. J. Park, E. C. Oh, S. Ghosh, R. S. Gray, R. A. Lewis, C. A. Johnson, T. Attie-Bittach, N. Katsanis, and J. B. Wallingford, *Planar cell polarity acts through septins to control collective cell movement and ciliogenesis.*, Science (New York, N.Y.) **329**, 1337 (2010).

[58] T. J. Park, S. K. Kim, and J. B. Wallingford, *The planar cell polarity effector protein Wdpcp (Fritz) controls epithelial cell cortex dynamics via septins and actomyosin*, Biochemical and Biophysical Research Communications **456**, 562 (2015).

[59] C. Cauvin and A. Echard, *Phosphoinositides: Lipids with informative heads and mastermind functions in cell division*, Biochimica et Biophysica Acta (BBA) - Molecular and Cell Biology of Lipids **1851**, 832 (2015).

[60] K. Song, G. Russo, and M. Krauss, *Septins As Modulators of Endo-Lysosomal Membrane Traffic*, **4**, 1 (2016).

[61] A. A. Bridges, H. Zhang, S. B. Mehta, P. Occhipinti, T. Tani, and A. S. Gladfelter, *Septin assemblies form by diffusion-driven annealing on membranes.*, Proceedings of the National Academy of Sciences of the United States of America , 1 (2014).

[62] A. Bertin, M. a. McMurray, L. Thai, G. Garcia, V. Votin, P. Grob, T. Allyn, J. Thorner, and E. Nogales, *Phosphatidylinositol-4,5-bisphosphate Promotes Budding Yeast Septin Filament Assembly and Organization*, Journal of Molecular Biology **404**, 711 (2010).

[63] A. Casamayor and M. Snyder, *Molecular Dissection of a Yeast Septin : Distinct Domains Are Required for Septin Interaction , Localization , and Function*, Mol. Cell Biol. **23**, 2762 (2003).

[64] L. Dolat and E. T. Spiliotis, *Septins promote macropinosome maturation and traffic to the lysosome by facilitating membrane fusion*, J Cell Biol **214**, 517 (2016).

[65] J. Zhang, C. Kong, H. Xie, P. S. McPherson, S. Grinstein, and W. S. Trimble, *Phosphatidylinositol polyphosphate binding to the mammalian septin H5 is modulated by GTP*, Current Biology **9**, 1458 (1999).

[66] S. Yamada, T. Isogai, R. Tero, Y. Tanaka-Takiguchi, T. Ujihara, M. Kinoshita, and K. Takiguchi, *Septin Interferes with the Temperature-Dependent Domain Formation and Disappearance of Lipid Bilayer Membranes*, Langmuir **32**, 12823 (2016).

[67] C. M. Field and B. M. Alberts, *Anillin, a contractile ring protein that cycles from the nucleus to the cell cortex*, J. Cell Biol. **131**, 165 (1995).

[68] A. J. Piekny and M. Glotzer, *Anillin is a scaffold protein that links RhoA, actin, and myosin during cytokinesis*, Curr Biol **18**, 30 (2008).

[69] M. J. Renshaw, J. Liu, B. D. Lavoie, and A. Wilde, *Anillin-dependent organization of septin filaments promotes intercellular bridge elongation and Chmp4B targeting to the abscission site*, Open Biol **4**, 130190 (2014).

[70] A. F. Straight, C. M. Field, and T. J. Mitchison, *Anillin binds nonmuscle myosin II and regulates the contractile ring*, Mol. Biol. Cell **16**, 193 (2005).

[71] E. Joo, M. C. Surka, and W. S. Trimble, *Mammalian SEPT2 Is Required for Scaffolding Nonmuscle Myosin II and Its Kinases*, Developmental Cell **13**, 677 (2007).

[72] E. A. Peterson and E. M. Petty, *Conquering the complex world of human septins: implications for health and disease*, Clin. Genet. **77**, 511 (2010).

[73] D. Angelis and E. T. Spiliotis, *Septin Mutations in Human Cancers*, Front Cell Dev Biol **4**, 122 (2016).

[74] C. Poüs, L. Klipfel, A. Baillet, C. Pous, L. Klipfel, A. Baillet, C. Poüs, L. Klipfel, and A. Baillet, *Cancer-Related Functions and Subcellular Localizations of Septins*, Front Cell Dev Biol **4**, 126 (2016).

[75] C. Addi, J. Bai, and A. Echard, *Actin, microtubule, septin and ESCRT filament remodeling during late steps of cytokinesis*, Current Opinion in Cell Biology **50**, 27 (2018).

[76] M. Farkasovsky, P. Herter, B. Voß, and A. Wittinghofer, *Nucleotide binding and filament assembly of recombinant yeast septin complexes*, Biological Chemistry **386**, 643 (2005).

[77] A. Khan, J. Newby, and A. S. Gladfelter, *Control of septin filament flexibility and bundling by subunit composition and nucleotide interactions*, Molecular Biology of the Cell **29**, 702 (2018).

[78] J. A. Frazier, M. L. Wong, M. S. Longtine, J. R. Pringle, M. Mann, T. J. Mitchison, and C. Field, *Polymerization of purified yeast septins: Evidence that organized filament arrays may not be required for septin function*, Journal of Cell Biology **143**, 737 (1998).

[79] G. Garcia, A. Bertin, Z. Li, Y. Song, M. A. McMurray, J. Thorner, and E. Nogales, *Subunit-dependent modulation of septin assembly: budding yeast septin Shs1 promotes ring and gauze formation.*, The Journal of cell biology **195**, 993 (2011).

[80] B. Byers and L. Goetsch, *A highly ordered ring of membrane-associated filaments in budding yeast.*, The Journal of cell biology **69**, 717 (1976).

[81] A. A. Rodal, L. Kozubowski, B. L. Goode, D. G. Drubin, and J. H. Hartwig, *Actin and Septin Ultrastructures at the Budding Yeast Cell Cortex*, Molecular Biology of the Cell **16**, 372 (2005).

[82] A. Bertin and E. Nogales, *Septin filament organization in Saccharomyces cerevisiae*, Communicative and Integrative Biology **5**, 503 (2012).

[83] K. Ong, C. Wloka, S. Okada, T. Svitkina, and E. Bi, *Architecture and dynamic remodelling of the septin cytoskeleton during the cell cycle*, Nature Communications **5**, 5698 (2014).

[84] C. Kaplan, B. Jing, C. M. Winterflood, A. A. Bridges, P. Occhipinti, J. Schmied, S. Grinhagens, T. Gronemeyer, P. Tinnefeld, A. S. Gladfelter, J. Ries, and H. Ewers, *Absolute Arrangement of Subunits in Cytoskeletal Septin Filaments in Cells Measured by Fluorescence Microscopy*, Nano Lett **15**, 3859 (2015).

[85] M. Versele, B. Gullbrand, M. J. Shulewitz, V. J. Cid, S. Bahmanyar, R. E. Chen, P. Barth, T. Alber, and J. Thorner, *Protein-protein interactions governing septin heteropentamer assembly and septin filament organization in Saccharomyces cerevisiae*, Mol Biol Cell **15**, 4568 (2004).

[86] I. D. Marques, N. F. Valadares, W. Garcia, J. C. P. Damalio, J. N. A. Macedo, A. P. U. DeAraujo, C. A. Botello, J. M. Andreu, and R. C. Garratt, *Septin C-Terminal Domain Interactions: Implications for Filament Stability and Assembly* , Cell Biochem. Biophys. **62**, 317 (2012).

[87] E. A. Booth, E. W. Vane, D. Dovala, and J. Thorner, *A förster resonance energy transfer (FRET)-based system provides insight into the ordered assembly of yeast septin hetero-octamers*, Journal of Biological Chemistry **290**, 28388 (2015).

[88] Y. Sadian, C. Gatsogiannis, C. Patasi, O. Hofnagel, R. S. Goody, M. Farkasovsky, and S. Raunser, *The role of Cdc42 and Gic1 in the regulation of septin filament formation and dissociation*, Elife **2**, e01085 (2013).

[89] Y. Xie, J. P. Vessey, A. Konecna, R. Dahm, P. Macchi, and M. A. Kiebler, *The GTP-binding protein Septin 7 is critical for dendrite branching and dendritic-spine morphology*, Curr Biol **17**, 1746 (2007).

[90] Q. Hu, L. Milenkovic, H. Jin, M. P. Scott, M. V. Nachury, E. T. Spiliotis, and W. J. Nelson, *A septin diffusion barrier at the base of the primary cilium maintains ciliary membrane protein distribution*, Science **329**, 436 (2010).

[91] M. Kinoshita, S. Kumar, A. Mizoguchi, C. Ide, A. Kinoshita, T. Haraguchi, Y. Hiraoka, and M. Noda, *Nedd5, a mammalian septin, is a novel cytoskeletal component interacting with actin-based structures.*, Genes & development **11**, 1535 (1997).

[92] A. Hagiwara, Y. Tanaka, R. Hikawa, N. Morone, A. Kusumi, H. Kimura, and M. Kinoshita, *Submembranous septins as relatively stable components of actin-based membrane skeleton*, Cytoskeleton **68**, 512 (2011).

[93] J. Kim and J. A. Cooper, *Septins regulate junctional integrity of endothelial monolayers*, Molecular Biology of the Cell **29**, 1693 (2018).

[94] M. Kinoshita, C. M. Field, M. L. Coughlin, A. F. Straight, and T. J. Mitchison, *Self- and actin-templated assembly of mammalian septins*, Developmental Cell **3**, 791 (2002).

[95] F. Calvo, R. Ranftl, S. Hooper, A. J. J. Farrugia, E. Moeendarbary, A. Bruckbauer, F. Batista, G. Charras, and E. Sahai, *Cdc42EP3/BORG2 and Septin Network Enables Mechano-transduction and the Emergence of Cancer-Associated Fibroblasts*, Cell Rep **13**, 2699 (2015).

[96] K. Schmidt and B. J. Nichols, *Functional interdependence between septin and actin cytoskeleton*, BMC Cell Biol. **5**, 43 (2004).

[97] A. Vissa, M. Giuliani, C. D. Froese, M. S. Kim, F. Soroor, P. K. Kim, W. S. Trimble, and C. M. Yip, *Single-molecule localization microscopy of septin bundles in mammalian cells*, Cytoskeleton (Hoboken) (2018).

[98] M. E. Sellin, P. Holmfeldt, S. Stenmark, and M. Gullberg, *Microtubules support a disk-like septin arrangement at the plasma membrane of mammalian cells*, Molecular Biology of the Cell **22**, 4588 (2011).

[99] E. T. Spiliotis, S. J. Hunt, Q. Hu, M. Kinoshita, and W. J. Nelson, *Epithelial polarity requires septin coupling of vesicle transport to polyglutamylated microtubules.*, The Journal of cell biology **180**, 295 (2008).

[100] B. S. DeMay, X. B. Bai, L. Howard, P. Occhipinti, R. A. Meseroll, E. T. Spiliotis, R. Oldenbourg, and A. S. Gladfelter, *Septin filaments exhibit a dynamic, paired organization that is conserved from yeast to mammals*, Journal of Cell Biology **193**, 1065 (2011).

[101] J. R. Bowen, D. Hwang, X. Bai, D. Roy, and E. T. Spiliotis, *Septin GTPases spatially guide microtubule organization and plus end dynamics in polarizing epithelia*, J. Cell Biol. **194**, 187 (2011).

[102] P. Verdier-Pinard, D. Salaun, H. Bouguenina, S. Shimada, M. Pophillat, S. Audebert, E. Agavnian, S. Coslet, E. Charafe-Jauffret, T. Tachibana, and A. Badache, *Septin 9_i2 is downregulated in tumors, impairs cancer cell migration and alters subnuclear actin filaments*, Sci Rep **7**, 44976 (2017).

[103] M. C. Surka, C. W. Tsang, and W. S. Trimble, *The mammalian septin MSF localizes with microtubules and is required for completion of cytokinesis*, Mol Biol Cell **13**, 3532 (2002).

[104] K. Nagata, A. Kawajiri, S. Matsui, M. Takagishi, T. Shiromizu, N. Saitoh, I. Izawa, T. Kiyono, T. J. Itoh, H. Hotani, and M. Inagaki, *Filament formation of MSF-A, a mammalian septin, in human mammary epithelial cells depends on interactions with microtubules*, J Biol Chem **278**, 18538 (2003).

[105] J. Hu, X. Bai, J. R. Bowen, L. Dolat, F. Korobova, W. Yu, P. W. Baas, T. Svitkina, G. Gallo, and E. T. Spiliotis, *Septin-driven coordination of actin and microtubule remodeling regulates the collateral branching of axons*, Curr Biol **22**, 1109 (2012).

[106] K. Nakos, M. Rosenberg, and E. T. Spiliotis, *Regulation of microtubule plus end dynamics by septin 9*, Cytoskeleton (Hoboken) (2018).

[107] T. Nolke, C. Schwan, F. Lehmann, K. Ostevold, O. Pertz, K. Aktories, T. Nölke, C. Schwan, F. Lehmann, K. Østevold, O. Pertz, and K. Aktories, *Septins guide microtubule protrusions induced by actin-depolymerizing toxins like Clostridium difficile transferase (CDT)*, Proc Natl Acad Sci U S A **113**, 7870 (2016).

[108] F. Pan, R. L. Malmberg, and M. Momany, *Analysis of septins across kingdoms reveals orthology and new motifs.*, BMC evolutionary biology **7**, 103 (2007).

[109] M. Nakahira, J. N. A. Macedo, T. V. Seraphim, N. Cavalcante, T. A. C. B. Souza, J. C. P. Damalio, L. F. Reyes, E. M. Assmann, M. R. Alborghetti, R. C. Garratt, A. P. U. Araujo, N. I. T. Zanchin, J. A. R. G. Barbosa, and J. Kobarg, *A draft of the human septin interactome*, PLoS One **5**, e13799 (2010).

[110] M. Mendoza, A. A. Hyman, and M. Glotzer, *GTP binding induces filament assembly of a recombinant septin*, Curr. Biol. **12**, 1858 (2002).

[111] R. P. H. Huijbregts, A. Svitin, M. W. Stinnett, M. B. Renfrow, and I. Chesnokov, *Drosophila Orc6 facilitates GTPase activity and filament formation of the septin complex*, Mol Biol Cell **20**, 270 (2009).

[112] K. Akhmetova, M. Balasov, R. P. Huijbregts, and I. Chesnokov, *Functional insight into the role of Orc6 in septin complex filament formation in Drosophila*, Mol Biol Cell **26**, 15 (2015).

[113] K. A. Akhmetova, I. N. Chesnokov, and S. A. Fedorova, *Functional Characterization of Septin Complexes*, Molecular Biology **52**, 137 (2018).

[114] T. P. Neufeld and G. M. Rubin, *The Drosophila peanut gene is required for cytokinesis and encodes a protein similar to yeast putative bud neck filament proteins*, Cell **77**, 371 (1994).

[115] H. Fares, M. Peifer, and J. R. Pringle, *Localization and possible functions of Drosophila septins*, Mol. Biol. Cell **6**, 1843 (1995).

[116] J. C. Adam, J. R. Pringle, and M. Peifer, *Evidence for functional differentiation among Drosophila septins in cytokinesis and cellularization*, Mol. Biol. Cell **11**, 3123 (2000).

[117] S. Müller and A. Engel, *Structure and mass analysis by scanning transmission electron microscopy*, Micron **32**, 21 (2001).

[118] A. A. Sousa and R. D. Leapman, *Development and application of STEM for the biological sciences*, Ultramicroscopy **123**, 38 (2012).

[119] A. Bremer, C. Henn, K. Goldie, A. Engel, P. Smith, and U. Aebi, *Towards Atomic Interpretation of F-Actin Filament Three-dimensional Reconstructions*, Journal of Molecular Biology **242**, 683 (1994).

[120] A. Engel, R. Eichner, and U. Aebi, *Polymorphism of reconstituted human epidermal keratin filaments: Determination of their mass-per-length and width by scanning transmission electron microscopy (STEM)*, Journal of Ultrastructure Research **90**, 323 (1985).

[121] U. Wickert, N. Mücke, T. Wedig, S. A. Müller, U. Aebi, and H. Herrmann, *Characterization of the in vitro co-assembly process of the intermediate filament proteins vimentin and desmin: mixed polymers at all stages of assembly*, European Journal of Cell Biology **84**, 379 (2005).

[122] D. Holmes, H. Graham, J. Trotter, and K. Kadler, *STEM/TEM studies of collagen fibril assembly*, Micron **32**, 273 (2001).

[123] A. Crewe and J. Wall, *A scanning microscope with 5 Å resolution*, Journal of Molecular Biology **48**, 375 (1970).

[124] A. A. Sousa and R. D. Leapman, *Quantitative STEM mass measurement of biological macromolecules in a 300 kV TEM*, Journal of microscopy **228**, 25 (2007).

[125] C. L. Woodcock, L. L. Frado, and J. S. Wall, *Composition of native and reconstituted chromatin particles: direct mass determination by scanning transmission electron microscopy.*, Proceedings of the National Academy of Sciences of the United States of America **77**, 4818 (1980).

[126] J. S. Wall and J. Hainfeld, *Mass Mapping With The Scanning-Transmission Electron-Microscope*, Annual Review Of Biophysics And Biophysical Chemistry **15**, 355 (1986).

[127] M. Mavrakis, F. C. Tsai, and G. H. Koenderink, *Purification of recombinant human and Drosophila septin hexamers for TIRF assays of actin-septin filament assembly*, Methods in Cell Biology **136**, 199 (2016).

[128] B. Birdsall, R. W. King, M. R. Wheeler, C. A. Lewis, S. R. Goode, R. Dunlap, and G. C. Roberts, *Correction for light absorption in fluorescence studies of protein-ligand interactions*, Analytical Biochemistry **132**, 353 (1983).

[129] E. Gasteiger, A. Gattiker, C. Hoogland, I. Ivanyi, R. D. Appel, and A. Bairoch, *ExPASy: The proteomics server for in-depth protein knowledge and analysis.*, Nucleic acids research **31**, 3784 (2003).

[130] C. Gell, V. Bormuth, G. J. Brouhard, D. N. Cohen, S. Diez, C. T. Friel, J. Helenius, B. Nitzsche, H. Petzold, J. Ribbe, E. Schäffer, J. H. Stear, A. Trushko, V. Varga, P. O. Widlund, M. Zanic, and J. Howard, *Microtubule Dynamics Reconstituted In Vitro and Imaged by Single-Molecule Fluorescence Microscopy*, Methods in Cell Biology **95**, 221 (2010).

[131] I. Rasnik, S. A. McKinney, and T. Ha, *Nonblinking and long-lasting single-molecule fluorescence imaging*, Nature Methods **3**, 891 (2006).

[132] C. E. Aitken, R. A. Marshall, and J. D. Puglisi, *An oxygen scavenging system for improvement of dye stability in single-molecule fluorescence experiments*, Biophysical Journal **94**, 1826 (2008).

[133] P. V. Patil and D. P. Ballou, *The use of protocatechuate dioxygenase for maintaining anaerobic conditions in biochemical experiments*, Analytical Biochemistry **286**, 187 (2000).

[134] J. Schindelin, I. Arganda-Carreras, E. Frise, V. Kaynig, M. Longair, T. Pietzsch, S. Preibisch, C. Rueden, S. Saalfeld, B. Schmid, J. Y. Tinevez, D. J. White, V. Hartenstein, K. Eliceiri, P. Tomancak, and A. Cardona, *Fiji: An open-source platform for biological-image analysis*, Nature Methods **9**, 676 (2012).

[135] R. Freeman and K. R. Leonard, *Comparative mass measurement of biological macromolecules by scanning transmission electron microscopy*, Journal of Microscopy **122**, 275 (1981).

[136] A. A. Sousa and R. D. Leapman, *Mass Mapping of Amyloid Fibrils in the Electron Microscope Using STEM Imaging*, in *Nanoimaging*, pages 195–207, Humana Press, Totowa, NJ, 2013.

[137] D. Nečas and P. Klapetek, *Gwyddion: an open-source software for SPM data analysis*, Open Physics **10**, 181 (2012).

[138] M. de Wild, W. Pomp, and G. H. Koenderink, *Thermal memory in self-assembled collagen fibril networks*, Biophysical journal **105**, 200 (2013).

[139] H. Herrmann, M. Häner, M. Brettel, S. A. Müller, K. N. Goldie, B. Fedtke, A. Lustig, W. W. Franke, and U. Aebi, *Structure and assembly properties of the intermediate filament protein vimentin: The role of its head, rod and tail domains*, Journal of Molecular Biology **264**, 933 (1996).

[140] C. Renz, N. Johnsson, and T. Gronemeyer, *An efficient protocol for the purification and labeling of entire yeast septin rods from E.coli for quantitative in vitro experimentation*, BMC Biotechnol **13**, 60 (2013).

[141] F. A. Sala, N. F. Valadares, J. N. Macedo, J. C. Borges, and R. C. Garratt, *Heterotypic Coiled-Coil Formation is Essential for the Correct Assembly of the Septin Heterofilament*, Biophys J **111**, 2608 (2016).

[142] W. Garcia, A. P. Ulian De Araújo, M. De Oliveira Neto, M. R. Ballestero, I. Polikarpov, M. Tanaka, T. Tanaka, and R. C. Garratt, *Dissection of a human septin: Definition and characterization of distinct domains within human SEPT4*, Biochemistry **45**, 13918 (2006).

[143] S. C. Hsu, C. D. Hazuka, R. Roth, D. L. Foletti, J. Heuser, and R. H. Scheller, *Subunit composition, protein interactions, and structures of the mammalian brain sec6/8 complex and septin filaments*, Neuron **20**, 1111 (1998).

[144] K. S. Cannon, B. L. Woods, J. M. Crutchley, and A. S. Gladfelter, *An amphipathic helix enables septins to sense micrometer-scale membrane curvature*, (2019).

[145] R. S. O'Neill and D. V. Clark, *Partial Functional Diversification of Drosophila melanogaster Septin Genes Sep2 and Sep5*, G3 (Bethesda) **6**, 1947 (2016).

[146] R. Nishihama, M. Onishi, and J. R. Pringle, *New insights into the phylogenetic distribution and evolutionary origins of the septins*, Biol Chem **392**, 681 (2011).

[147] B. Kartmann and D. Roth, *Novel roles for mammalian septins: from vesicle trafficking to oncogenesis*, Journal of Cell Science **114** (2001).

[148] Y. W. Huang, M. Yan, R. F. Collins, J. E. DiCiccio, S. Grinstein, and W. S. Trimble, *Mammalian Septins Are Required for Phagosome Formation*, Molecular Biology of the Cell **19**, 1717 (2008).

[149] J. Marquardt, X. Chen, and E. Bi, *Architecture, remodeling, and functions of the septin cytoskeleton*, Cytoskeleton (Hoboken) (2018).

[150] A. Bertin, M. A. McMurray, J. Piersonb, L. Thai, K. L. McDonald, E. A. Zehr, G. Garcia, P. Peters, J. Thorner, and E. Nogales, *Three-dimensional ultrastructure of the septin filament network in Saccharomyces cerevisiae* , Mol. Biol. Cell **23**, 423 (2012).

[151] G. C. Finnigan, E. A. Booth, A. Duvalyan, E. N. Liao, and J. Thorner, *The Carboxy-Terminal Tails of Septins Cdc11 and Shs1 Recruit Myosin-II Binding Factor Bni5 to the Bud Neck in Saccharomyces cerevisiae*, Genetics **200**, 843 (2015).

[152] G. C. Finnigan, A. Duvalyan, E. N. Liao, A. Sargsyan, and J. Thorner, *Detection of protein-protein interactions at the septin collar in Saccharomyces cerevisiae using a tripartite split-GFP system*, Mol Biol Cell **27**, 2708 (2016).

[153] M. S. Longtine, C. L. Theesfeld, J. N. McMillan, E. Weaver, J. R. Pringle, and D. J. Lew, *Septin-dependent assembly of a cell cycle-regulatory module in Saccharomyces cerevisiae.*, Molecular and cellular biology **20**, 4049 (2000).

[154] D. Tamborrini, M. A. Juanes, S. Ibanes, G. Rancati, and S. Piatti, *Recruitment of the mitotic exit network to yeast centrosomes couples septin displacement to actomyosin constriction*, Nat Commun **9**, 4308 (2018).

[155] Y. Barral, V. Mermall, M. S. Mooseker, and M. Snyder, *Compartmentalization of the cell cortex by septins is required for maintenance of cell polarity in yeast*, Molecular Cell **5**, 841 (2000).

[156] P. A. Takizawa, *Plasma Membrane Compartmentalization in Yeast by Messenger RNA Transport and a Septin Diffusion Barrier*, Science **290**, 341 (2000).

[157] L. Clay, F. Caudron, A. Denoth-Lippuner, B. Boettcher, S. Buvelot Frei, E. Lee Snapp, and Y. Barral, *A sphingolipid-dependent diffusion barrier confines ER stress to the yeast mother cell*, **3**, 1883 (2014).

[158] G. Garcia III, G. C. Finnigan, L. R. Heasley, S. M. Sterling, A. Aggarwal, C. G. Pearson, E. Nogales, M. A. McMurray, and J. Thorner, *Assembly, molecular organization, and membrane-binding properties of development-specific septins*, J Cell Biol **212**, 515 (2016).

[159] A. Beber, M. Alqabandi, C. Prevost, F. Viars, D. Levy, P. Bassereau, A. Bertin, S. Mangenot, C. Prévost, F. Viars, D. Lévy, P. Bassereau, A. Bertin, and S. Mangenot, *Septin-based readout of PI(4,5)P2 incorporation into membranes of giant unilamellar vesicles*, Cytoskeleton (2018).

[160] S. J. Cho, H. Lee, S. Dutta, J. Song, R. Walikonis, and I. S. Moon, *Septin 6 regulates the cytoarchitecture of neurons through localization at dendritic branch points and bases of protrusions*, Molecules and Cells **32**, 89 (2011).

[161] O. Palander, M. El-Zeiry, and W. S. Trimble, *Uncovering the Roles of Septins in Cilia*, Front Cell Dev Biol **5**, 36 (2017).

[162] H. Ewers, T. Tada, J. D. Petersen, B. Racz, M. Sheng, and D. Choquet, *A Septin-Dependent Diffusion Barrier at Dendritic Spine Necks*, PLoS One **9**, e113916 (2014).

[163] K. Schmidt and B. J. Nichols, *A barrier to lateral diffusion in the cleavage furrow of dividing mammalian cells*, Curr. Biol. **14**, 1002 (2004).

[164] E. T. Spiliotis, M. Kinoshita, and W. J. Nelson, *A mitotic septin scaffold required for mammalian chromosome congression and segregation* , Science **307**, 1781 (2005).

[165] G. Garcia III, A. Bertin, Z. Li, Y. Song, M. A. McMurray, J. Thorner, and E. Nogales, *Subunit-dependent modulation of septin assembly: Budding yeast septin Shs1 promotes ring and gauze formation* , J. Cell Biol. **195**, 993 (2011).

[166] P. A. Leventis and S. Grinstein, *The Distribution and Function of Phosphatidylserine in Cellular Membranes*, Annual Review of Biophysics **39**, 407 (2010).

[167] J. Braunger, C. Kramer, D. Morick, and C. Steinem, *Solid supported membranes doped with PIP2: influence of ionic strength and pH on bilayer formation and membrane organization.*, Langmuir : the ACS journal of surfaces and colloids **29**, 14204 (2013).

[168] R. P. Richter and A. R. Brisson, *Following the formation of supported lipid bilayers on mica: a study combining AFM, QCM-D, and ellipsometry*, Biophys J **88**, 3422 (2005).

[169] G. Blin, E. Margeat, K. Carvalho, C. A. Royer, C. Roy, and C. Picart, *Quantitative analysis of the binding of ezrin to large unilamellar vesicles containing phosphatidylinositol 4,5 bisphosphate*, Biophysical Journal **94**, 1021 (2008).

[170] E. E. Kooijman, K. E. King, M. Gangoda, and A. Gericke, *Ionization properties of phosphatidylinositol polyphosphates in mixed model membranes.*, Biochemistry **48**, 9360 (2009).

[171] M. Toner, G. Vaio, A. McLaughlin, and S. McLaughlin, *Adsorption of Cations to Phosphatidylinositol 4,5-Bisphosphate*, Biochemistry **27**, 7435 (1988).

[172] Z. T. Graber, Z. Jiang, A. Gericke, and E. E. Kooijman, *Phosphatidylinositol-4,5-bisphosphate ionization and domain formation in the presence of lipids with hydrogen bond donor capabilities*, Chemistry and Physics of Lipids **165**, 696 (2012).

[173] T. Yeung, G. E. Gilbert, J. Shi, J. Silvius, A. Kapus, and S. Grinstein, *Membrane phosphatidylserine regulates surface charge and protein localization.*, Science (New York, N.Y.) **319**, 210 (2008).

[174] S. McLaughlin and D. Murray, *Plasma membrane phosphoinositide organization by protein electrostatics.*, Nature **438**, 605 (2005).

[175] A. A. Bertin, *Personal Communication*.

[176] R. Richter, A. Mukhopadhyay, and A. Brisson, *Pathways of lipid vesicle deposition on solid surfaces: A combined QCM-D and AFM study*, Biophysical Journal **85**, 3035 (2003).

[177] R. Zhang, N. Kumar, J. L. Ross, M. L. Gardel, and J. J. de Pablo, *Interplay of structure, elasticity, and dynamics in actin-based nematic materials.*, Proceedings of the National Academy of Sciences of the United States of America **115**, E124 (2018).

[178] M. Onishi, T. Koga, A. Hirata, T. Nakamura, H. Asakawa, C. Shimoda, J. Bähler, J. Q. Wu, K. Takegawa, H. Tachikawa, J. R. Pringle, and Y. Fukui, *Role of septins in the orientation of forespore membrane extension during sporulation in fission yeast.*, Molecular and cellular biology **30**, 2057 (2010).

[179] K. I. Lee, W. Im, and R. W. Pastor, *Langevin dynamics simulations of charged model phosphatidylinositol lipids in the presence of diffusion barriers: toward an atomic level understanding of corralling of PIP2 by protein fences in biological membranes*, BMC Biophys **7**, 13 (2014).

[180] ExPASy, *COILS : https://embnet.vital-it.ch/software/COILS_form.html*.

[181] M. Bovellan, Y. Romeo, M. Biro, A. Boden, P. Chugh, A. Yonis, M. Vaghela, M. Fritzsche, D. Moulding, R. Thorogate, A. Jégou, A. Thrasher, G. Romet-Lemonne, P. Roux, E. Paluch, and G. Charras, *Cellular Control of Cortical Actin Nucleation*, Current Biology **24**, 1628 (2014).

[182] M. Fritzsche, C. Erlenkämper, E. Moeendarbary, G. Charras, and K. Kruse, *Actin kinetics shapes cortical network structure and mechanics*, Science Advances **2**, e1501337 (2016).

[183] E. Fischer-Friedrich, Y. Toyoda, C. J. Cattin, D. J. Müller, A. A. Hyman, and F. Jülicher, *Rheology of the Active Cell Cortex in Mitosis*, Biophysical Journal **111**, 589 (2016).

[184] R. Clément, B. Dehapiot, C. Collinet, T. Lecuit, and P. F. Lenne, *Viscoelastic Dissipation Stabilizes Cell Shape Changes during Tissue Morphogenesis*, Current Biology **27**, 3132 (2017).

[185] P. Kanchanawong, G. Shtengel, A. M. Pasapera, E. B. Ramko, M. W. Davidson, H. F. Hess, and C. M. Waterman, *Nanoscale architecture of integrin-based cell adhesions.*, Nature **468**, 580 (2010).

[186] M. B. Smith, H. Li, T. Shen, X. Huang, E. Yusuf, and D. Vavylonis, *Segmentation and tracking of cytoskeletal filaments using open active contours*, Cytoskeleton **67**, 693 (2010).

[187] A. S. Gladfelter, *Guides to the final frontier of the cytoskeleton: septins in filamentous fungi*, Curr Opin Microbiol **13**, 720 (2010).

[188] C. Lin, Y. Shen, H. Wang, C. Chiang, C. Wang, and P. Kuo, *Regulation of septin phosphorylation: SEPT12 phosphorylation in sperm septin assembly*, Cytoskeleton **76**, 137 (2019).

[189] M. Biro, Y. Romeo, S. Kroschwald, M. Bovellan, A. Boden, J. Tcherkezian, P. P. Roux, G. Charras, and E. K. Paluch, *Cell cortex composition and homeostasis resolved by integrating proteomics and quantitative imaging.*, Cytoskeleton (Hoboken, N.J.) **754**, 741 (2013).

[190] A. Liu and D. A. Fletcher, *Biology under construction: in vitro reconstitution of cellular function*, Nat. Rev. Mol. Cell Biol. **10**, 644 (2009).

[191] G. Rivas, S. K. Vogel, and P. Schwille, *Reconstitution of cytoskeletal protein assemblies for large-scale membrane transformation*, Current Opinion in Chemical Biology **22**, 18 (2014).

[192] I. Reviakine, D. Johannsmann, and R. P. Richter, *Hearing What You Cannot See and Visualizing What You Hear*, Analytical chemistry **83**, 8838 (2011).

[193] N. J. Cho, C. W. Frank, B. Kasemo, and F. Höök, *Quartz crystal microbalance with dissipation monitoring of supported lipid bilayers on various substrates.*, Nat. Protoc. **5**, 1096 (2010).

[194] G. Sauerbrey, *Use of Quartz Crystal Vibrator for Weighting Thin Films on a Microbalance*, Zeitschrift fur Physik **155**, 206 (1959).

[195] N. B. Eisele, F. I. Andersson, S. Frey, and R. P. Richter, *Viscoelasticity of thin biomolecular films: A case study on nucleoporin phenylalanine-glycine repeats grafted to a histidine-tag capturing QCM-D sensor*, Biomacromolecules **13**, 2322 (2012).

[196] D. Johannsmann, I. Reviakine, and R. P. Richter, *Dissipation in films of adsorbed nanospheres studied by quartz crystal microbalance (QCM)*, Anal Chem **81**, 8167 (2009).

[197] J. A. De Feijter, J. Benjamins, and F. A. Veer, *Ellipsometry as a tool to study the adsorption behavior of synthetic and biopolymers at the air-water interface*, Biopolymers **17**, 1759 (1978).

[198] P. Bingen, G. Wang, N. F. Steinmetz, M. Rodahl, and R. P. Richter, *Solvation effects in the quartz crystal microbalance with dissipation monitoring response to biomolecular adsorption. A phenomenological approach*, Anal Chem **80**, 8880 (2008).

[199] R. Konradi, M. Textor, E. Reimhult, R. Konradi, M. Textor, and E. Reimhult, *Using Complementary Acoustic and Optical Techniques for Quantitative Monitoring of Biomolecular Adsorption at Interfaces*, Biosensors **2**, 341 (2012).

[200] I. Carton, A. R. Brisson, and R. P. Richter, *Label-free detection of clustering of membrane-bound proteins*, Analytical Chemistry **82**, 9275 (2010).

[201] P. Drucker, D. Grill, V. Gerke, and H. J. Galla, *Formation and characterization of supported lipid bilayers containing phosphatidylinositol-4,5-bisphosphate and cholesterol as functional surfaces*, Langmuir **30**, 14877 (2014).

[202] R. P. Richter, J. L. K. Him, B. Tessier, C. Tessier, and A. R. Brisson, *On the kinetics of adsorption and two-dimensional self-assembly of annexin A5 on supported lipid bilayers.*, Biophysical journal **89**, 3372 (2005).

[203] P. Drücker, M. Pejic, D. Grill, H. J. Galla, and V. Gerke, *Cooperative binding of annexin A2 to cholesterol- and phosphatidylinositol-4,5-bisphosphate-containing bilayers*, Biophys J **107**, 2070 (2014).

[204] V. Shabardina, C. Kramer, B. Gerdes, J. Braunger, A. Cordes, J. Schäfer, I. Mey, D. Grill, V. Gerke, and C. Steinem, *Mode of Ezrin-Membrane Interaction as a Function of PIP2 Binding and Pseudophosphorylation*, Biophysical Journal **110**, 2710 (2016).

[205] R. J. Barfoot, K. H. Sheikh, B. R. Johnson, J. M. Colyer RE, L. J. Jeuken, R. J. Bushby, and S. R. Evans, *Minimal F-actin cytoskeletal system for planar supported phospholipid bilayers*, Langmuir **24**, 6827 (2008).

[206] H. Van Zalinge, J. Aveyard, J. Hajne, M. Persson, A. Mansson, and D. V. Nicolau, *Actin filament motility induced variation of resonance frequency and rigidity of polymer surfaces studied by quartz crystal microbalance*, Langmuir **28**, 15033 (2012).

[207] I. F. Márquez, P. Mateos-Gil, J. Y. Shin, R. Lagos, O. Monasterio, and M. Vélez, *Mutations on FtsZ lateral helix H3 that disrupt cell viability hamper reorganization of polymers on lipid surfaces*, Biochimica et Biophysica Acta (BBA) - Biomembranes **1859**, 1815 (2017).

[208] M. K. Baumann, E. Amstad, A. Mashaghi, M. Textor, and E. Reimhult, *Characterization of supported lipid bilayers incorporating the phosphoinositides phosphatidylinositol 4,5-biphosphate and phosphoinositol-3,4,5-triphosphate by complementary techniques.*, Biointerphases **5**, 114 (2010).

[209] R. P. Richter, R. Berat, A. R. Brisson, R. Bérat, and A. R. Brisson, *Formation of solid-supported lipid bilayers: An integrated view*, Langmuir **22**, 3497 (2006).

[210] M. D. Ward and D. A. Buttry, *In situ interfacial mass detection with piezoelectric transducers*, Science (New York, N.Y.) **249**, 1000 (1990).

[211] R. P. Richter, K. B. Rodenhausen, N. B. Eisele, and M. Schubert, *Coupling spectroscopic ellipsometry and quartz crystal microbalance to study organic films at the solid-liquid interface*, in *Ellipsometry of functional organic surfaces and films*, edited by K. Hinrichs and K. J. Eichhorn, pages 223–248, Springer Berlin Heidelberg, Berlin, Heidelberg, 2014.

[212] H. G. Tompkins, E. A. Irene, C. Hill, and N. Carolina, *Handybook of Ellipsometry*, William Andrew, 2005.

[213] B. Johs and J. S. Hale, *Dielectric function representation by B-splines*, Physica Status Solidi (A) Applications and Materials Science **205**, 715 (2008).

[214] S. A. J. van der Meulen, G. V. Dubacheva, M. Dogterom, R. P. Richter, and M. E. Leunissen, *Quartz crystal microbalance with dissipation monitoring and spectroscopic ellipsometry measurements of the phospholipid bilayer anchoring stability and kinetics of hydrophobically modified DNA oligonucleotides*, Langmuir **30**, 6525 (2014).

[215] H. J. Butt and M. Jaschke, *Calculation of thermal noise in atomic force microscopy*, Nanotechnology **6**, 1 (1995).

[216] S. Garcia-Manyes and F. Sanz, *Nanomechanics of lipid bilayers by force spectroscopy with AFM: A perspective*, Biochimica et Biophysica Acta - Biomembranes **1798**, 741 (2010).

[217] C. A. Keller and B. Kasemo, *Surface specific kinetics of lipid vesicle adsorption measured with a quartz crystal microbalance*, Biophysical Journal **75**, 1397 (1998).

[218] W. T. Hermens, M. Benes, R. Richter, and H. Speijer, *Effects of flow on solute exchange between fluids and supported biosurfaces*, Biotechnol Appl Biochem **39**, 277 (2004).

[219] M. Edvardsson, S. Svedhem, G. Wang, R. Richter, M. Rodahl, and B. Kasemo, *QCM-D and reflectometry instrument: Applications to supported lipid structures and their biomolecular interactions*, Analytical Chemistry **81**, 349 (2009).

[220] E. Tellechea, D. Johannsmann, N. F. Steinmetz, R. P. Richter, and I. Reviakine, *Model-independent analysis of QCM data on colloidal particle adsorption*, Langmuir **25**, 5177 (2009).

[221] C. Canale, M. Jacono, A. Diaspro, and S. Dante, *Force spectroscopy as a tool to investigate the properties of supported lipid membranes*, Microscopy Research and Technique **73**, 965 (2010).

[222] V. Wollrab, J. M. Belmonte, M. Leptin, F. Nedelec, and G. H. Koenderink, *Polarity sorting drives remodeling of actin-myosin networks*, Journal of Cell Science , 314484 (2018).

[223] J. Alvarado, M. Sheinman, A. Sharma, F. C. MacKintosh, and G. H. Koenderink, *Molecular motors robustly drive active gels to a critically connected state*, Nature Physics **9**, 591 (2013).